

**SYNTHESIS, CHARACTERIZATION, PROPERTIES, AND TRIBOLOGICAL
PERFORMANCE OF 2D NANOMATERIALS**

A Dissertation

by

XINGLIANG HE

Submitted to the Office of Graduate and Professional Studies of
Texas A&M University
in partial fulfillment of the requirements for the degree of

DOCTOR OF PHILOSOPHY

Chair of Committee,	Hong Liang
Committee Members,	Ibrahim Karaman
	Xinghang Zhang
	James D. Batteas
Head of Department,	Andreas A. Polycarpou

May 2014

Major Subject: Mechanical Engineering

Copyright 2014 Xingliang He

ABSTRACT

Demand in wear and friction reduction drives continuous development of new lubricant additives for energy saving in wide engineering applications. In the present research, a new approach has been developed in order to modify the viscosity of lubricants using novel nanostructured particles.

Experimental approaches include synthesis, characterization, and tribological and rheological investigation of nanoparticles, yttrium oxide (Y_2O_3), α -zirconium phosphate (ZrP), and boron (B)-boron trioxide (B_2O_3) composite. It was discovered that the sheet-shaped nanoparticles in particular are effective in friction and viscosity reduction.

Specifically, friction coefficient was reduced by $\sim 40\%$ and $\sim 65\%$, respectively, when Y_2O_3 nanosheets and α -ZrP nanoplatelets were added in mineral oil.

Physical and rheological analyses based on basic principles of fluid dynamics were conducted. It was found out that the improved lubricating performance caused by the viscosity reduction. The relationship between structure-fluid properties was established. It showed that the inclination of 2D nanoparticles in fluid direction reduced the viscosity.

In the present research, fluidic additives for lubricants have been demonstrated for the first time. Using 2D nanoparticles provides fundamentally new solution to reduce friction-induced energy loss in liquid lubrication. New understandings on nano-fluidics and nano-rheology will be beneficial to a broad range of tribology-related applications,

e.g., industrial machinery, microelectronic processing, oil production and transportation, organic manufacturing, bioengineering, food processing, and pharmaceuticals.

DEDICATION

To my beloved family, with whom my life is the most beautiful one!

ACKNOWLEDGEMENTS

Undertaking this Ph.D. research has been a truly life-changing experience for me. I would not have been able to see it through without the support and guidance that I received from many individuals. First and foremost, I would like to sincerely and gratefully thank my advisor, Dr. Hong Liang, for her guidance, support, patience, and the most importantly, her friendship during my graduate studies at Texas A&M University. She inspired my creativity, helped me to think independently, and always encouraged me to do my best.

I would also like to recognize the support from the rest of my committee members, Dr. Ibrahim Karaman, Dr. Xinghang Zhang, and Dr. James D. Batteas for their valuable advice and comments throughout the course of this research.

I would also like to acknowledge the financial support from Texas A&M University, Texas Engineering Experiment Station, GE Power & Water, Baker Hughes, Varel International, and Kennametal, Inc. Special gratitude also goes to the Microscopy Image Center (MIC), the Material Characterization Facility (MCF), and the X-ray Diffraction Laboratory at Texas A&M University for their service in characterization.

I also want to extend my gratitude to all the members in Surface Science Group for their countless assistance, comments, and suggestions in my research. Assistance provided by Dr. Elon J. Terrell, Dr. Xinchun Lu, Dr. Abraham Clearfield, Dr. Partha Mukherjee, Dr. Tony Van Buuren, Dr. Iraidia N. Demchenko, Dr. Wayne C. Stolte, Dr. Karla Balzuweit, Dr. Hung-Jue Sue, Dr. Alexei Sokolov, Dr. Xing Cheng, Dr. Agustín

Díaz, Mr. Mel J. Esmacher, Mr. Jonathan Kyle, Mr. Youxing Chen, Mr. Miao Song, Mr. Youwei Jiang, Mr. Peng Li, Ms. Xiayun Huang, and Mr. Alexander Sinyukov in my graduate research are also deeply appreciated.

Thanks also go to my friends and the department faculty and staff for making my time at Texas A&M University a great experience.

Finally, I am forever indebted to my family. Thank you to my parents, my wife, and my brother for all of their love, supports, and endless patience.

NOMENCLATURE

Acronyms

AFM	Atomic force microscope
CMP	Chemical-mechanical planarization
CVD	Chemical vapor deposition
FESEM	Field emission scanning electron microscope/microscopy
FTIR	Fourier transform infrared spectroscopy
NP	Nanoparticle
NS	Nanosheet
NW	Nanowire
PPD	Pour point depressant
SAED	Selected area electron diffraction
TEM	Transmission electron microscope/microscopy
WIWNU	Within-wafer-non-uniformity
XRD	X-ray diffraction

Symbols

P	Pressure
h	Lubricant film thickness
R _a	Arithmetic average roughness
R _q	Root-mean-square average roughness

u	Velocity
η	Viscosity
σ	Normal stress
τ	Shear stress
ρ	Density

TABLE OF CONTENTS

	Page
ABSTRACT	ii
DEDICATION	iv
ACKNOWLEDGEMENTS	v
NOMENCLATURE.....	vii
TABLE OF CONTENTS	ix
LIST OF FIGURES.....	xii
LIST OF TABLES	xviii
CHAPTER I INTRODUCTION	1
1.1. Lubricant additives.....	1
1.1.1. Deposit-control additives	2
1.1.1.1. Antioxidants	3
1.1.1.2. Zinc dithiophosphate (ZDDP).....	5
1.1.1.3. Dispersant and detergent	7
1.1.2. Film-forming additives.....	9
1.1.3. Anti-wear and extreme-pressure additives	11
1.1.4. Miscellaneous additives	13
1.2. Viscosity modification for lubricants.....	15
1.2.1. Organic viscosity modifiers	16
1.2.2. Einstein relationship between additives and viscosity	17
1.2.3. Non-Einstein-like viscosity reduction	19
1.3. Two-dimensional nanomaterials	20
1.4. Summary	24
CHAPTER II MOTIVATION AND OBJECTIVES	26
CHAPTER III MATERIALS AND METHODS.....	30
3.1. Materials.....	30
3.2. Synthesis of nanomaterials.....	31
3.2.1. Y ₂ O ₃ nanosheets.....	31

3.2.2.	α -ZrP nanoplatelets	33
3.2.3.	B-B ₂ O ₃ composited nanoparticles	33
3.3.	Characterization	35
3.4.	Tribological and rheological experiments	36
3.5.	CMP experiments using different nano-abrasives	38
3.5.1.	B-B ₂ O ₃ nanoparticles as abrasives	39
3.5.2.	Y ₂ O ₃ nanosheets as abrasives	40
CHAPTER IV SYNTHESIS AND CHARACTERIZATION		42
4.1.	Yttrium oxide nanosheets	42
4.1.1.	Synthesis of multiphase Y ₂ O ₃ nanosheets (NS)	42
4.1.2.	Phase transformation	45
4.1.3.	I-V characteristics	49
4.2.	α -zirconium phosphate (ZrP) nanoplatelets	54
4.3.	Boron-B ₂ O ₃ composited nanoparticles	58
4.3.1.	Size-specific synthesis of boron nanoparticles	59
4.3.2.	Preparation of boron-B ₂ O ₃ composited nanoparticles	62
4.4.	Summary	64
CHAPTER V TRIBOLOGICAL EVALUATION OF 2D NANOPARTICLES		66
5.1.	Frictional behavior	66
5.1.1.	2D nanoparticles as additives in lubricants	67
5.1.2.	Roles of concentration in friction	69
5.2.	Effects of experimental parameters on friction	72
5.2.1.	Effects of applied loads	73
5.2.2.	Effects of rotational speeds	76
5.2.3.	Aqueous lubricants	79
5.3.	Intermolecular interactions between fluid molecules and nano-additives	81
5.4.	Tribological performance in Cu CMP	85
5.4.1.	Utilization of nanosheets as slurry abrasives	86
5.4.2.	Utilization of B-B ₂ O ₃ composite nanoparticles as slurry abrasives	93
5.5.	Summary	101
CHAPTER VI VISCOSITY MODIFICATION USING 2D NANO-ADDITIVES		103
6.1.	Effects of 2D nano-additives on lubricating performance	103
6.1.1.	Evaluation via Stribeck curves	103
6.1.2.	Lubricating behavior of 2D nanomaterials	107
6.2.	Non-Einstein-like reduction of viscosity	110
6.2.1.	Viscosity modification using 2D nano-additives	110
6.2.2.	Thixotropic study	112
6.3.	Mechanisms	114

6.3.1. Fluid mechanics calculation	115
6.3.2. Viscous flow analysis.....	119
6.3.2.1. Viscosity expression in pure lubricant	119
6.3.2.2. Viscosity with spherical nanoparticles as additives	120
6.3.2.3. Viscosity with 2D nanosheets as additives	122
6.3.3. Particle hydrodynamic simulation.....	126
6.4. Summary	130
 CHAPTER VII CONCLUSIONS AND FUTURE WORKS	 131
7.1. Conclusions	131
7.2. Future works.....	133
 REFERENCES.....	 135

LIST OF FIGURES

	Page
Figure 1.1. Fuel energy consumption in passenger cars.....	2
Figure 1.2. Classification of lubricant additives.....	2
Figure 1.3. (a) Deposit-formation mechanism. (b) Formation of deposit precursors. (c) Interaction between deposit-forming products.....	4
Figure 1.4. (a) Symmetrical molecular structures of monomeric ZDDP. (b) Molecular structure of ZDDP tetramer.....	6
Figure 1.5. (a) A typical detergent molecular structure. (b) Polarized oxidizing deposit is suspended in lubricant oil.....	8
Figure 1.6. (a) Surface-additive interacting mode; (b) additives adsorption on the metal surface; (c) interaction of a metal surface with the organic film- forming additives.....	10
Figure 1.7. Exfoliation of the inorganic film-forming additive.....	11
Figure 1.8. Commonly used anti-wear additives.....	12
Figure 1.9. Surfactant microstructures assembled in liquid.....	15
Figure 1.10. Viscosity-temperature properties of lubricants using polymers (a) and PPD (b).....	17
Figure 2.1. Research flow chart.....	27
Figure 3.1. Schematic diagram of the Teflon [®] -lined pressure vessel.....	32
Figure 3.2. Scheme of the home-built CVD system and brief route for synthesis of B-B ₂ O ₃ composited nanoparticles.....	34
Figure 3.3. Diagram of the pin-on-disk testing configuration.....	37
Figure 3.4. Schematic setup of AR-G2 rheometer.....	37
Figure 3.5. Illustration of CMP experimental setup schematically.....	38
Figure 3.6. Pictures of the Universal CMP Tester.....	41

Figure 4.1.	TEM images of irregular Y_2O_3 nanostructure (a), Y_2O_3 NS (b) and Y_2O_3 NW (c) synthesized at 80 °C, 120 °C, and 240 °C, respectively. (d) AFM images of the Y_2O_3 NS. (e) Comparison of XRD patterns among the commercial multiphase Y_2O_3 powder (bottom black pattern), the irregular nanostructure, NS, and NW of multiphase Y_2O_3 (top colorized patterns)	44
Figure 4.2.	(a) Comparison of XRD patterns among the commercial multiphase Y_2O_3 powder (bottom black pattern), the multiphase Y_2O_3 NS (middle blue pattern), and the single-phase cubic Y_2O_3 -Cu NS (top red pattern); (b) TEM image of the single-phase cubic Y_2O_3 -Cu NS	47
Figure 4.3.	(a) XRD patterns of multiphase Y_2O_3 NS synthesized in the presences of the other metal ions. (b) TEM images of multiphase Y_2O_3 NS synthesized in the presences of the other metal ions	48
Figure 4.4.	SAED patterns of the single-phase cubic Y_2O_3 -Cu NS (a) and the multiphase Y_2O_3 NS (b).....	48
Figure 4.5.	(a) Schematic of the I-V setup. I-V characteristics of the Cu substrate electrode (b), the commercial multiphase Y_2O_3 powder (c), the multiphase Y_2O_3 NS (d), and the single-phase cubic Y_2O_3 -Cu NS (e). (f) Structure of cubic Y_2O_3	51
Figure 4.6.	Scheme of electronic/ionic transportation under positive (a) and negative (b) bias, respectively.....	52
Figure 4.7.	XRD pattern (a), and FESEM (b) and TEM (c) images of α -ZrP nanoplatelets	55
Figure 4.8.	AFM images showing stacked layer of α -ZrP nanoplatelets with low (a) and (b) high magnification. (c) AFM images of a single α -ZrP nanoplatelet with 3D visualization.....	56
Figure 4.9.	(a) Schematic representation of the atomically-layered structure of α -ZrP. (b) Dry friction results with α -ZrP nanoplatelets (top red curve), graphite (bottom green curve), and without any additives (middle black curve)	57
Figure 4.10.	Schematic representation of CVD synthesis of the crystalline boron nanoparticles	60
Figure 4.11.	TEM images show increased boron nanoparticles' sizes by increasing BBr_3 volatilizing temperatures: 0 °C (a), 10 °C (b), and 20°C (c). Size	

distributions of those boron nanoparticles are shown in (d) through (f) accordingly.....	62
Figure 4.12. XRD patterns for the boron nanoparticles before (black, bottom) and after (red, top) oxidization. Inset: TEM image of a boron-B ₂ O ₃ composited nanoparticles.....	64
Figure 5.1. TEM images of the Y ₂ O ₃ NS (a), Y ₂ O ₃ NP (b), and Y ₂ O ₃ NW used in experiments.....	68
Figure 5.2. Under different friction tests, comparison of friction coefficient of mineral oils without (black curve) and with different types (colored curves) of Y ₂ O ₃ nanomaterials additives (0.5 wt %)......	69
Figure 5.3. Under different friction tests, comparison of friction coefficient of mineral oils without (black curve) and with different concentrations (colored curves) of Y ₂ O ₃ NS additives.....	71
Figure 5.4. Under different loads, comparison of friction coefficient of mineral oils without (black curve) and with 0.5 wt % of Y ₂ O ₃ NS additives (red curve).....	74
Figure 5.5. Under different loads, comparison of friction coefficient of mineral oils without (black curve) and with 0.5 wt % of α -ZrP nanoplatelet additives (green curve)......	76
Figure 5.6. Under different speeds, comparison of friction coefficient of mineral oils without (black curve) and with 0.5 wt % of Y ₂ O ₃ NS additives (red curve).....	78
Figure 5.7. Under different speeds, comparison of friction coefficient of mineral oils without (black curve) and with 0.1 wt % of α -ZrP nanoplatelet additives (green curve)......	79
Figure 5.8. Example comparison of friction coefficient of DI water without (middle black curve) and with 0.1 wt % (top blue curve) and 0.002 wt % (bottom green curve) of α -ZrP nanoplatelet additives.....	81
Figure 5.9. (a) Comparison of infrared spectra of α -ZrP nanoplatelets (top red curve), mineral oil (bottom black curve), and mineral oil containing 0.5 wt % α -ZrP nanoplatelets (middle green curve). (b) Comparison of Raman spectra between α -ZrP nanoplatelets (top red curve) and mineral oil containing 0.5 wt % α -ZrP nanoplatelets (bottom green curve). (c) Comparison of Raman spectra between mineral oil	

containing 0.5 wt % α -ZrP nanoplatelets (top green curve) and pure mineral oil (bottom black curve).....	82
Figure 5.10. (a) Schematics showing interaction between lubricant molecules and α -ZrP surface (the left), and formation of dipole-dipole complex (the right). (b) Schematic explanation of friction reduction with localized asperity-contact.	84
Figure 5.11. Changes of WIWNU before (black) and after (gray) CMP using different slurries.....	87
Figure 5.12. The arithmetic averaged surface roughness of wafers that are polished using different slurries.	88
Figure 5.13. The Cu dishing in wafers that are polished using different slurries.	88
Figure 5.14. Results of friction between the Cu film and the polishing pad in SiO ₂ NP (black, top) and Y ₂ O ₃ NS (red, bottom) slurries.....	89
Figure 5.15. Results of rheological measurements: (a) the comparison of shear stress-shear rate plots in different slurries with different abrasive concentrations; (b) variation of shear stress to shear rate in SiO ₂ NP slurries with different concentrations; (c) the clear comparison of shear stress-shear rate plots in different slurries with the same abrasive concentration (3 wt %); (d) variation of shear stress to shear rate in Y ₂ O ₃ NS slurries with different concentrations.	90
Figure 5.16. Schematic representations of abrasion modes using the commercial SiO ₂ NP (inset) slurry (a) and the Y ₂ O ₃ NS (inset) slurry (b).	92
Figure 5.17. Five pyramidal micro-indentations on the Cu coated Si wafers prepared for CMP.	94
Figure 5.18. AFM images before and after CMP in different slurries (as labeled).....	96
Figure 5.19. Averaged micro-indent depth on Cu films before and after CMP in different slurries.....	97
Figure 5.20. Comparison of materials removal rate using different CMP slurries.....	97
Figure 5.21. Comparison of coefficient of friction for CMP experiments conducted in different slurries.....	99
Figure 5.22. 2D nanostructured B ₂ O ₃ -induced surface improvement during CMP (left); layered nanostructure of B ₂ O ₃ (right).....	100

Figure 5.23. Surface roughness on Cu films before and after CMP in different slurries.....	101
Figure 6.1. (a) A Stribeck curve with different lubrication regimes schematically showing in inset; (b) Example comparison of friction coefficient in different lubricant regimes using mineral oils; the applied loads and the rotational speeds used in the experiments are labeled in the figure.....	105
Figure 6.2. Plotting Stribeck curves of different lubricants using the average coefficient of friction.	106
Figure 6.3. (a) Comparison of Stribeck curves using mineral oils without (black curve) and with different types (colored curves) of Y_2O_3 nano-additives (0.5 wt %). (b) Comparison of friction coefficient using mineral oils without (black curve) and with different concentrations (colored curves) of Y_2O_3 NS additives	108
Figure 6.4. Diagram schematically showing the transition from boundary-lubrication regime to mixed- or hydrodynamic-lubrication regime with relatively high concentration (1 wt %) of Y_2O_3 NS additives	108
Figure 6.5. (a) Comparison of Stribeck curves using mineral oils without (black curve) and with different concentrations (colored curves) of α -ZrP nanoplatelet additives. (b) Comparison of Stribeck curves using DI water without (black curve) and with different concentrations (colored curves) of α -ZrP nanoplatelet additives.....	109
Figure 6.6. (a) Variation of viscosity with shear rate in mineral oil (top black plot), and with addition of different types (colored curves) of Y_2O_3 nano-additives (0.5 wt %). (b) Variation of viscosity with shear rate in mineral oil (top black plot), and with addition of 0.5 wt % (middle red plot) and 0.1 wt % (bottom green plot) Y_2O_3 NS additives.....	111
Figure 6.7. (a) Variation of viscosity with shear rate in mineral oil (top black plot), and with addition of 0.5 wt % (middle red plot) and 0.1 wt % (bottom green plot) α -ZrP nanoplatelet additives. (b) Variation of viscosity with shear rate in DI water (top black plot), and with addition of 0.002 wt % (middle red plot) and 0.0004 wt % (bottom green plot) α -ZrP nanoplatelet additives.....	112
Figure 6.8. Under a constant shear rate ($10,000\text{ s}^{-1}$), (a) reduction in viscosity of mineral oil (top black plot) in the presence of Y_2O_3 NS with concentrations of 0.5 wt % (middle red plot) and 0.1 wt % (bottom green plot); (b) reduction in viscosity of mineral oil (top black plot) in the presence of α -ZrP nanoplatelets with concentrations of 0.5 wt %	

(middle red plot) and 0.1 wt % (bottom green plot); (c) reduction in viscosity of DI water (top black plot) in the presence of α -ZrP nanoplatelets with concentrations of 0.002 wt % (middle red plot) and 0.0004 wt % (bottom green plot)	114
Figure 6.9. Designating surface stresses on a fluid element.	115
Figure 6.10. Lubricant flow between two parallel flat plates (top: pin; bottom: disk) .	118
Figure 6.11. Flow-rate profile of pure lubricant flow	120
Figure 6.12. (a) Rotation (or spin) of the spherical nanoparticle under flow shearing; (b) flow distribution close to the nanoparticle surface; (c) flow-rate profile in lubricant that contains the nanoparticle additive.....	121
Figure 6.13. (a) Rotation of the 2D nanosheet under flow shearing; (b) flow-rate profile in lubricant that contains the 2D nano-additive; (c) flow distribution close to the nanosheet surface	123
Figure 6.14. (a) Inclined Y_2O_3 NS in mineral oil modeled in a rectangular shear cell with periodic boundary conditions. (b) Total viscosity of the fluid matrix without and with a single inclusion of inclined Y_2O_3 NS at different degrees (0° , 2° , 4° , 6° , 8° , and 10°), under a constant shear rate ($10,000 \text{ s}^{-1}$). (c) Total viscosity of the fluid matrix without and with a single inclusion of Y_2O_3 NP and inclined Y_2O_3 NS	127
Figure 6.15. (a) Schematic top-view (the left) and side-view (the right) showing inclined alignment of the 2D nano-additives in the lubricants. (b) Schematic explanation of lubrication improvement via viscosity modification.	128

LIST OF TABLES

	Page
Table 1.1. Current 2D nanomaterials library.....	20

CHAPTER I

INTRODUCTION

This chapter provides information necessary to understand background of the thesis research regarding lubricant additives and viscosity modification. The state-of-the-art in two-dimensional (2D) nanomaterials is briefly discussed.

1.1. Lubricant additives

Friction and wear dominate the efficiency, energy consumption, heat generation, and lifetime of machinery. In a passenger car, for example, one-third of the fuel energy is consumed to overcome friction in the brakes, engine, tires, and transmission (Figure 1.1).¹ Lubrication is known as a process that a friction/wear-reduction film supports a sliding load. The substance that composes the film is a lubricant. Lubricants are consisted of an additives package and a base fluid or fluid-like material. The additive percentage varies from 20 % or more to several hundredths of a percent. Lubricants must possess certain desirable properties, such as slipperiness, proper viscosity, good dispersing and cleaning capability, low pour point, corrosion inhibition, weak volatility, low flammability, and nontoxicity. Various additives have been reported to improve such.²⁻⁴ There is at least one additive in all practically used lubricants. As summarized in Figure 1.2, these additives can be categorized into five types: deposit-control, film-forming, anti-wear, miscellaneous, and viscosity modification. Details of each additive will be discussed as follows.

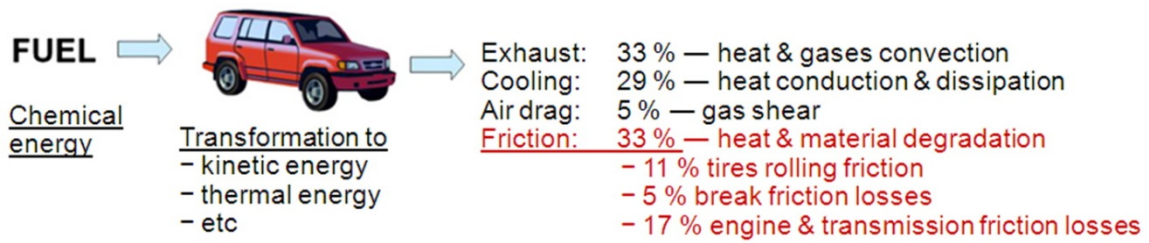


Figure 1.1. Fuel energy consumption in passenger cars. Reprinted from reference¹ with permission from Elsevier (Copyright © 2012).

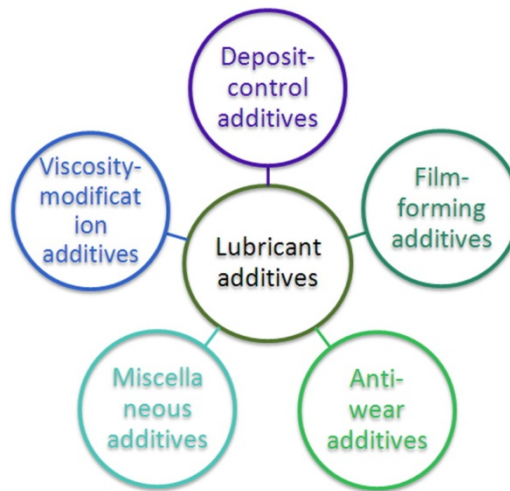


Figure 1.2. Classification of lubricant additives.

1.1.1. Deposit-control additives

The deposit-control additives enable lubricants to work in a clear environment by preventing precipitates from oxidation, wear, and other friction-induced reactions.³

Generation of deposits during lubrication is a major cause that induces operating malfunction. Deposit-control additives include antioxidants, zinc dithiophosphate (ZDDP), and dispersant and detergent.

1.1.1.1. Antioxidants

Oxidative or thermal degradation of base liquids results in formation of deposits like sludge, carbon, lacquer, varnish, soot, etc. At high temperature, the degradation is caused by nitrogen oxides (NO_x) and un-reacted oxygen due to partially combustion of fuels (Figure 1.3a). As a consequence, oxygenated products form as precursors resulting in oil insoluble deposits. Figure 1.3b shows mechanism how deposit precursors form. The formation of deposit precursors is initiated by radical generation. Rearrangement or disproportionation to carbonyl and olefinic groups in lubricants undergoes during the precursor formation. Carboxyl and hydroxyl groups-functionalized precursors are capable of polymerizing certain molecules in lubricants to high molecular weight products. Polymerization of the oil-insoluble products leads to formation of resin. Resin, consisting of highly oxygenated hydrocarbon, is critical in the formation of deposits (Figure 1.3c). The resin is oil-soluble when its non-polar to polar ratio is high. The dissolving process results in an increased viscosity by oil thickening. If the ratio is low, the resin becomes insoluble in lubricants. Varnish exists when the resin forms on a hot metal surface. In the presence of solids, water, and carbon, sludge forms from oil-insoluble resin.

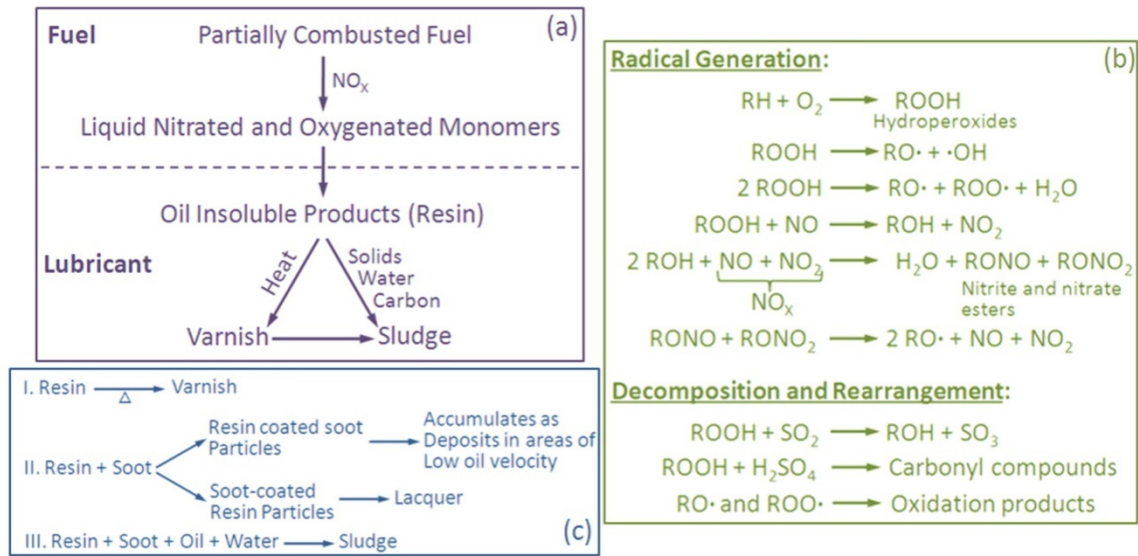


Figure 1.3. (a) Deposit-formation mechanism. (b) Formation of deposit precursors. (c) Interaction between deposit-forming products.

Generally, oxidation progress occurs following equations (1.1) through (1.2) continuously and repeatedly. Oxygen-bearing compounds and unsaturated hydrocarbons form via branching reactions of hydroperoxide molecules [equation (1.4)]. The resultant high molecular-weight polymers are insoluble in the lubricants. Meanwhile, neutralization of the unsaturated hydrocarbons forms more oxygen-bearing compounds, e.g. acids, ketone, aldehydes, etc.



In order to get rid of deposit during the lubrication, resistance to oxidation needs to be enhanced. Antioxidants are used to delay onset of the oxidation and minimize the

oxidative degradation. There are three types of antioxidants: primary antioxidants (PA, radical scavengers), secondary antioxidants (SA, peroxide decomposers), and metal deactivators (MD, chelating agents). PA inhibits the chain oxidizing reactions by donating hydrogen atoms to stabilize the radicals. Hindered aromatic amines and phenolics are two major classes of PA additives. SA reduces the peroxides and represses the oxidization. Phosphorus and/or sulfur compounds, thio-ethers, and phosphites are examples of SA additives. MD reduces chemical activity of the metal ions via forming a stable coordination complex with chelating agents. The MD additives show the antioxidant capability as well. Nowadays, many antioxidants have been widely used in metal-working fluids, hydraulic fluids, greases, gear oils, and engine oils. They are: phosphorus/sulfur compounds, boron compounds, hindered phenolic compounds, aromatic amine compounds, and organometallic compounds (metals: alkaline metals, molybdeum, copper, zinc, etc).

1.1.1.2. Zinc dithiophosphate (ZDDP)

ZDDP $[(4(\text{RO})_2\text{PS}_2)_2\text{Zn}]$ is a family coordination complex, in which zinc chelates with the anion of dithiophosphoric acid. The zinc atom is sp^3 hybridized coordinate with four sulfur atoms. Zn-S chelating arrangement in monomeric ZDDP is symmetrical (Figure 1.4 a). In lubricants, ZDDP molecules presents as oligomer, tetramer (Figure 1.4b), trimer, or dimer, as well.

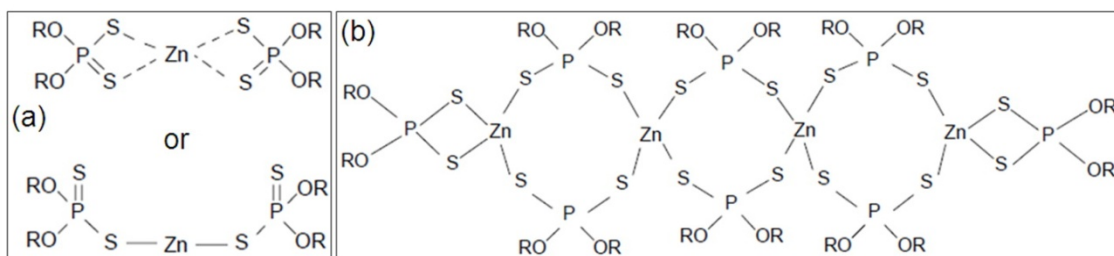
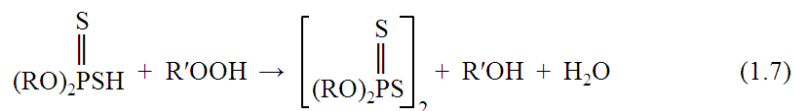
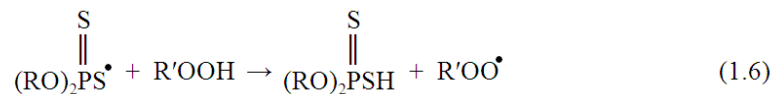
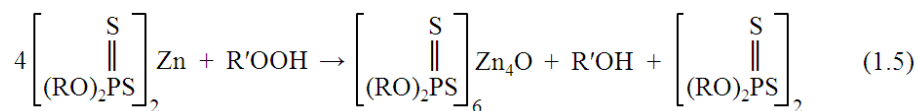


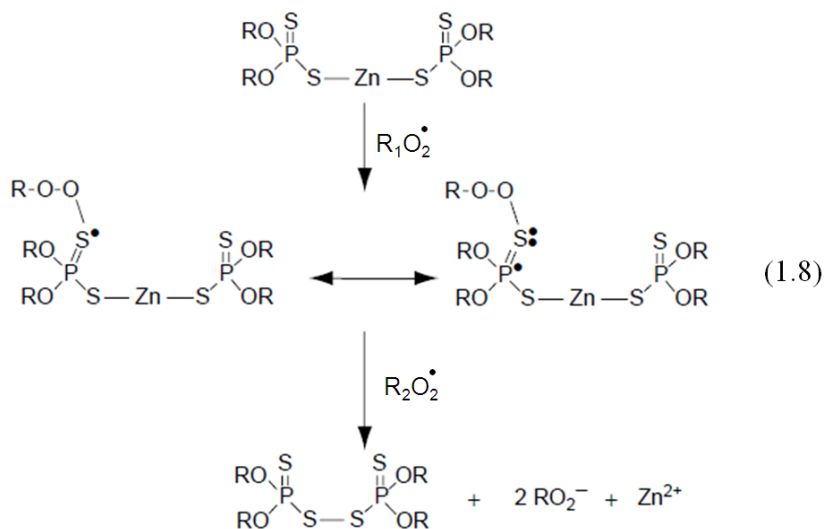
Figure 1.4. (a) Symmetrical molecular structures of monomeric ZDDP. (b) Molecular structure of ZDDP tetramer. R = alkyl, phenyl, or alkylphenyl.

Affinity of ZDDP to alkyl hydroperoxides and peroxy radicals entails its deposit-control capability. When the alkyl hydroperoxides exist in lubricants, ZDDP can be oxidized. Basic ZDDP salt forms through its rapid initial reaction (1.5) with the hydroperoxide (R'OOH). The alkyl hydroperoxide decomposition occurs via its reaction (1.6) with dialkyldithiophosphoryl radical, leading to formation of dialkyldithiophosphoric acid. Inert oxidizing products then form via a reaction (1.7) of the alkyl hydroperoxide with the dialkyldithiophosphoric acid. The oxidation products are dialkyldithiophosphoryl sulfides, which have little reactivity as antioxidant.



Furthermore, ZDDP can inhibit the oxidation of lubricants by reacting with peroxy radicals [see reaction (1.8)]. Dithiophosphate radicals form by reacting ZDDP

with the alkyl peroxy radical ($R_1O_2^\bullet$). Another dithiophosphate radical ($R_2O_2^\bullet$)-assisted intramolecular dimerization of the dithiophosphate radical leads to formation of dialkyldithiophosphoryl disulfide. The disulfide is inert to the oxidation. As an antioxidant, ZDDP not only destroys the alkyl hydroperoxide, but also acts as an alkyl radical scavenger.



1.1.1.3. Dispersant and detergent

Suspension of unwanted oxidization-produced deposits is an important property for lubricants. Dispersant and detergent are used as the additives to suspend the deposits in lubricants. About 40 vol % of a practical lubricant is made up with the dispersants and detergents. Associating with extra base, metal salts of organic acids are the most common detergents used in lubricants. Calcium, magnesium, potassium, and sodium are the extensively used metals in detergents. The so-called "soap" is the organic groups from the detergent. Detergent molecules contain an oleophilic hydrocarbon group and a

polar group (Figure 1.5a). The polar group can be selected from carboxylate, phenate, and sulfonate. As discussed above, lubricant oxidation results in the formation of oxygenated materials, such as ketones, aldehydes, and acids. In the presence of detergents, polar oxidizing deposits are suspended in the lubricant (Figure 1.5b), while the oxidation-generated acids are neutralized. Dispersants are high-molecular-weight polymers with the similarly functionalized/polarized end groups. Dispersants are capable of suspending non-acidic oxidizing deposits, e.g. resinous oxygenates, aldehydes, and alcohols. The suspension of deposits by dispersants occurs in five different ways: 1) decrease of interface/surface energy of the polarized species; 2) inclusion of the undesirable species in micelles; 3) prevention of colloids from agglomeration; 4) modification of surface of soot particles; and 5) elimination of the deposit adherence to metal surfaces.

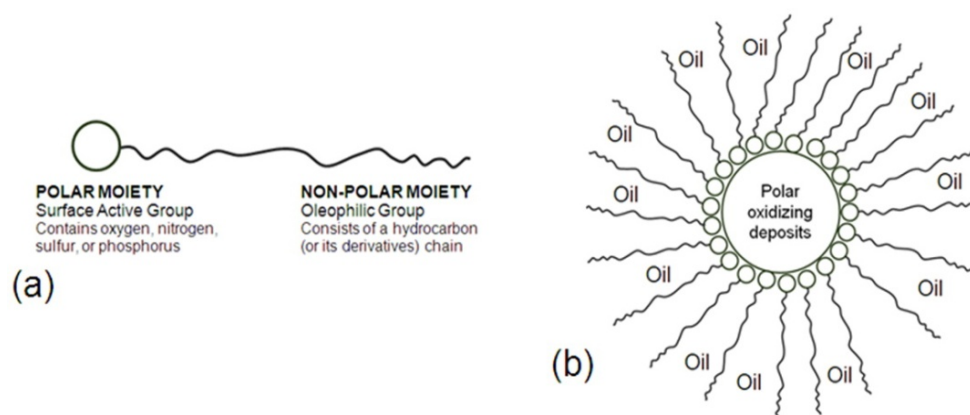


Figure 1.5. (a) A typical detergent molecular structure. (b) Polarized oxidizing deposit is suspended in lubricant oil.

1.1.2. Film-forming additives

In order to save energy and minimize wear, film-forming additives are used to reduce friction in lubricants via forming either a dry or a wet film on solid surfaces. As shown in Figure 1.6a, the solid surfaces interact with such additives via chemical reaction, chemical adsorption (chemisorption), or physical adsorption (physisorption).^{5,6} The interacting strength of chemical reaction is stronger than chemisorptions, which is in turn stronger than physisorption. Both organic and inorganic film-forming additives have been widely used in lubricants. Common organic film-forming additives include: 1) Polytetrafluoroethylene (PTFE); 2) sulphurized hydrocarbons and fats; 3) dithiophosphoric, dithiocarbamic, or carboxylic acid coordinated transition metallic complexes; 4) phosphorous or phosphoric acid and alcohol esters; and 5) carboxylic acids, amines, fatty alcohols, and their derivatives. The organic film-forming molecule consists of a long-chain hydrocarbon or its derivatives and a functionalized end group. The molecular chains extend to the lubricant while the end group interacts with the solid surface (Figure 1.6b). The interaction of a metal surface with the organic film-forming additives is schematically shown in Figure 1.6c.

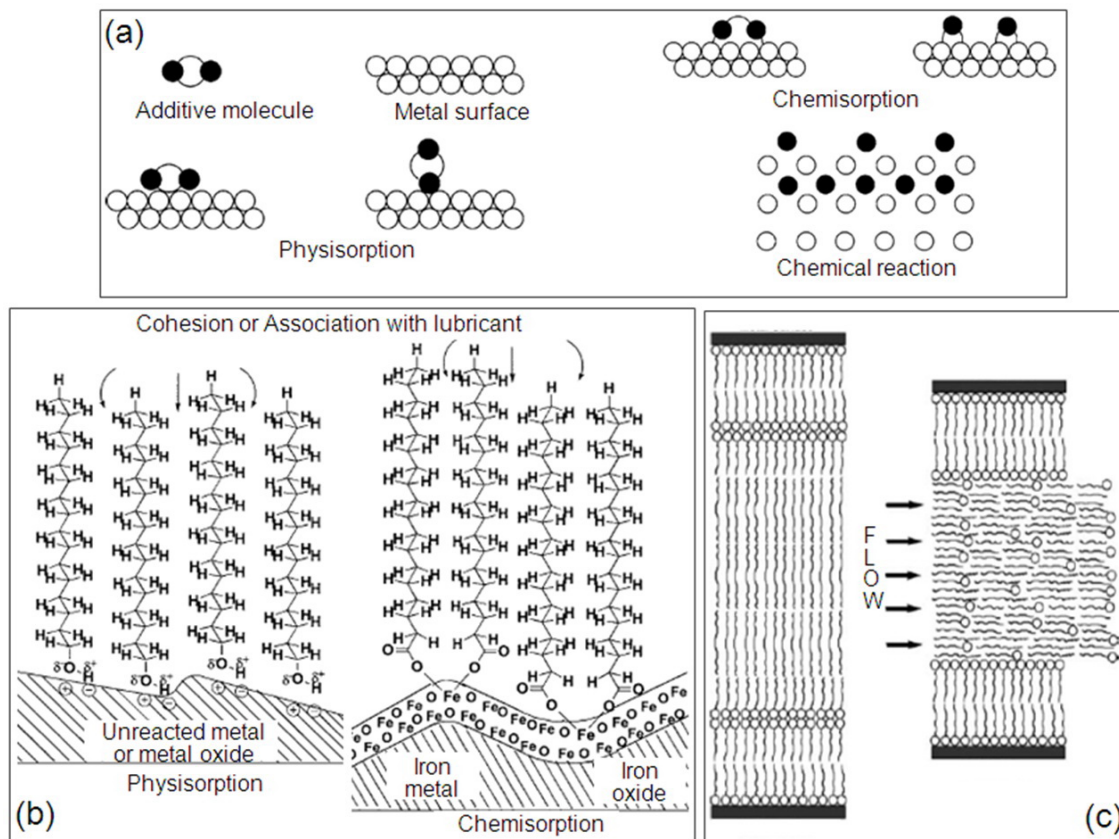


Figure 1.6. (a) Surface-additive interacting mode;⁵ (b) additives adsorption on the metal surface;⁷ (c) interaction of a metal surface with the organic film-forming additives.⁷

In addition, layered inorganic materials, e.g. MoS₂, WS₂, h-BN, and graphite, are another type of film-forming additives. Such solid lubricants are able to prevent the mating surface from asperity contact via exfoliation of their layered structures (Figure 1.7). As effective friction modifiers, film-forming additives should meet the following requirements: 1) The layered additives must orient parallel to the lubricant flow; 2) Yield strength along the sliding direction should be low enough for a small friction coefficient; 3) The adhesion to substrate should be higher than the shear forces loaded to the film;

and 4) Continuous lubricant film should be maintained with the addition of film-forming additives, in which plastic deformation of lubricant molecules is avoided.

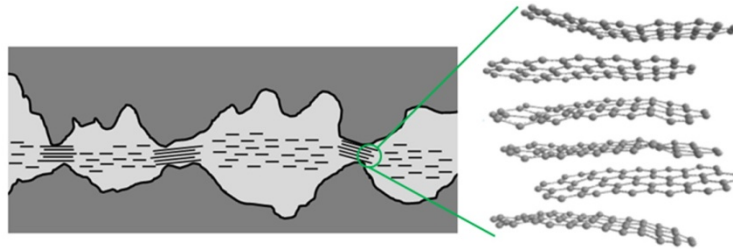


Figure 1.7. Exfoliation of the inorganic film-forming additive.

1.1.3. Anti-wear and extreme-pressure additives

Under the conditions of high load, low speed, or little viscosity, high asperities on the mating surfaces interact with each other. This occurs initially through an elastohydrodynamic-lubrication (EHL), and later via a direct contact. The asperity interaction leads to friction and wear on the mating surfaces. Anti-wear additives are introduced, especially under extreme-pressure, to reduce wear and keep the mating surfaces from seizure. Anti-wear additives protect the surfaces in various ways: some chemically bond with the surface and modify the material removal process; some establish replenishable surface layer reducing the local shear stress; the others deposit thick layers on the surfaces to prevent the asperity contact. Organophosphorus and organosulfur compounds (Figure 1.8) are the most widely used anti-wear additives.^{8,9} Lead compounds that are coordinated with carboxylic acids are usually used with sulfur-

based compounds. Oil-soluble chlorinated and phosphorous-sulfur substances perform well as anti-wear additives as well.

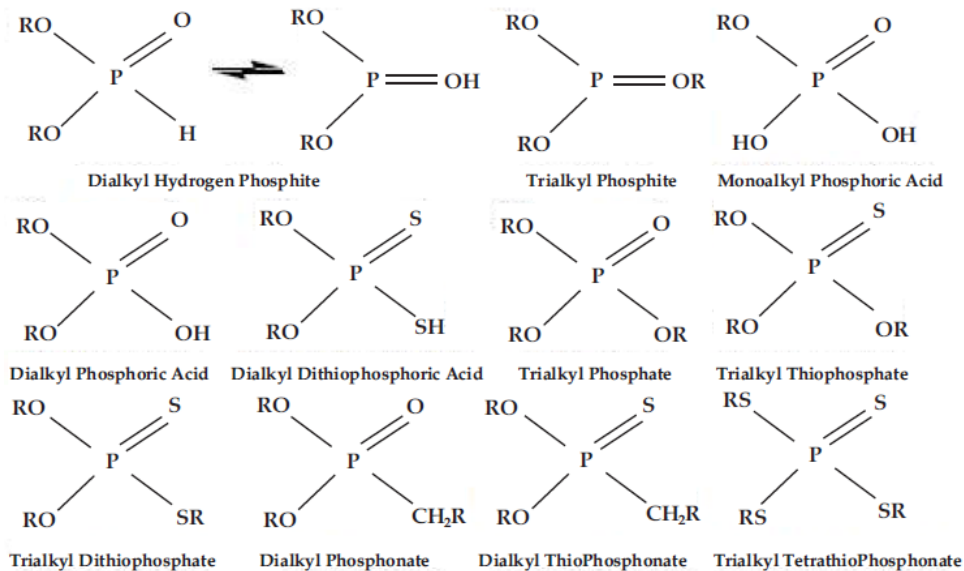
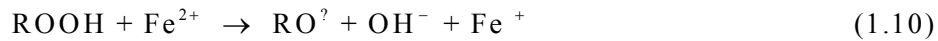
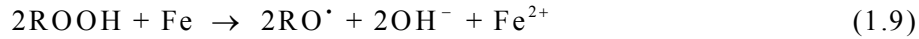


Figure 1.8. Commonly used anti-wear additives.³

In addition, discovery of ZDDP is one of the most important advances in anti-wear additives. Asperities react with the ZDDP to reduce the possibility of the contacts between mating surfaces. Thermal degradation of ZDDP leads to the formation of sulfur, which reacts with metal surfaces resulting in a thin layer of sulfide. Simultaneously, with incorporation of sulfur, phosphate from ZDDP reacts with metal to produce an amorphous meta-phosphate layer. In such a “glass” phosphate region, metallic cations are neutralized, and stabilization on metal surface is obtained. The anti-wear efficiency of ZDDP is highly dependent on the surface rubbing extent and the operating temperature. In addition, wear rate is found to be directly proportional to the

concentration of alkyl hydroperoxide in lubricants.¹⁰ This is because that oxidation of ferrous metals happens through reactions (1.9) and (1.10). The ZDDP and its derivatives are capable of neutralizing the hydroperoxides via reactions (1.5) through (1.8). Wear rate is thus reduced due to the addition of ZDDP.



Under extreme pressure, anti-scuffing additives are used to protect metal surface from forming metallic compounds. After chemical-thermo reaction between metal surface and anti-scuffing additives, an extremely durable protective layer is formed on the mating surfaces. This layer is able to withstand ultra high pressures and temperature. Scoring and seizing between the mating surfaces are effectively eliminated. The metallic compounds have high resistance to sliding-shear. However, the anti-scuffing additives have strong reactivity. Corrosion and metal fatigue are the adverse effects that are often encountered using the anti-scuffing additives. Extreme cautiousness must be taken when utilizing anti-scuffing additives under high pressure.

1.1.4. Miscellaneous additives

The lubricating process often faces problems like grease stringiness, lubricant adherence, fluid leakage, surface adsorption, and corrosion. Miscellaneous additives are thus added to solve such problems. They are tackifiers,¹¹ antimisting agents,¹² seal swelling agents,¹³ surfactants,¹⁴ and corrosion inhibitors.^{15,16} Tackifier is used as additive to provide stringiness for a lubricant to a substance. Common tackifiers are soluble high

molecular-weight polymers with vegetable- or mineral-based diluents. In order to ensure the tackifier solution is tacky, its molecular chain should be good at extension in lubricants. This implies that the conventional tackifiers can be used as antimisting additives.² Seal swelling additives are used in lubricant to prevent seal failure. Most common seal-swelling additives are tris-phosphite ester, dihexylphthalate, tridecyl alcohol, di-2-ethylhexylsebacate (DOS), and di-2-ethylhexylphthalate (DOP). In particular, surfactants are critical ingredients for lubricants, and their microstructures assembled in liquid are shown schematically in Figure 1.9. Their main functions include defoaming, dispersion, (d)emulsification, and solubilization. Finally, various types of corrosion occur when lubricants are used. As several organic acids have been used as lubricant additives, it is indeed necessary to enhance corrosion resistance of the substrate metals using corrosion inhibitors. A passivated surface forms on metal surface by reacting the corrosion inhibitor with the bearing substrate. Such a protective layer keeps corrosive ingredients in lubricant from attacking or approaching the metals. The corrosion-resistant surface is bonded to the metal chemically or adsorbed on it physically. Corrosion inhibitors can be oxygen scavenger, hydrogen poisons, cathodic inhibitor, anodic inhibitor, or (non-)oxidizing anion. They are typically selected from nitrites, chromates, oxidates, sulfonates, phosphates, hydrazine, carboxylates, alkyl amines, amine salts, Na_3AsO_4 , As_2O_3 , and nitrogen-ring-structured.

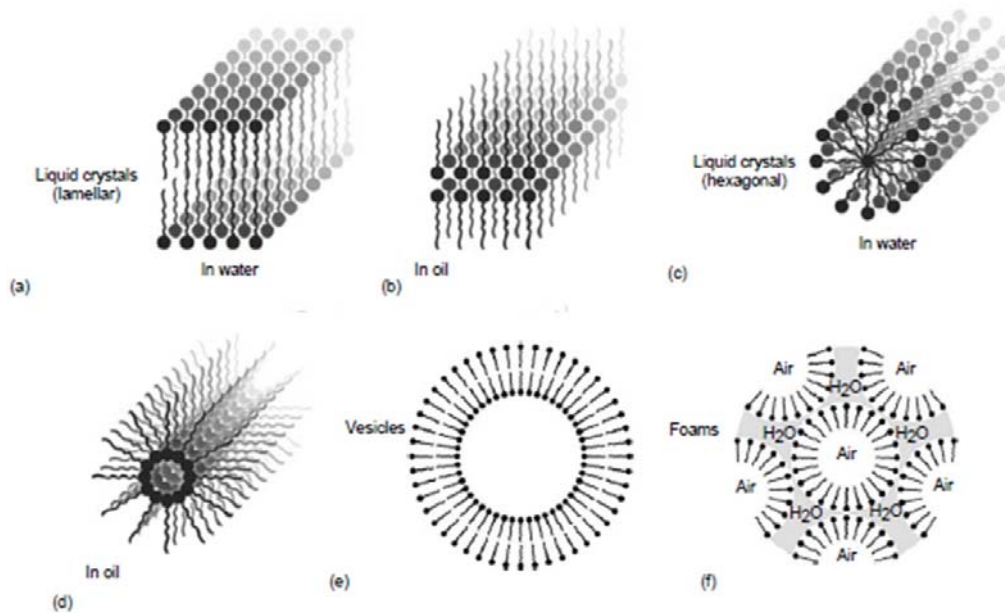


Figure 1.9. Surfactant microstructures assembled in liquid.²

1.2. Viscosity modification for lubricants

Viscosity is a property that determines the lubricant film thickness as well as its rheological behavior.¹⁷ Unlike the lubricant additives discussed above, viscosity modifiers are the only additives that can significantly affect the fluid dynamic behaviors of the lubricants. Particularly in hydrodynamic lubrication regime, fluid dynamic property of the lubricant dominates the lubricating efficiency and affects the energy consumption. Generally, friction is small when the viscosity of the lubricant is low, provided that the gap between two mating-sliding surfaces is fully filled with a liquid lubricant. This research aims at developing a new method to modify the viscosity of a lubricant, and finally improve its tribological performances.

1.2.1. Organic viscosity modifiers

Traditionally, viscosity-modification additives are used to improve viscosity-temperatures performance of lubricants.^{18,19} Pour point depressant (PPD) and oil-soluble-polymers, such as olefin copolymers (OCP), polyisobutylene (PIB), styrene isoprene copolymer (SIC), styrene butadiene copolymer (SBC), and polymethacrylates (PMMA), are used as organic viscosity modifiers. For most lubricants, viscosity decrease with temperature. The polymer molecules listed in the left of Figure 1.10a could expand with temperature and counteract the oil thinning. This would lead to a decent viscosity at relatively high temperature, as shown in the right of Figure 1.10a. On the other hand, industrial lubricants often contain some dissolved wax. A rigid wax crystal structure forms as the lubricant is chilled (the left in Figure 1.10b). When an oil or fuel is cooled to certain temperature, it will stop flowing. The temperature is the pour point. Pour point depressant (PPD) is the second type of organic viscosity modifiers. By inserting the organic molecule branches into the rigid wax structure (the middle in Figure 1.10b), interlocking reduction enables the lubricant to flow at low temperature with low viscosity (the right in Figure 1.10b). When lubricants are used at a fixed temperature, such organic additives are unable to effectively modify the viscosity.

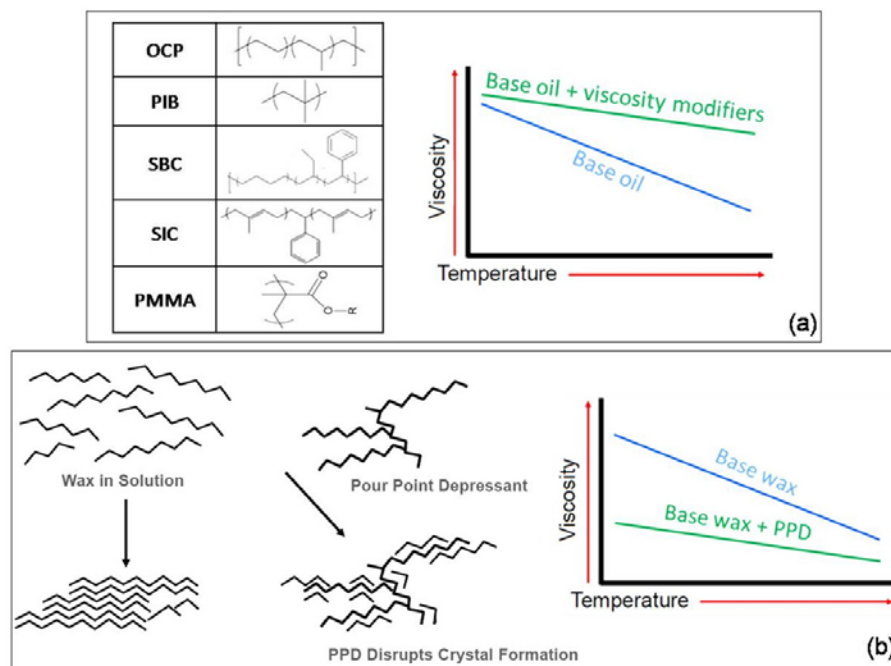


Figure 1.10. Viscosity-temperature properties of lubricants using polymers (a) and PPD (b).

1.2.2. Einstein relationship between additives and viscosity

The rheological properties of colloidal suspensions have garnered increased interest in a wide array of fluidic and tribological disciplines. Einstein predicted the viscosity of low-concentration hard-sphere suspended liquids, which initiated the long history in studying the rheology of suspensions.²⁰⁻²⁵ Einstein's theory only permits the viscosity of a suspension to increase linearly with the addition of particulates. Einstein's relationship has been extensively studied experimentally,^{26,27} theoretically,²⁸⁻³³ and through computational simulations.^{34,35} The rheological performance of the suspension is dependent on hydrodynamic phenomena solely, when the size of particulate additives is large (\sim several μm).^{36,37} The viscosity increases with the volume fractions since the colloidal effect is ignored. For the suspension of non-Brownian spherical inorganic

particles, viscosity increases with the additives due to shear migration, particle roughening, hydrodynamic-assisted aggregation, shear-induced particle pressure, and anisotropic radial suspension.³⁸⁻⁴⁴ Rheological investigation becomes complicated, when the non-spherical particles are investigated. Particles are found to gel when their aspect ratios are very low or very high.⁴⁵ For example, flocculation of rod-like nanoparticles is believed to increase viscosity of the suspension,^{45,46} while shear thickening is observed for non-spherical particles-suspended colloids.⁴⁷ In the presences of the non-spherical particles, extensional and shear flows become pronounced, from which the high viscosity can be understood by interpreting the suspension hydrodynamic fluid behavior.

Additionally, additives are often suspended in surfactant solutions and polymer solutions or melts in various applications. The flow structure impacts the variation of viscosity significantly due to the viscoelasticity of the dispersing medium. Under shearing, string-like flow structure is developed in a viscoelastic polymer solution by suspending particles in it.⁴⁸ The shape of particle is critical for viscosity increase in such viscoelastic suspension. When mono-dispersed organic particles are added in a viscoelastic liquid, viscosity is increased due to the suppression of extensional flow.⁴⁹ Grafting density on the surface of inorganic nanoparticles affects the fluid dynamic behavior of a polymer melts. Aggregation of the nanoparticles induces the increase in viscosity due to repression of free length of the polymer chain.^{50,51} In brief, conventional particulate additives show the viscosity increase for the base liquid under shearing or sliding. In order to obtain an efficient lubrication and save energy consumption, the additives that can reduce the viscosity of lubricants are highly desirable.

1.2.3. Non-Einstein-like viscosity reduction

Recent studies suggested that the addition of organic nanoparticles could affect the viscosity of a fluid in ways that do not follow linear Einstein's model.⁵²⁻⁵⁴ In the polymer suspension, if the correlation length of the organic molecules becomes comparable with the size of the suspended particles, abnormal viscosity reduction is obtained. This is due to the additives-induced change in free volume and conformation of the polymer by minimizing the extraneous enthalpic effects.⁵⁵ Such a viscosity reduction is promising in optimize performance of the lubricants. It is noted that sheet- or platelet-like 2D nano-particles have been studied as interfaces between two liquids or liquid and gas.^{36,37} In solid-stabilized emulsions, the interfacial adsorption on layered structure is able to suppress the droplet coalescence.⁵⁶ Due to the large surface area, emulsions could be well stabilized by using the 2D shaped additives, resulting in a viscosity reduction. Capillary force-driven particle bridging is crucial for the suspension of nanoparticles in colloids.⁵⁷⁻⁵⁹ The sheet-like 2D nano-additives could eliminate particle aggregation and effectively modify its viscosity.⁶⁰ Therefore, lubricant performance would be improved, if a non-Einstein-like viscosity additive is used in it. As briefly discussed here, sheet-like 2D nanomaterials could be a proper candidate for the desirable viscosity modification in the liquid lubricants. The 2D nanomaterials that may be suitable for this research are being concisely reviewed in the following section.

1.3. Two-dimensional nanomaterials

Recently developed nanomaterials additives are promising in enhancing lubricating efficiency.⁶¹⁻⁶⁷ The two-dimensional (2D) nanomaterials have been studied extensively as solid lubricants.⁶⁸⁻⁷⁴ Their common characteristic is the layered structures. Within each atomic layer, covalent bonding bonds atoms together, and van der Waals interaction presents between two adjacent layers. Their applications as lubricant additives focused on film-forming additives mainly.^{65,75-79} Little attention has been paid to the capability of 2D nanomaterials in modifying the lubricants' fluid dynamics. Some representative 2D nanomaterials are summarized in Table 1.1.

Table 1.1. Current 2D nanomaterials library. Some representative structures are listed.

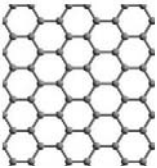
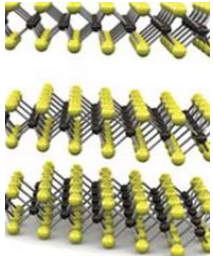
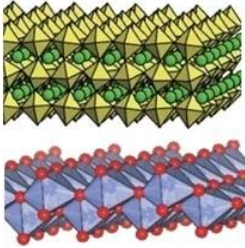
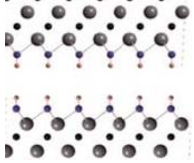
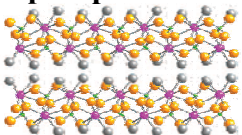
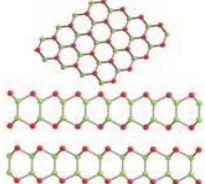
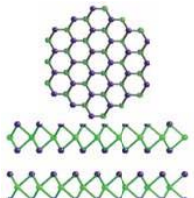
2D category & representative structure	Representative materials	References
Graphene family 	<ul style="list-style-type: none"> ➤ Graphene, Fluoro-graphene, Graphene oxide, BCN, h-BN (white graphene). 	80-87
2D Chalcogenides 	<ul style="list-style-type: none"> ➤ MoS₂, WS₂, MoSe₂, WSe₂. ➤ Semiconducting chalcogenides: MoTe₂, WTe₂, ZrS₂, ZrSe₂, TiS₂, VSe₂, GaSe, GaTe, InSe, Bi₂Se₃, Bi₂Te₃, Bi₂MnTe₄, etc. ➤ Metallic dichalcogenides: NbSe₂, NbS₂, LaSe, TaS₂, NiSe₂, etc. 	88-94 95-107 108-112

Table 1.1 (Continued)

2D category & representative structure	Representative materials	References
<p>2D Oxides and hydroxides</p> 	<ul style="list-style-type: none"> ➤ Micas, BSCCO, MoO₃, WO₃, TiO₂, MnO₂, V₂O₅, TaO₃, RuO₂, Y₂O₃, B₂O₃, TiNbO₅, K_{0.8}H_{3.2}Nb₆O₁₇, etc. ➤ Perovskite-type: LaNb₂O₇, (Ca,Sr)₂Nb₃O₁₀, La_{0.90}Eu_{0.05}Nb₂O₇, Bi₄Ti₃O₁₂, Bi₂SrTa₂O₉, Ca₂Ta₂TiO₁₀, Bi_{3.25}La_{0.75}Ti₃O₁₂, K₂NbO₃F, etc. ➤ Hydroxides: Ni(OH)₂, Sm(OH)₃, Er(OH)₃, Eu(OH)₃, Y(OH)₃, Co-Al(OH)_x, Mg-Al(OH)_x, etc. 	<p>113-124</p> <p>125-132</p> <p>133-139</p>
<p>2D MAX phases</p> 	<ul style="list-style-type: none"> ➤ Ti₃AlC₂, Ti₂AlC, Ta₄AlC₃, (Ti_{0.5}Nb_{0.5})₃AlC, (V_{0.5}Cr_{0.5})₃AlC₂, Ti₃AlCN, etc 	<p>140-145</p>
<p>2D Phosphonates or phosphates</p> 	<ul style="list-style-type: none"> ➤ CaHPO₄, Zr(HPO₄)₂, Zr(PO₄)(H₂PO₄), etc 	<p>146-148</p>
<p>2D III-VI semiconductor</p> 	<ul style="list-style-type: none"> ➤ Gas, GaSe, GaTe, InS, InSe, InTe, etc. 	<p>149-151</p>
<p>2D Metal halides</p> 	<ul style="list-style-type: none"> ➤ MoCl₂, α-RuCl₃, CrCl₃, BiI₃, PbCl₄, etc 	<p>152-154</p>

Among the 2D nanomaterials listed in Table 1.1, graphene is the most common component in van der Waals heterostructures and devices.⁸⁰ Graphene can be described as one or several-atom thick layer of graphite, making of carbon atoms in a honeycomb lattice. Many physical properties in graphene exceed that in any other materials, and some of them even reach the theoretical limits.^{83,155-158} Fluorographene, graphene oxide, and boron carbon nitride (BCN) are three graphene derivatives that are also widely used as 2D nanomaterials. Fluorination of graphene into fluorographene leads to poor electronic quality.⁸⁶ Non-stoichiometric graphene oxide⁸⁴ and monolayers of BCN^{82,85} are also considered in designing 2D van der Waals heterostructures. Similar to the graphene and its derivatives, hexagonal boron nitride (h-BN) or "white graphene" consists of alternating nitrogen and boron atoms in a honeycomb lattice. The sp^2 -bonded 2D atomic plane enables it to be the most studied layered material after graphene.^{81,85}

2D layered materials such as metal dichalcogenides and transition metal oxides have attracted intense research interest as well.⁹⁵ More than 40 different types of metal dichalcogenides present in nature depending on the combination of transition metals and chalcogen.^{88,159} Metal dichalcogenides have a MX_2 stoichiometry. The transition metal atoms have trigonal prismatic or octahedral coordination, and the overall symmetry of MX_2 is rhombohedral. In the layered structures of X-M-X, a metal atomic plane (e.g. W, Mo, Nb, Zr, V, Ni, and Re) separates two hexagonal planes of the chalcogenatoms (e.g. Te, Se, and S). By varying atom coordination and stacking orders, 2D metal dichalcogenide nanomaterials form when adjacent layers bond together weakly.

Some oxides exhibit 2D structural feature at nanoscale as well.^{113,125,160} These include mica, bismuth strontium calcium copper oxide (BSCCO), WO_3 , MoO_3 , V_2O_5 , TiO_2 , perovskite-like crystals, etc. The oxide crystals tend to react with water or hydrogen in air via losing the oxygen. Due to quantum confinement, 2D atomically thin oxide often have larger band-gaps and lower dielectric constants than the bulk counterparts.¹¹³ 2D hydroxides [e.g. $\text{Ni}(\text{OH})_2$, $\text{Eu}(\text{OH})_3$, $\text{Y}(\text{OH})_3$, etc] that can be exfoliated down to trilayer, bilayer, and monolayer sheets are another family of 2D nanomaterials.^{114,160}

Ternary nitrides and carbides are the latest 2D nanostructured materials known as the MAX phases. Chemical composition of the MAX phases is $\text{M}_{n+1}\text{AX}_n$, where $n = 1, 2$, or 3. “X” is N and/or C. “A” is an element from group 13, and Al has been widely used. “M” is a transition metal, e.g. Ti, Nb, V, and Cr. MAX phases are layered hexagonal, in which a unit cell contains two formula units. The element “A” layers interleave with near-close-packed “M” layers. The “X” atoms fill the octahedral sites in between “M” and “A” layers. In the presence of MAX phases, the nitrides and carbides could be exfoliated into layered nanostructures via hydrogen fluoride treatment and sonication.^{140,141} The other common 2D nanomaterials include metal phosphonates or phosphates,¹⁴⁶⁻¹⁴⁸ III–VI semiconductor,¹⁴⁹⁻¹⁵¹ and metal halides.¹⁵²⁻¹⁵⁴

When solid additives are added into a lubricant, fluid drag that acts on the solid surface affects the fluid viscosity and the hydrodynamic pressure.^{161,162} It has been reported that the shape of an additive affects the amount of fluid drag.^{163,164} The additives that align in the fluid direction could reduce the fluid drag. Meanwhile, heat

and mass transfer between two adjacent flow layers also impacts viscosity modification.¹⁶⁵ At the localized contact area, the 2D nano-shaped architecture is capable of changing the mass and heat transfer for the relative motion of the fluid. In such, the viscosity and friction can be modified using the 2D nanomaterials as lubricant additives.

1.4. Summary

This chapter summarized the traditionally used lubricant additives and viscosity modifiers, the classic Einstein viscosity theory, and two-dimensional (2D) nanomaterials.

The challenges in improving machinery efficiency and saving energy consumption have led to the innovation of lubricant additives. Particularly for a fluidic lubrication, viscosity reduction is highly desirable for an energy-saving operation. However, none of the conventional additives is capable of modifying the fluid dynamic behavior. This is due to fact that the conventional additives could increase viscosity following the classic Einstein theory. It is noted that 2D nanomaterials are found to modify rheological properties of solid-stabilized emulsions in an abnormal way. Therefore, the present dissertation research aims at developing a new type of non-Einstein-like lubricant additives.

Following chapters discuss details of this research. Motivations and objectives and the materials and methods are described in the Chapters II and III, respectively. Synthesis and characterization of nanomaterials are delivered in the Chapter IV. The Chapters V and VI cover the tribological examination and the rheological investigations.

Theoretical analyses are conducted at the same time in those chapters. Finally, the Chapter VII presents conclusions and future works.

CHAPTER II

MOTIVATION AND OBJECTIVES

In order to reduce energy consumption during fluidic lubrication, the reduction of viscosity is highly sought after. As discussed in Chapter I, conventional lubricant additives cannot fulfill such needs. Viscosity often increases with additives, following the classic Einstein theory. Therefore, new types of additives that are able to reduce viscosity are desired. It is noted that 2D nanoparticles in solid-stabilized emulsions could affect fluid dynamic behavior in an abnormal way. These 2D nanomaterials are believed to be a promising candidate for the desired viscosity reduction in fluidic lubrication.

Not all 2D nanomaterials listed in Table 1.1 of Chapter I are suitable for modifying the fluid dynamic behavior of lubricants. The reported graphite-based materials and the chalcogenides are effective in boundary lubrication; however the low surface energy of the basal planes after exfoliation limits their applications in fluidic lubrication. The 2D ceramic MAX phases have a high possibility to induce noticeable scratch and wear on the mating surfaces. There are also corrosive elements in the 2D metal halides, which would affect viscosity undesirably and hinder lubrication. In addition, the expensive cost for 2D III–VI semiconductor materials limits their large scale application in the lubricant industry. Hence, the 2D nanomaterials that will be synthesized in this research are chosen from 2D oxide and 2D phosphates. Such materials have relatively strong inter-atomic-layer bonding that makes them resistant to exfoliation. They also have high surface energy, which enables the edges and the

dangling bonds of the basal planes to be passivated by the environment; i.e. lubricant molecules in this study. Considering their their feasibility, yttrium oxide (Y_2O_3) nanosheets, α -zirconium phosphate (ZrP) nanoplatelets, and boron (B)-boron trioxide (B_2O_3) composited nanoparticles will be synthesized and characterized for the tribological and rheological investigations in this research.

The approaches and the major objectives of this research are addressed in the following flow chart.

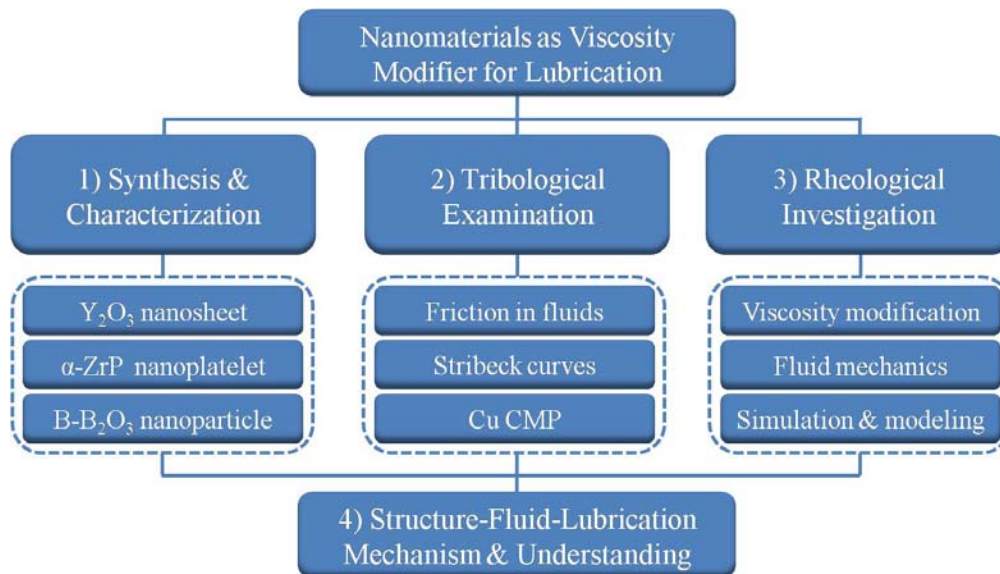


Figure 2.1. Research flow chart.

1) Synthesizing and characterizing the nanomaterials

As discussed above, three 2D nanomaterials are used in this research: Y_2O_3 nanosheets, α -ZrP nanoplatelets, and B- B_2O_3 composited nanoparticles. Hydrothermal synthesis is a facile but powerful method to prepare a broad range of nanomaterials. It

was used to synthesize the α -ZrP nanoplatelets, and is adopted in the one-pot preparation of the Y_2O_3 nanosheets. The B-B₂O₃ nanoparticles are synthesized using a home-built chemical vapor deposition system. The size of the nanoparticles is regulated by controlling the deposition rate. Unique properties based on the 2D morphology or structures are characterized prior to the tribological and rheological investigation.

2) Improving tribological performance using 2D nanomaterials

In a viscous lubricant, friction varies as a function of load for different speeds. The variation is represented by the Stribeck curves. The Stribeck curves for both aqueous and non-aqueous lubricants are being studied with and without the nano-additives. In such, the tribological performance of different nano-additives is examined. Improvement in lubricating performance is highly anticipated based on the 2D nanomaterials proposed here. The tribological examination would finally provide a general guidance for designing and developing a new generation of fluidic lubricants. As an example, chemical-mechanical planarization of copper are carried out to prove the improved tribological performance.

3) Exploring non-Einstein-like viscosity additives

For a fluidic lubricant to be effective, viscosity should be reduced. However, inorganic particulates would increase viscosity, following the classic Einstein theory. Therefore, reduction of viscosity using the conventional lubricant additives is challenging. It is of great interest to modify the lubricant's fluid dynamic behavior by

exploring novel nanomaterials-based additives. A rheological investigation of lubricants possessing non-Einstein-like behavior is conducted. Such lubricants are designed to work efficiently with the addition of the 2D sheet-like nanoparticles.

4) Establishing a relationship between structure and fluid-lubricants

The ultimate goal of this research is to obtain an understanding and to establish structure-fluid -lubrication relationships for the 2D nano-additives. Fluid mechanics calculations, viscous flow analysis, and computational simulation are carried out to achieve this goal. For the lubricant flow with different nano-additives, flow-rate distribution, and viscosity could be calculated using the Navier-Stokes equation and the Reynolds equation, respectively. The reasons for the viscosity-induced lubrication improvement can be addressed from this analysis. A particle hydrodynamic simulation is used to confirm the experimental results and the fluid mechanics calculations. The fundamental rheological and tribological investigations will enable a better understanding of the nano-fluidic behaviors. The nano-fluidic mechanism will be finally developed.

CHAPTER III

MATERIALS AND METHODS

This chapter describes methods and procedures utilized in the current research. It has five sections. The first two sections describe chemicals and synthesis of nanomaterials, including yttrium oxide (Y_2O_3) nanosheets (NS), α -zirconium phosphate (ZrP) nanoplatelets, and boron (B)-boron trioxide (B_2O_3) composited nanoparticles. The third section contains technique details of characterization. Specifics of tribological and rheological experiments (including chemical-mechanical planarization) are discussed in the fourth and fifth sections.

3.1. Materials

The following chemicals were purchased from Sigma-Aldrich, USA: Y_2O_3 nanopowder, zirconyl chloride octahydrate ($ZrOCl_2 \cdot 8H_2O$), boron tribromide (BBr_3), concentrated sulfuric acid (H_2SO_4 , ACS reagent), nitric acid (HNO_3 , ACS reagent), phosphoric acid (H_3PO_4 , ACS reagent), ammonium hydroxide solution (NH_4OH , 28.0-30.0 % NH_3 basis), potassium hydroxide (KOH), citric acid, benzotriazole (BTA), and hydrogen peroxide (H_2O_2), heavy mineral oil, aluminum nitrate nonahydrate [$Al(NO_3)_3 \cdot 9H_2O$], magnesium nitrate hexahydrate [$Mg(NO_3)_2 \cdot 6H_2O$], manganese nitrate tetrahydrate [$Mn(NO_3)_2 \cdot 4H_2O$], iron nitrate nonahydrate [$Fe(NO_3)_3 \cdot 9H_2O$], nickel nitrate hexahydrate [$Ni(NO_3)_2 \cdot 6H_2O$], copper nitrate trihydrate [$Cu(NO_3)_2 \cdot 3H_2O$], zinc nitrate hexahydrate [$Zn(NO_3)_2 \cdot 6H_2O$], palladium nitrate dehydrate [$Pd(NO_3)_2 \cdot 2H_2O$], silver

nitrate (AgNO_3), indium nitrate hydrate [$\text{In}(\text{NO}_3)_3 \cdot x\text{H}_2\text{O}$], holmium nitrate pentahydrate [$\text{Ho}(\text{NO}_3)_3 \cdot 5\text{H}_2\text{O}$], dysprosium nitrate pentahydrate [$\text{Dy}(\text{NO}_3)_3 \cdot 5\text{H}_2\text{O}$], and gadolinium nitrate hexahydrate [$\text{Gd}(\text{NO}_3)_3 \cdot 6\text{H}_2\text{O}$]. All chemicals were used without further purification. Glass slides and E52100 alloy steel ball (Ø 6.35 mm) as the sliding counterparts were purchased from VWR International and McMaster-Carr, respectively. Compressed gases of argon (Ar) and hydrogen (H_2) were purchased from Praxair Distribution, Inc. A commercial SiO_2 slurry was purchased from Fujimi Corporation for CMP experiment, and the SiO_2 nanoparticles ($\text{Ø} \sim 35$ nm) were purchased from Cabot Electronics co. Boron (B)-doped-silicon (Si) wafer (doping concentration between 10^{13} and 10^{16} atoms per cm^3) and Cu film (~ 2 μm in thickness) coated Si wafers were purchased from Siltronic AG.

3.2. Synthesis of nanomaterials

3.2.1. Y_2O_3 nanosheets

In the present study, multi- and single-phase Y_2O_3 nanosheets (NS) were synthesized via a hydrothermal method.¹²⁴ In a typical synthesis, 0.4 g commercial Y_2O_3 powder was first dissolved in 80 mL HNO_3 solution (3.4 wt %) at 50 °C to form a clear and transparent yttrium nitrate [$\text{Y}(\text{NO}_3)_3$] solution. After adding 320 mL deionized (DI) water, a KOH solution (15wt %) was used to adjust the pH value of the mixed solution to 8.7 rapidly. White $\text{Y}(\text{OH})_3$ floc appeared as soon as the KOH was added to the $\text{Y}(\text{NO}_3)_3$ solution. This turbid solution was filled with DI water up to 600 mL and transferred into a 2 L general purpose non-stirred pressure vessel (4622Q, Parr

Instrument) after stirring for 10 min. Schematic diagram of the pressure vessel is shown in Figure 3.1. The vessel was sealed and heated at different temperature, ranging from 80 °C to 240 °C, for 12 hours. Multiphase irregular Y_2O_3 nanostructure, multiphase Y_2O_3 NS, and multiphase Y_2O_3 nanowire (NW) were synthesized at 80 °C, 120 °C, and 240 °C, respectively. They were collected after the cooling the vessel to room temperature. Possible unwanted ionic remnants were removed by rinsing with great amount of DI water. Final products were dried in air at 70 °C for 24 hours after filtration. In order to investigate the metal ion-assisted transformation of multiphase Y_2O_3 NS to single-phase cubic Y_2O_3 NS, different metal ions from their nitrates were used in the synthesis. They were magnesium (Mg), aluminum (Al), manganese (Mn), iron (Fe), nickel (Ni), copper (Cu), zinc (Zn), palladium (Pd), silver (Ag), indium (In), gadolinium (Gd), dysprosium (Dy), and holmium (Ho). A molar ratio of 80 to 1 was selected for the yttrium ion to the metal ion with the subsequent processes being the same as that for the multiphase Y_2O_3 NS.

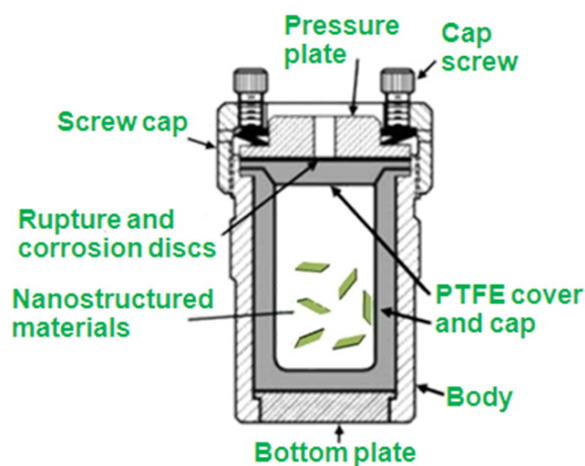


Figure 3.1. Schematic diagram of the Teflon[®]-lined pressure vessel.

3.2.2. α -ZrP nanoplatelets

Similarly, two dimensional α -ZrP nanoplatelets used in this research were synthesized using the hydrothermal method as well.^{166,167} In a brief, 10 mL of ZrOCl_2 aqueous solution (13.5 mmol of $\text{ZrOCl}_2 \cdot 8\text{H}_2\text{O}$) was added drop wise to a 30 mL solution of H_3PO_4 (12M) into a 80 ml Teflon[®]-lined pressure vessel under constant stirring (final $[\text{H}_3\text{PO}_4] = 9\text{M}$). Then the pressure vessel was sealed and heated at 200 °C for 24 hours. The product was washed several times with DI water and dried at 70 °C. The resulting powder was grounded with a mortar and pestle into fine particles.

3.2.3. B-B₂O₃ composited nanoparticles

In the present study, a chemical vapor deposition (CVD) method was developed to synthesize α -rhombohedral boron nanoparticles with different sizes. As schematically shown in Figure 3.2, Ar was used as carrier and protective gas, and H_2 was used as a reductant for BBr_3 . Flow speeds were regulated by a mass-flow controller (1179A, MKS Instruments). Before these gases passed the flask containing 2ml of BBr_3 , they were thoroughly dried with concentrated H_2SO_4 and molecular sieves. The B-doped-Si substrate was loaded in a ceramic boat and placed in the tube furnace (TF55030A-1, Lindberg-Blue M Thermo Scientific) before synthesis started. Initially, the quartz tubular chamber was purged with pure Ar flow (250 sccm) for 1.5 hours. During purging, BBr_3 was kept at ~ -70 °C by dry ice and no BBr_3 molecules volatilized at this temperature. The temperature of the quartz chamber was increased during the same time period. Once the quartz chamber reached 900 °C, BBr_3 was heated to the volatilizing

temperatures above its flash point ($-18\text{ }^{\circ}\text{C}$), and a mixed gas flow of 120 sccm Ar and 40 sccm H_2 was introduced into the chamber. In order to control the growth of boron nanoparticles, three different volatilizing temperatures were selected for BBr_3 , $0\text{ }^{\circ}\text{C}$, $10\text{ }^{\circ}\text{C}$, and $20\text{ }^{\circ}\text{C}$. The reaction was then maintained until all BBr_3 was gone. The byproduct, hydrogen bromide (HBr), is hazardous so that the waste gas was purged into the concentrated H_2SO_4 and reacted with NH_4OH in order to get ammonium bromide (NH_4Br), which is a safe agent. After reaction, the ceramic boat was removed when the chamber was cooled to the room temperature. Next, the surface of boron nanoparticles was oxidized to boron trioxide (B_2O_3) by exposing them to air at $900\text{ }^{\circ}\text{C}$ for 45 minutes. These B- B_2O_3 composited nanoparticles were then collected for characterization and CMP experiment.

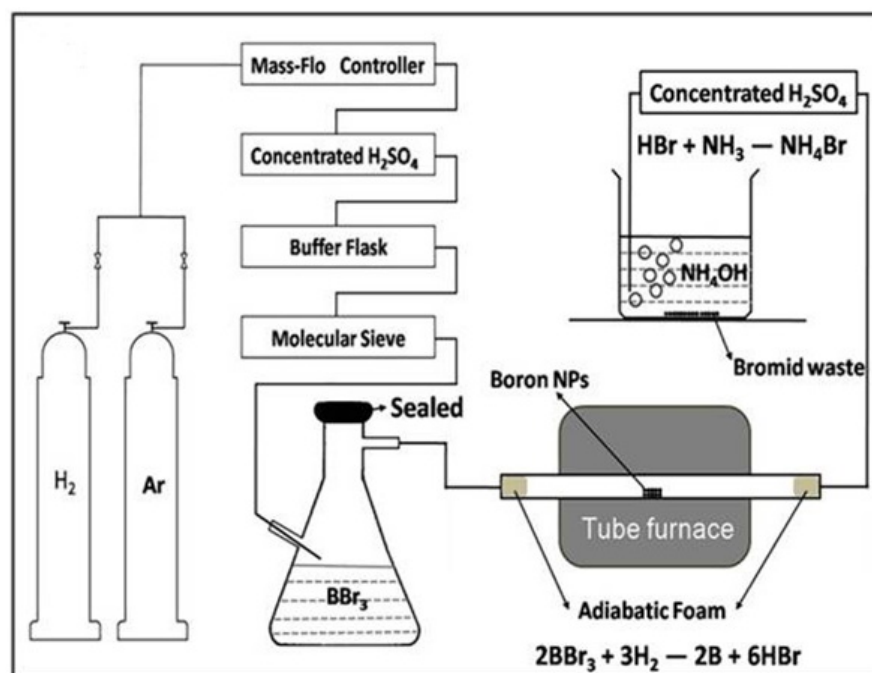


Figure 3.2. Scheme of the home-built CVD system for synthesis of B- B_2O_3 composited nanoparticles.

3.3. Characterization

A D8 advance X-ray diffractometer (XRD, Bruker) was used to determine crystal structure of the nanomaterials. Cu $K\alpha$ radiation ($\lambda = 1.5418 \text{ \AA}$), operating at 50 mA and 40 kV, was the X-ray source. A transmission electron microscope (TEM, JEOL 1200) was used to examine the size and morphology of the products using accelerating voltage at 100 kV. A field emission scanning electron microscope (FESEM, FEI Quanta 600) was used to image the morphology features of the 2D sheet-like nanomaterials as well. The selected area electron diffraction (SAED) analysis was performed with the instrument connected with a high-resolution (HR) TEM (JEOL 2010, accelerating voltage at 200 kV). The samples for TEM and SAED studies were prepared by slow evaporation of a drop of diluted water solution of the nanomaterials on the carbon coated Cu grid at room temperature. An atomic force microscope (AFM, Nano-R2, Pacific Nanotechnology) was utilized in this study for the surface measurements. Raman spectra were recorded using micro-Raman spectrometer (Raman, Jobin Yvon iHR-320) with a light source of He-Ne green laser (532 nm in wavelength). A Fourier transform infrared (FTIR) spectrometer (Thermo Scientific Nicolet 380) was used to record the infrared spectra at resolution of 4 cm^{-1} by averaging 250 scans. The powder of nanomaterials was measured using the attenuated total reflection (ATR) technique. A small amount of the liquid samples was measured after putting it between two blocks of KBr.

Particularly, current-voltage (I-V) characteristics of different Y_2O_3 samples were measured based on a metal-semiconductor (M-S) junction. Samples of M-S junction were prepared by dropping 10 μL different Y_2O_3 (0.0001 wt %) solution on Cu

substrates. All those samples were fully dried at 80 °C. After drying, the Y_2O_3 particles were deposited on the Cu substrate. The I-V characteristic analysis of the M-S junctions was conducted using a Keithley 2400 Digital SourceMeter together with a probe system. A tungsten probe was placed contacting with the top surface of Y_2O_3 . During the electric measurement, the Cu substrate and the tungsten probe were used as the bottom electrode and the top electrode, respectively. The I-V measurement was conducted under a scanning voltage ranged between -3.0 V and 3.0 V in 1000 steps.

3.4. Tribological and rheological experiments

During the tribological and rheological experiments, lubricant samples consisted of a base liquid (mineral oil or DI water) and the additives (Y_2O_3 NS or α -ZrP nanoplatelets). The additives with different concentrations (1 wt %, 0.5 wt %, and 0.1 wt %) were simply dispersed in the base liquid via ultrasonication for 15 minutes before the measurements. The coefficients of friction were recorded using a tribometer (CSM Instruments). As shown in Figure 3.3, the tribological measurements were carried out via a pin-on-disk configuration consisting of a rotating disk (glass slide) and a fixed pin (steel ball). 100 μ l of liquid (mineral oil or DI water with or without the additives) was added on the disk, and the radius of the wear track was set at 3 mm. The reason to set this parameter is to avoid spill of the liquid during high speed rotating. The rotating speeds were from 10 rpm to 600 rpm under different load, 1N, 0.5 N, 0.25 N, and 0.15 N. Coefficient of friction at specific speed and loaded was recorded. The duration of each test was 1 minute. To plot the Stribeck curve, the averaged friction coefficients

were obtained from original data and the standard deviation was used to calculate corresponding error. The viscosity was measured using an AR-G2 rheometer (TA Instruments, setup is schematically shown in Figure 3.4) with the shear rate ranged from 10 s^{-1} to 18740 s^{-1} . During experiments, a stainless steel parallel spindle ($\text{Ø} 25 \text{ mm}$) rotated while the lower Peltier plate was stationary. A test liquid filled the gap of $200 \text{ }\mu\text{m}$ between parallel plates. The temperature was maintained at $25 \text{ }^\circ\text{C}$. Thixotropic behavior was investigated by applying a constant shear rate (10000 s^{-1}) to the lubricants for 10 minutes while tracking the changes of the viscosity in time.

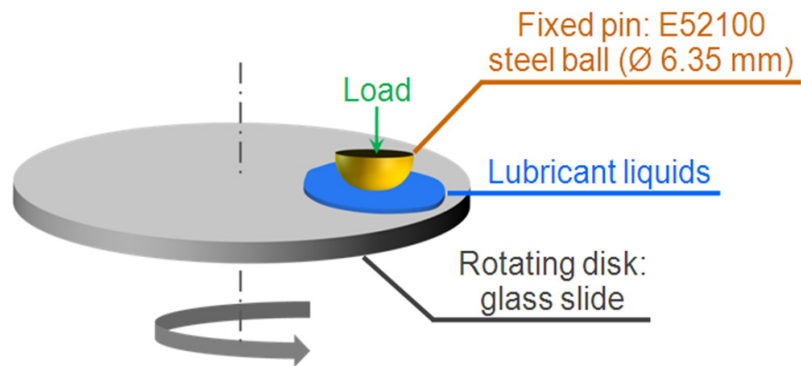


Figure 3.3. Diagram of the pin-on-disk testing configuration.

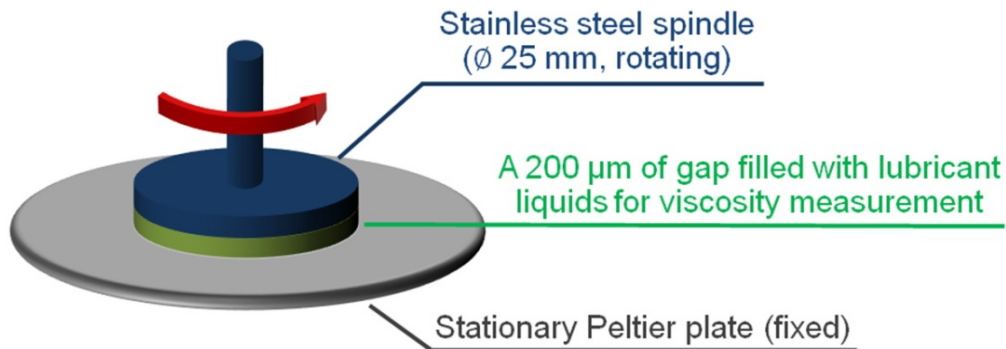


Figure 3.4. Schematic setup of AR-G2 rheometer.

3.5. CMP experiments using different nano-abrasives

In the microelectronic manufacturing, CMP process is an important tribological-based process. A CMP experimental setup is briefly illustrated in Figure 3.5. A rotating polishing pad is in contact with a target wafer that is adhered to a rotating head. The material on the wafer is removed via wear and abrasion between the rotating pad and head. In order to obtain a well planarized surface and enhance material removal, a polishing slurry containing different nano-abrasives is continuously supplied through the nozzle. As polishing proceeds, efficiency of planarization and materials removal would reduce due to deterioration of pad asperity. An ex-situ or in-situ conditioner is needed to maintain the asperity.

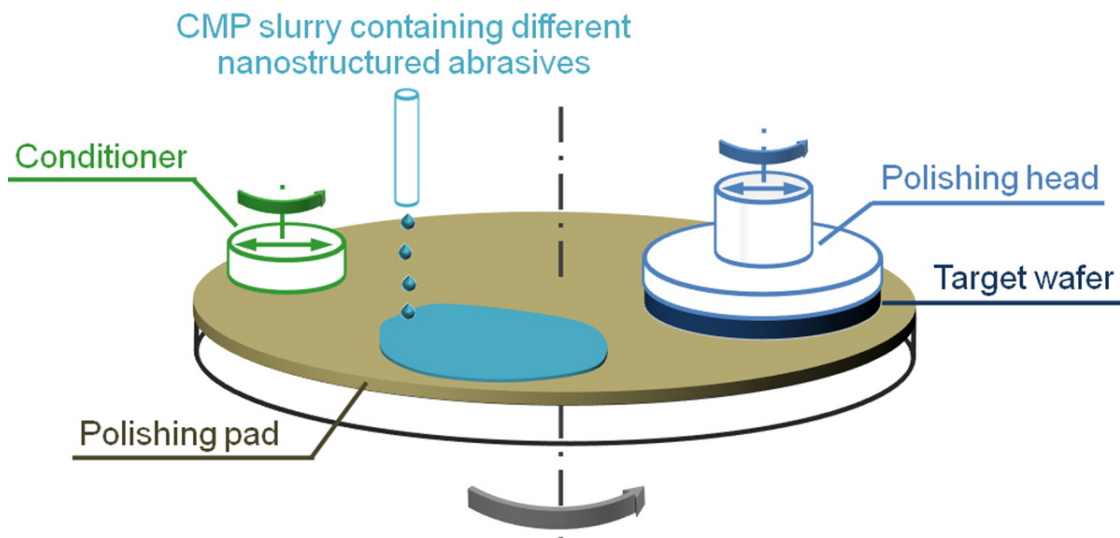


Figure 3.5. Illustration of CMP experimental setup schematically.

3.5.1. B-B₂O₃ nanoparticles as abrasives

The Cu film (~ 2 μm in thickness) coated Si wafers were used as target substrates for CMP experiments using B-B₂O₃ composited as abrasive in the slurry. Before CMP, they were cut into 2 cm × 2 cm, and five pyramidal micro-indentations were made with a depth of 1 μm using a micro-hardness tester (HM2000, Fischer Technology, Inc.) on each of them. The line of micro-indentations was parallel to the edge of the squared Cu-Si wafer and 5 mm away from it. The distance between each micro-indentation was 0.5 mm. These Cu films were then CMPed with a Politex polishing pad (Rohm & Haas) that was made of polyester and polyurethane. The polishing slurry was composed of citric acid (0.01 M), BTA (0.05 wt %), H₂O₂ (3 vol %), abrasive particles (3 wt %), and DI water. Three different abrasive particles were used: 1). pure SiO₂ nanoparticles (Ø ~ 35 nm, Cabot Electronics co.) abrasive; 2). pure B-B₂O₃ composited nanoparticles (sized ~ 5 nm) abrasive; and 3). the SiO₂ nanoparticles-based abrasive containing the 1 wt % B-B₂O₃ composited nanoparticles. Using 1 M of KOH, the slurry pH values were adjusted to 5, at which H₃BO₃ can be dissolved into water with very high concentration.¹⁶⁸ Each polishing experiment was conducted for 210 seconds using a tribometer (CSM Instruments). The Cu films were placed face-down onto the polishing pad. The applied load was 2 N (5 KPa), and the rotation speed was maintained at 40 rpm (0.21 cm·s⁻¹). The AFM (Nano-R2, Pacific Nanotechnology) was used to analyze the samples before and after CMP experiments.

3.5.2. Y_2O_3 nanosheets as abrasives

In the CMP experiment using Y_2O_3 NS abrasive, a home-made slurry was used, which was composed of citric acid (0.01 M), BTA (0.05 wt %), H_2O_2 (3 vol %), Y_2O_3 NS abrasive (3 wt %), and DI water. A commercial SiO_2 slurry ($\sim \text{Ø}$ 35 nm, Fujimi Corporation) was used as-received for comparison in this CMP experiment. Cu film ($\sim 2 \mu\text{m}$ thick) coated Si wafers (Ø 300 mm) were used as target substrates here. These wafers were then CMPed with an IKONICTM polishing pad (Rohm & Haas). All polishing experiments were conducted using a Universal CMP Tester (Figure 3.6) with the same set-up configuration showing in Figure 3.5. Polishing was conducted for 1 minute. Wafers were placed face-down onto the polishing pad. The applied pressure was 1 psi (6894.757 Pa), and rotation speeds of the pad and the wafer were maintained at 79 rpm and 76 rpm, respectively. The speeds were kept close to each other for good uniformity in wafer planarization. Each slurry was used to polish four wafers. The averaged thickness of the Cu film was measured using a table top four point probe (CDE ResMap 273) choosing 80 spots along the diameter of each wafer. The percentage ratio of the standard deviation of thickness relative to the averaged value was used to calculate the within-wafer-non-uniformity (WIWNU).¹⁶⁹⁻¹⁷¹ A surface profile topography system (KLA-Tencor HRP-350) was used to measure the surface roughness and the Cu dishing on Si wafers. Results of the WIWNU, the surface roughness, and the Cu dishing were presented statistically.

In addition, frictional behaviors and rheological properties of the slurries used in this section were examined separately. In order to solely investigate the frictional

behaviors and rheological properties of SiO₂ nanoparticles and Y₂O₃ NS, the measurements were conducted in DI water. Friction experiments of Cu wafers were carried out using a tribometer (CSM Instruments). IC 1000 polishing pads (Rohm & Haas) with SiO₂ (3 wt %) and Y₂O₃ (3 wt %) slurries were used in friction experiments. Friction coefficients were recorded during each test for 60 cycles (20 mm per cycle, 20 mm/s) with an applied pressure of 80 kPa. An AR-G2 rheometer (TA Instruments) was used to measure the change of shear stress with shear rate ranging from 30 s⁻¹ to 500 s⁻¹. In rheological experiments, three different concentrations were selected for slurries, 0.3 wt %, 3 wt %, and 10 wt % in DI water. During the measurement, a stainless steel parallel spindle (Ø 25 mm) rotated while the lower Peltier plate was stationary. The gap (500 µm) between parallel plates was filled with slurries, and the temperature was maintained at 25 °C.



Figure 3.6. Pictures of the Universal CMP Tester.

CHAPTER IV

SYNTHESIS AND CHARACTERIZATION*

This chapter discusses the synthesis, characterization, and properties of nanomaterials investigated. It has three sections. The first section contains hydrothermal synthesis of yttrium oxide (Y_2O_3) nanosheets. The second is about α -zirconium phosphate (ZrP) nanoplatelets synthesized using the similar hydrothermal method. At last, a home-built chemical vapor deposition system is developed for synthesis of boron-boron trioxide (B_2O_3) composited nanoparticles.

4.1. Yttrium oxide nanosheets

4.1.1. Synthesis of multiphase Y_2O_3 nanosheets (NS)

Rare-earth elements are a large family of functional materials that have broad applications in magnetics, electronics, optics, mechanics, and catalysis.¹⁷²⁻¹⁷⁵ Aqueous synthesis of colloidal nano-rare-earth-materials has been widely used during the preparation.^{135,176,177} In a hydrothermal method, the anisotropic growth of rare-earth hydroxides or oxide composites was conventionally obtained via modifying OH⁻ ligands.¹⁷⁷⁻¹⁷⁹ Simultaneous precipitations from boiling water solution results in complex

*Part of this chapter reproduced with permission from “Cuⁿ⁺-assisted synthesis of multi- and single-phase yttrium oxide nanosheets” by Xingliang He, et al., *J. Mater. Chem. C*, **2013**, *1*, 6829-6834 (Copyright © 2013, Royal Society of Chemistry); “Boron-based nanoparticles for chemical-mechanical polishing of copper films” by Xingliang He, et al., *ECS J. Solid State Sci. Technol.*, **2013**, *2*, P20-P25 (Copyright © 2013, The Electrochemical Society); and “ α -zirconium phosphate nanoplatelets as lubricant additives” by Xingliang He, et al., *Colloids Surf., A*, **2014**, *452*, 32-38 (Copyright © 2014, Elsevier).

compounds with multiphase.¹⁸⁰⁻¹⁸² In addition, the hydroxide nanomaterials demand high-temperature dehydration ($> 500\text{ }^{\circ}\text{C}$) to transform them into oxide.^{135,183,184} The transformation of phase, microstructure, and morphology occur along with the heat treatment. Y_2O_3 has three distinct crystalline phases in nature: cubic, hexagonal, and monoclinic. The cubic structure is the most stable phase and has been extensively studied as phosphors,¹⁸⁵ microwave filters,¹⁸⁶ and solid-state laser.¹⁸⁷ Single-phase cubic Y_2O_3 provides rapid electron transfer with high efficiency as compared with their multiphase compounds.^{188,189} Therefore, a one-pot synthesis of single-phase cubic Y_2O_3 nanomaterials, featuring easy control, simple apparatus, and low temperature, is highly desirable.

The hydrothermal method has shown to be effective in synthesis of oxide nanomaterials. It is observed in Figure 4.1 that different Y_2O_3 nanostructures were synthesized via hydrothermal reactions at different temperature. At low temperature ($80\text{ }^{\circ}\text{C}$), irregular Y_2O_3 nanostructures were obtained as shown in Figure 4.1a. Square Y_2O_3 NS ($317 \pm 49\text{ nm}$ side, Figure 4.1b) and Y_2O_3 nanowires (NW, Figure 4.1c) were synthesized at $120\text{ }^{\circ}\text{C}$ and $240\text{ }^{\circ}\text{C}$, respectively. An AFM image of Y_2O_3 NS is shown in Figure 4.1d. The average thickness of Y_2O_3 NS is $16 \pm 1\text{ nm}$. This gives the aspect ratio as high as 25. A commercial multiphase Y_2O_3 powder was used as starting material for synthesis of these Y_2O_3 NS. In Figure 4.1e, the XRD pattern of the commercial Y_2O_3 powder is shown with the black (bottom) plot. Three different phases were revealed: cubic (phase c in Figure 4.1e, JCPDS Files No. 41-1105), hexagonal (phase h in Figure 4.1e, JCPDS Files No. 20-1412), and monoclinic (phase m in Figure 4.1e, JCPDS Files

No. 44-0399). All three phases are observed in the XRD pattern of the as-synthesized irregular Y_2O_3 nanostructure, Y_2O_3 NS and Y_2O_3 NW (see top colored plots in Figure 4.1e). Directly hydrothermal-synthesized Y_2O_3 nanomaterials, including NS, are multiphase. The reaction between water and Y_2O_3 powder occurs spontaneously via hydrolysis in nitrate solution.¹⁹⁰ This reaction leads to the formation of hydroxide and oxide-hydroxide. Presences of the hexagonal hydroxide and monoclinic oxide-hydroxide species can be confirmed by the other unidentified peaks in the XRD patterns in Figure 4.1e.

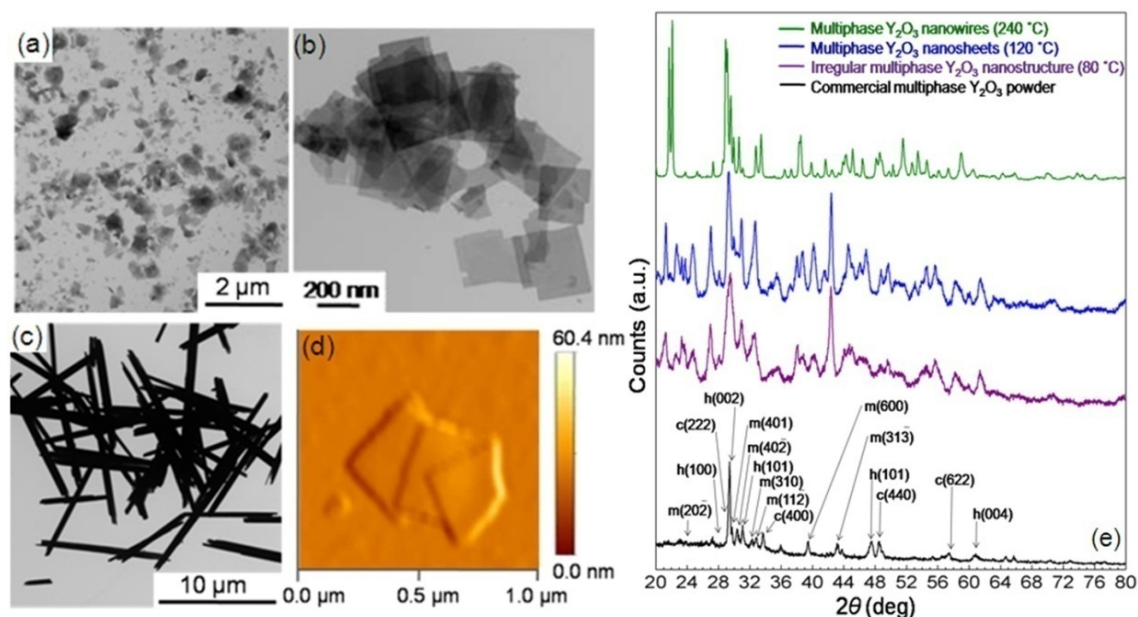


Figure 4.1. TEM images of irregular Y_2O_3 nanostructure (a), Y_2O_3 NS (b) and Y_2O_3 NW (c) synthesized at 80 °C, 120 °C, and 240 °C, respectively. (d) AFM images of the Y_2O_3 NS. (e) Comparison of XRD patterns among the commercial multiphase Y_2O_3 powder (bottom black pattern), the irregular nanostructure, NS, and NW of multiphase Y_2O_3 (top colored patterns).

Most metal hydroxide and oxide-hydroxide have layered structures.¹⁹¹⁻¹⁹⁴

Exfoliation of the layered structures results in the formation of hydroxide or oxide-hydroxide NS initially. Y_2O_3 NS is obtained hydrothermally via subsequent dehydration of the hydroxide and oxide-hydroxide in the high-boiling solution.^{195,196} Due to the random distribution of two-dimensional growth orientations, multiphase Y_2O_3 NS will be obtained with cubic, hexagonal, and monoclinic crystalline structures. At high temperature (240 °C), Y_2O_3 dissolves into the solution gradually, leading to nucleation of yttrium hydroxide again.¹⁹⁷ The nuclei evolve into one-dimensional multiphase crystals at nanoscale due to the high anisotropic structure along c-axis in hexagonal yttrium hydroxide. Surface energy reduces substantially due to elimination of the rigid lamellar structured interface.¹⁹⁸ This prompts the thermodynamic driving force to fuse and align nanocrystals together anisotropically.¹⁹⁹ One-dimensional hydroxide NW forms spontaneously.

4.1.2. Phase transformation

An interesting phenomenon that we observed during the synthesis was the transformation of Y_2O_3 NS from the multiphase structure to the single-phase one. As shown with the red (top) XRD pattern in Figure 4.2a, only the cubic phase (JCPDS Files No. 41-1105) is obtained from Y_2O_3 NS that was synthesized in the presence of Cu ions (Y_2O_3 -Cu NS, see Figure 4.2b). Different from multiphase Y_2O_3 NS as discussed above, the Y_2O_3 -Cu NS is single cubic phase. The effects of other metal ions were also investigated in the synthesis of Y_2O_3 NS. Their XRD patterns are shown in Figure 4.3a,

from which we observe multiphase Y_2O_3 only. According to TEM images in Figures 4.1b, 4.2b, and 4.3b, we can see that the two-dimensional morphology of Y_2O_3 NS is well maintained, even though different metal ions were involved during the synthesis. Crystalline phase of the single-phase cubic Y_2O_3 -Cu NS and multiphase Y_2O_3 NS are further compared using SAED patterns in Figures 4.4a and 4.4b. These two patterns were recorded from the same samples that are shown in Figures 4.1b and 4.2b, respectively. In the single-phase cubic Y_2O_3 -Cu NS (Figure 4.4a), only electron diffraction patterns indexed in the red (top) XRD pattern of Figure 4.2a are observed. They are cubic (222), cubic (400), cubic (440), and cubic (622). In contrast, as shown in the SAED pattern of Figure 4.4b, both hexagonal and monoclinic crystalline phases present in addition to the cubic phase. Therefore, it is concluded that Cu ions, as a phase transfer catalyst, play a unique role in assisting the formation of single-phase cubic Y_2O_3 NS. On the basis of our present results, it is difficult to address the reasons why multi-single-phase transformation occurs and how Cu ions catalyze the transformation. Further investigations are being carried out to reveal the mechanism that Cu ions transform the multiphase Y_2O_3 NS into the single-phase cubic Y_2O_3 NS.

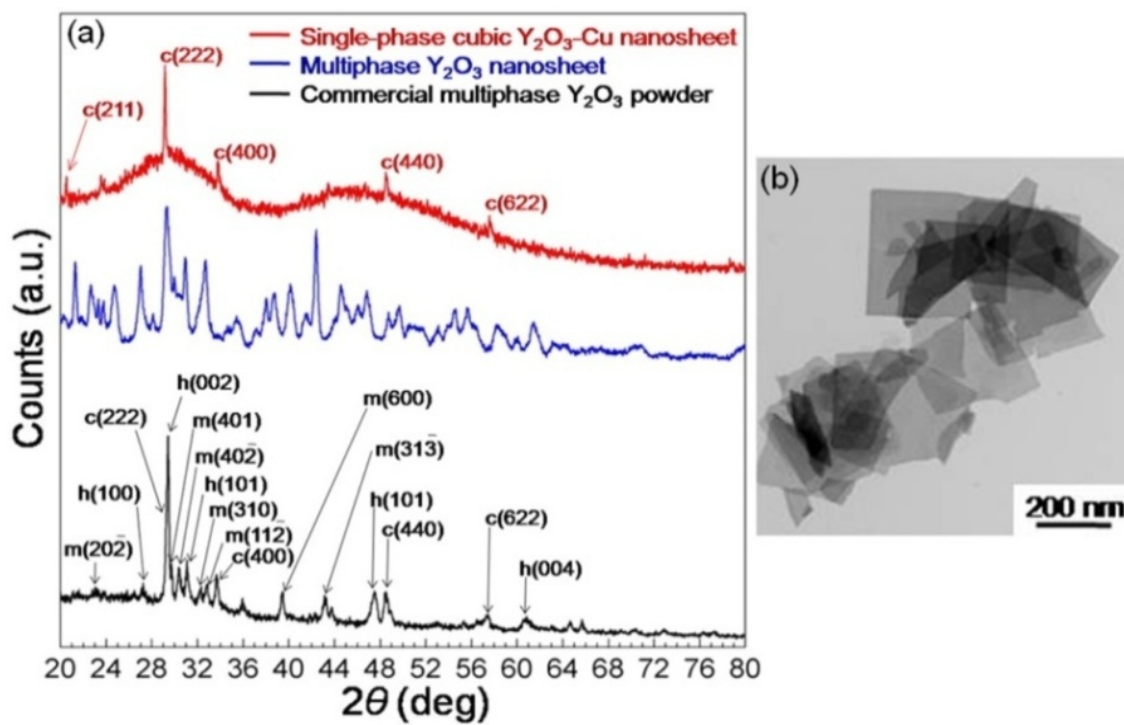


Figure 4.2. (a) Comparison of XRD patterns among the commercial multiphase Y_2O_3 powder (bottom black pattern), the multiphase Y_2O_3 NS (middle blue pattern), and the single-phase cubic Y_2O_3 -Cu NS (top red pattern); (b) TEM image of the single-phase cubic Y_2O_3 -Cu NS.

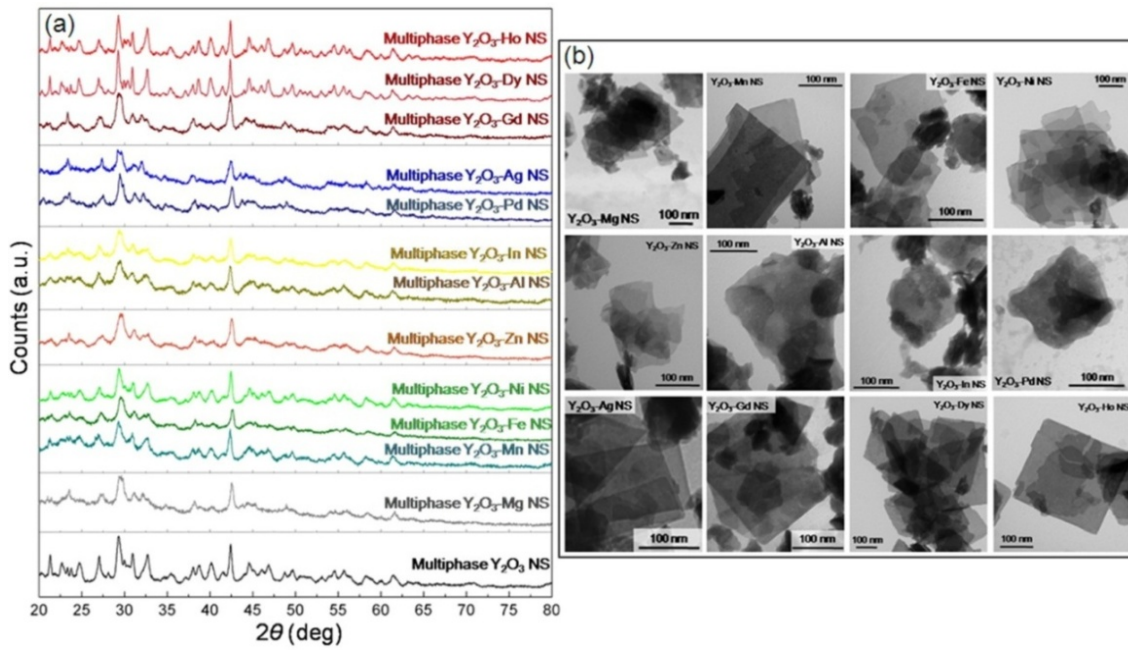


Figure 4.3. (a) XRD patterns of multiphase Y_2O_3 NS synthesized in the presence of the other metal ions. (b) TEM images of multiphase Y_2O_3 NS synthesized in the presence of the other metal ions.

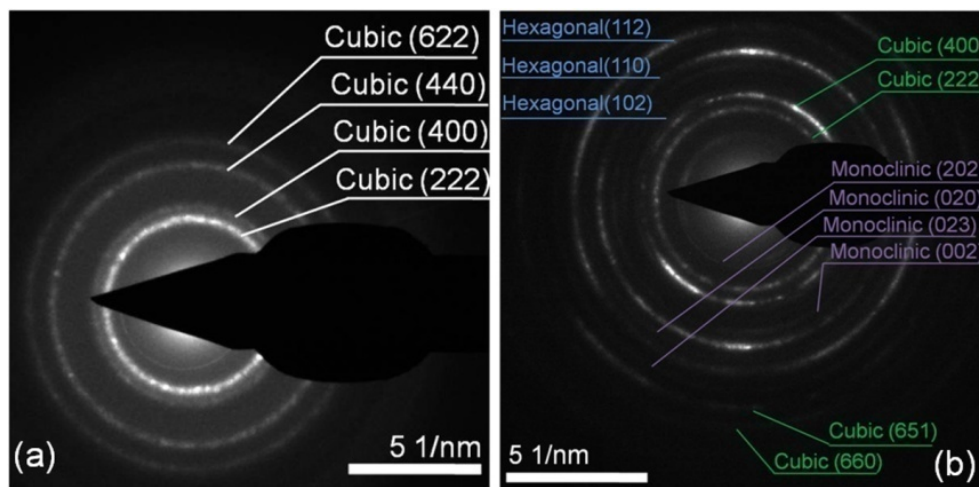


Figure 4.4. SAED patterns of the single-phase cubic Y_2O_3 -Cu NS (a) and the multiphase Y_2O_3 NS (b).

4.1.3. I-V characteristics

Based on an M (Cu)-S (Y_2O_3) junction, we investigate the electronic transportation behaviors of the multiphase Y_2O_3 NS and the single-phase cubic Y_2O_3 -Cu NS. A tungsten probe was placed contacting with the top surface of Y_2O_3 mechanically (See Figure 4.5a). The results of I-V characteristics are shown in Figures 4.5b through 4.5e. Cu is used as bottom electrode, and the current passing through it is directly proportional to the applied voltage (Figure 4.5b). The I-V characteristic of the commercial multiphase Y_2O_3 is shown in Figure 4.5c as a reference. The Schottky diode-like behavior is observed with an obvious leakage current and a great current fluctuation. The commercial Y_2O_3 powder has a random distribution in its size, morphology, and structure. Therefore, it is impossible to exhibit efficient electronic transportation through the interface between each Y_2O_3 particle. An inhomogeneous electric field is believed to build in the commercial multiphase Y_2O_3 and results in the current fluctuation. The large leakage current can be attributed to the easy draw of defects-induced electrons and holes from the depletion layer.^{200,201} The output current versus voltage in Figure 4.5d exhibits significant nonlinearity in multiphase Y_2O_3 NS-based M-S junction. Schottky diode-like behavior is obtained with a negligible leakage current. When a positive bias is applied to the Cu bottom electrode, its Fermi energy is lowered with respect to that of Y_2O_3 . More electrons will diffuse towards the Cu than the number drifting into the Y_2O_3 NS due to the smaller potential drop across the Y_2O_3 NS. Multiphase Y_2O_3 NS has a thin and uniform nanostructure, across which the potential drops fast and smoothly. A distinct forward current, passing through the junction, is

obtained in the right branch ($V > 0$) of Figure 4.5d as the voltage becomes larger than the built-in potential barrier. Before the positive bias surpasses the built-in potential barrier, electrons accumulate at the M-S interface with the increase of voltage. Two-dimensional morphology of multiphase Y_2O_3 NS enables it to accumulate more electrons till a higher voltage is reached. The multiphase Y_2O_3 NS-based M-S junction thus has a larger built-in potential barrier than that based on the commercial multiphase Y_2O_3 (Figure 4.5c). When a negative voltage is applied to the Cu bottom electrode, its Fermi energy is raised comparing to that of Y_2O_3 . The potential across the Y_2O_3 increases, yielding a large depletion region. This barrier restricts the electronic transportation to the Cu bottom electrode. A negligible leakage current is observed from the left branch ($V < 0$) of Figure 4.5d due to the uniform two-dimensional structure of thin multiphase Y_2O_3 NS. Further increase of negative bias leads to a breakdown of the M-S junction. During the breakdown, the broken ionic/covalent bonding enables electron tunnelling from the valence band to the conduction band like a Zener diode.^{202,203} Similar to the distinct forward current, this clear reverse current gives rise to the high slope resistance due to the uniform and fast electronic transportation.

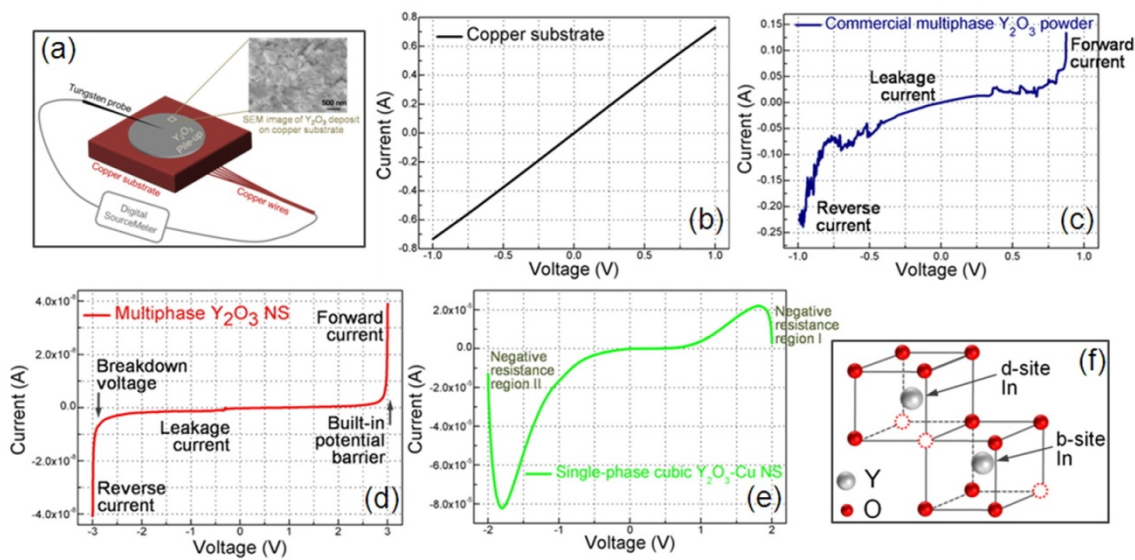


Figure 4.5. (a) Schematic of the I-V setup. I-V characteristics of the Cu substrate electrode (b), the commercial multiphase Y_2O_3 powder (c), the multiphase Y_2O_3 NS (d), and the single-phase cubic Y_2O_3 -Cu NS (e). (f) Structure of cubic Y_2O_3 .

A novel negative resistance is observed on the single-phase cubic Y_2O_3 -Cu NS, in which an increase in voltage results in decreased current. As it is shown in Figure 4.5e, two asymmetric negative resistance regions are obtained in the single-phase cubic Y_2O_3 -Cu NS-based M-S junction. Driven by an external bias, solid-state electrochemical reactions can be used to analyze the negative resistance in the diode-like junction.²⁰⁴⁻²⁰⁶ The highly localized redox-induced negative resistance is believed to occur solely in the single-phase cubic Y_2O_3 NS due to its unique crystal structure. The cubic Y_2O_3 has a Bixbyite-like structure that has 80 atoms in its unit cell.²⁰⁷ Local structure of cubic Y_2O_3 is shown in Figure 4.5f. In the cubic structure, one fourth of the anions are missing. The oxygen vacancies denoted by open circles arrange along a body diagonal (lower right) or a face diagonal (upper left). Wyckoff positions denote two inequivalent-symmetrical

sites (d-site In and b-site In) that are occupied by metal atoms. The vacancies significantly facilitate the solid-state electrochemical reactions that undergo under the external electrical field. It is the oxygen vacancies that enable the single-phase Y_2O_3 -Cu NS to possess the negative resistance.

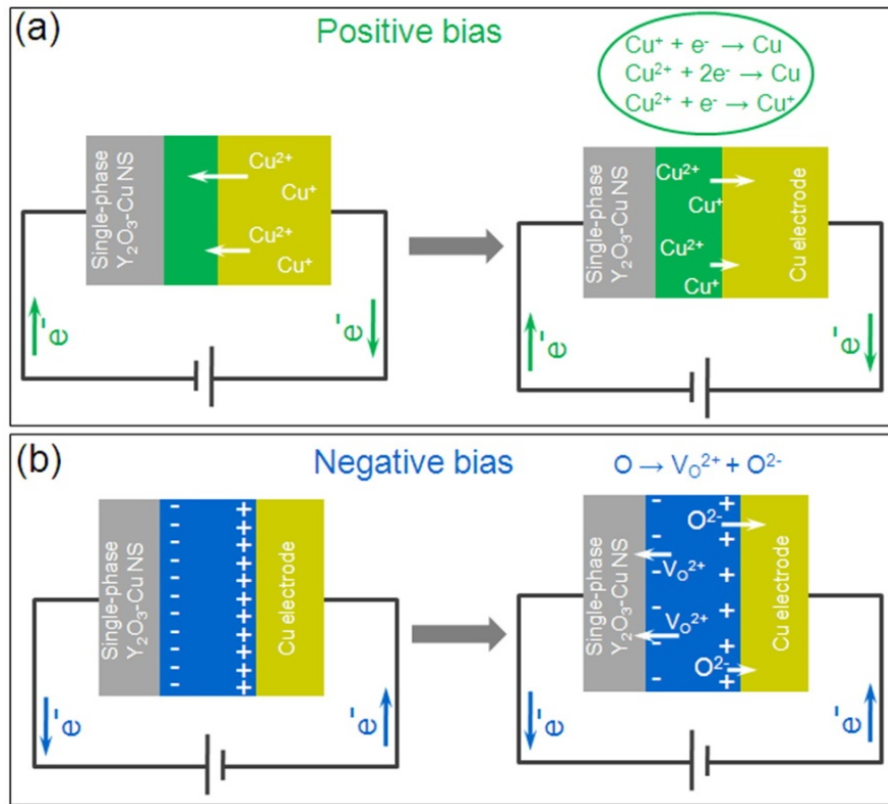


Figure 4.6. Scheme of electronic/ionic transportation under positive (a) and negative (b) bias, respectively.

The reasons why the localized redox reaction occurs in single-phase cubic Y_2O_3 -Cu NS only will be investigated in coming future. In Figure 4.6, we propose a scheme to explain the mechanism dynamically. When a positive bias is applied to the Cu bottom electrode, diode-like electronic transportation occurs across the M-S junction. Initially

driven by the positive bias (the left image of Figure 4.6a), Cu ions from the Cu bottom electrode move toward space-charge region (marked in green in Figure 4.6a) at the M-S interface. Cu ions (Cu^{2+} and Cu^{1+}) have a reduction potential window, ranging from 0.15 V to 0.73 V (comparing to standard hydrogen electrode).^{208,209} Localized redox reactions of Cu ions (circled in Figure 4.6a) occur at the surface of Cu bottom electrode once the positive bias becomes larger than their reduction potential. The Cu ions in the space-charge region will migrate back to the Cu bottom electrode (the right image of Figure 4.6a). The direction of Cu ionic migration is opposite to the forward current that is induced by the electronic transportation across the M-S junction. The Cu ionic migration competes with the forward current under positive bias. The higher the voltage, the more localized redox reactions occur. The negative resistance region I in Figure 4.5e presents once the Cu ionic migration current surpasses the forward current. If a negative bias is applied to the Cu bottom electrode, a depletion region (marked in blue in Figure 4.6b) forms at M-S interface in which an electric field is built. The built-in electric field has an opposite direction to the external bias, and its strength is proportional to the negative bias (the left image of Figure 4.6b). Positively charged V_O^{2+} are generated in the depletion region as oxygen ion (O^{2-}) leaves its lattice driven by the strong built-in electric field (see the solid reaction in Figure 4.6b).²⁰⁴ In addition, the electric field is capable of separating of V_O^{2+} and O^{2-} further, leading to an ionic transportation current (the right image of Figure 4.6b). The direction of the V_O^{2+} and O^{2-} current is opposite to the reverse current and proportional to the applied negative bias. The negative resistance region II in Figure 4.5e is obtained as soon as the V_O^{2+} and O^{2-} current exceeds the

reverse current across the single-phase cubic $\text{Y}_2\text{O}_3\text{-Cu}$ NS-based M-S junction. As V_O^{2+} has higher mobility than metallic ions,^{210,211} the two negative resistance regions are asymmetric.

4.2. α -zirconium phosphate (ZrP) nanoplatelets

Montmorillonite-like zirconium phosphates (i.e. α -ZrP) is such a 2D layered structured materials with high surface energy.^{166,212} The α -ZrP nanoplatelets have been synthesized using the hydrothermal method.^{166,167} The XRD pattern confirms that crystal structure of the ZrP nanoplatelets is alpha phase (Figure 4.7a). The crystal structure is monoclinic (space group $P2_1/n$).²¹³ The morphology of α -ZrP nanoplatelets was characterized using FESEM, TEM, and AFM. As shown in Figure 4.7b, the circular α -ZrP nanoplatelets have sizes ranged from ~ 600 nm to $1 \mu\text{m}$. Those nanoplatelets aggregate together. The TEM image in Figure 4.7c shows the 2D morphology and stacked layers (as indicated by arrows) of the α -ZrP nanoplatelets. The stacked layers are also observed from AFM images of α -ZrP nanoplatelets, as shown in Figures 4.8a and 4.8b. The profile labeled in Figure 4.8b indicates the two dimensional morphology as well. Thickness of the single nanoplatelet is measured using the AFM (Figure 4.8c). A representative thickness of ~ 30 nm is obtained for the α -ZrP. The high aspect ratio is ~ 20 to 30 for the α -ZrP nanoplatelets.

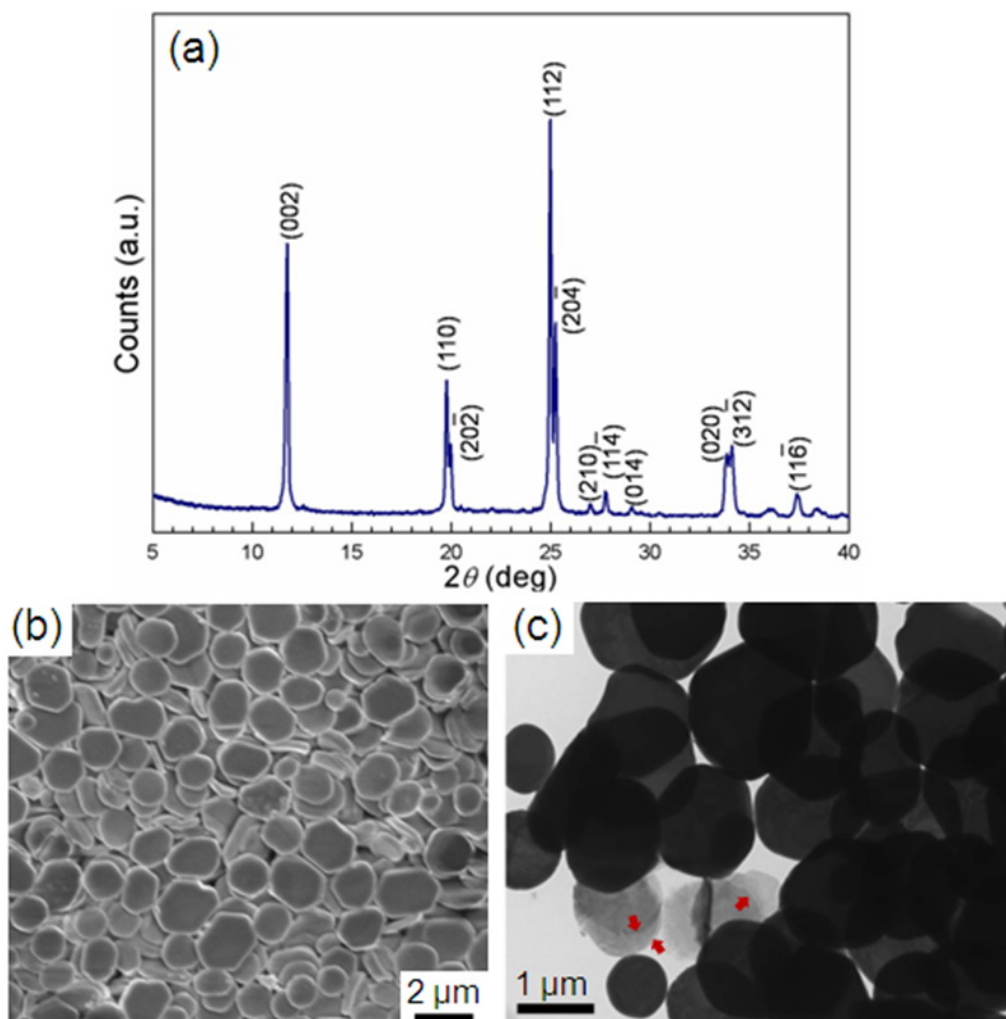


Figure 4.7. XRD pattern (a), and FESEM (b) and TEM (c) images of α -ZrP nanoplatelets.

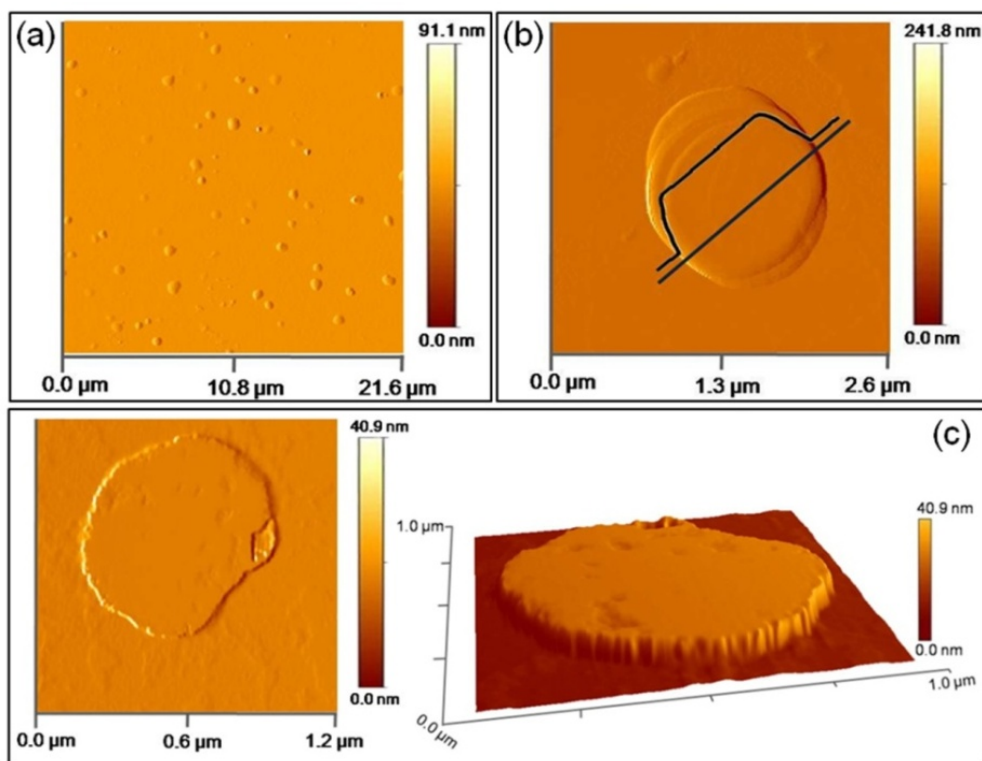


Figure 4.8. AFM images showing stacked layer of α -ZrP nanoplatelets with low (a) and (b) high magnification. (c) AFM images of a single α -ZrP nanoplatelet with 3D visualization.

The α -ZrP nanoplatelets have been reported to have an atomically-layered structure, as schematically shown in Figure 4.9a.^{213,214} Three oxygen atoms from one phosphate group bond to three different zirconium atoms, forming a cross-linked covalent network inside the plane. The fourth oxygen atom of the phosphate is perpendicular to the layer pointed toward the interlayer region. Between two atomic layers of α -ZrP, a basal water molecule resides in a zeolitic cavity, forming a hydrogen bonding with the OH group of the phosphate. Uniformly distributed hydroxyl-phosphate groups, -POH, point into the space between the two layers and maintain the spacing 7.6 Å wide through hydrogen bonding, electrostatic, and van der Waals interactions.

Calculation based on 2θ values of the (002) plane in the XRD pattern (Figure 4.7a) confirms the interlayer spacing.

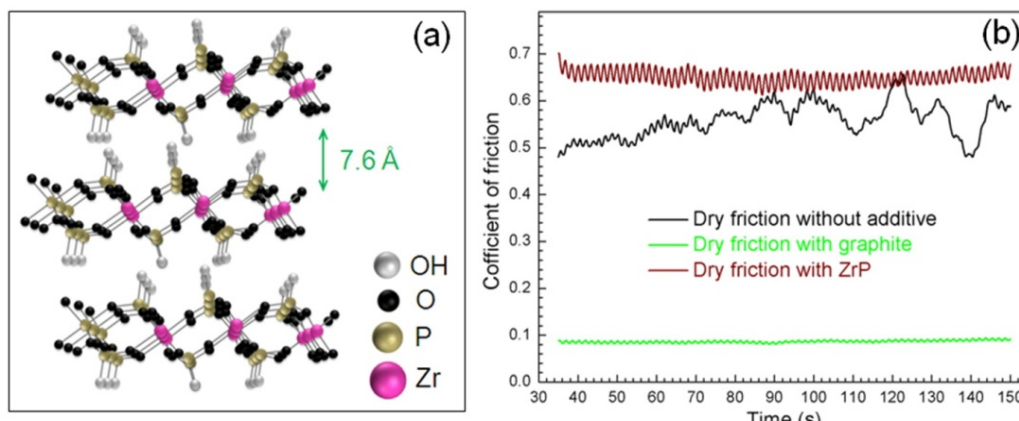


Figure 4.9. (a) Schematic representation of the atomically-layered structure of α -ZrP. (b) Dry friction results with α -ZrP nanoplatelets (top red curve), graphite (bottom green curve), and without any additives (middle black curve).

The inter-atomic-layer interaction (hydrogen bonding) between two adjacent layers of ZrP is stronger than that those in the 2D nanomaterials with van der Waals bondings, e.g. graphite and its derivatives and transition metal dichalcogenides. To prove this, dry friction experiments were carried out and results are shown in Figure 4.9b. In comparison to a known solid lubricant, graphite, it is seen that that α -ZrP nanoplatelets do not show reduced friction while the graphite shows otherwise. As noted that, the dry friction measurements were carried out by moving a steel ball on a stainless steel (Grade 316) plate. The α -ZrP cannot be deemed as a solid state lubricant. There is no report in using these nanoplatelets as additives in lubricants. Therefore the α -ZrP has relatively strong inter-atomic-layer bonding that makes it difficult to be exfoliated and to be used

as a dry lubricant. However, the high surface energy enables the edges and the dangling bonds of the basal planes to be passivated by the environment, i.e. lubricant molecules in this study. This is believed to make the 2D α -ZrP nanoplatelets be an excellent lubricant additives. Details about exploration of the α -ZrP in lubrication can be found in coming chapters.

4.3. Boron-B₂O₃ composited nanoparticles

As a class of hard and lightweight materials with exceptional thermo-stabilizing capability,²¹⁵⁻²¹⁷ boron and its compounds have been used as additives to strengthen engineering materials,²¹⁸ bullet-proof vests,²¹⁹ n- or p-type semiconductors,^{220,221} spin electronics,²²² field emission device,^{223,224} photocurrent switch device,²²⁵ ultraviolet laser device,^{226,227} superconductors working up to 39 K,^{228,229} hydrogen storing fuel cells,^{230,231} neutron detector,^{232,233} and metal working fluid additives.²³⁴ In those applications, all distinctive boronic characteristics, including unusual complex bonding and exceptional electron deficiency, are dependent on the unique crystalline structures of boron developed upon triangular-defined icosahedral subunits.^{235,236} Four main polymorphs, α , β , T, and γ , exist in crystalline boron.²³⁷ Under the atmospheric pressure, α -rhombohedral and β -rhombohedral boron are thermodynamically stable at low (~ 1000 °C) and high (~ 1200 °C) temperatures respectively.²³⁸ Crystalline T-boron phases (α -tetragonal boron and β -tetragonal boron) were prepared through “stabilization of impurity atoms”.^{235,239,240} Recent reports show that γ -B₂₈ can be obtained from β -B via a high temperature (~ 1800 °C) treatment under ~ 20 GPa of pressure.^{237,241} The

structural complexity of the crystalline boron remains the challenge in synthesis of its nanomaterials. In the last decade, efforts have been devoted to preparation of boronic amorphous nanoparticles,²⁴²⁻²⁴⁴ amorphous nanotubes,²⁴⁵ crystalline nanowires,^{246,247} crystalline nanocones,²²⁴ crystalline nanobelts,²²⁵ and crystalline nanoribbons.²⁴⁸ The synthesis methods include pyrolysis, high-energy ball milling, arc decomposition, solution reduction, chemical vapor deposition (CVD), pulsed laser ablation, and radio-frequency magnetron sputtering. Among those, only amorphous or small domain sized (~ 25 Å) boron nanoparticless was synthesized. In this research, a CVD method is developed to synthesize crystalline boron nanoparticles with the help of a B-doped-silicon (Si) catalyzing substrate.

4.3.1. Size-specific synthesis of boron nanoparticles

During the CVD synthesis, argon (Ar) was used as carrier and protective gas, and hydrogen (H_2) was used as a reductant for boron tribromide (BBr_3). B-doped-Si was used as catalyzing substrate. As reported by Oganov et al.,²³⁷ α -rhombohedral boron could only be synthesized from a relatively severe condition, ~ 1200 °C with tens of GPa. Here we are able to synthesize this crystallized boron nanoparticles at 900 °C under the atmospheric pressure. At a temperature lower than 1200 °C, the growth of boron crystal on common solid surfaces is expected to be slow because it is difficult for these surfaces to absorb BBr_3 vapor molecules. However, in the present work, the growth rate is visibly high. This is most likely due to the fact that the B-doped-Si substrate adsorbs BBr_3 vapor quickly, similar to previous reports about Si epitaxy at a low temperature.²⁴⁹⁻²⁵¹ As a

result, less activation energy is needed to break B-Br covalent bonding at the interface between the Si substrate and BBr_3 vapor molecules. H_2 can reduce BBr_3 into elemental boron at a relatively low temperature. Once enough number of boron atoms aggregate together and reach supersaturating levels, boron crystal growth subsequently took place from the nucleated seeds at the liquid (B) - solid (B-doped-Si) interface as continuously shown in Figure 4.10.

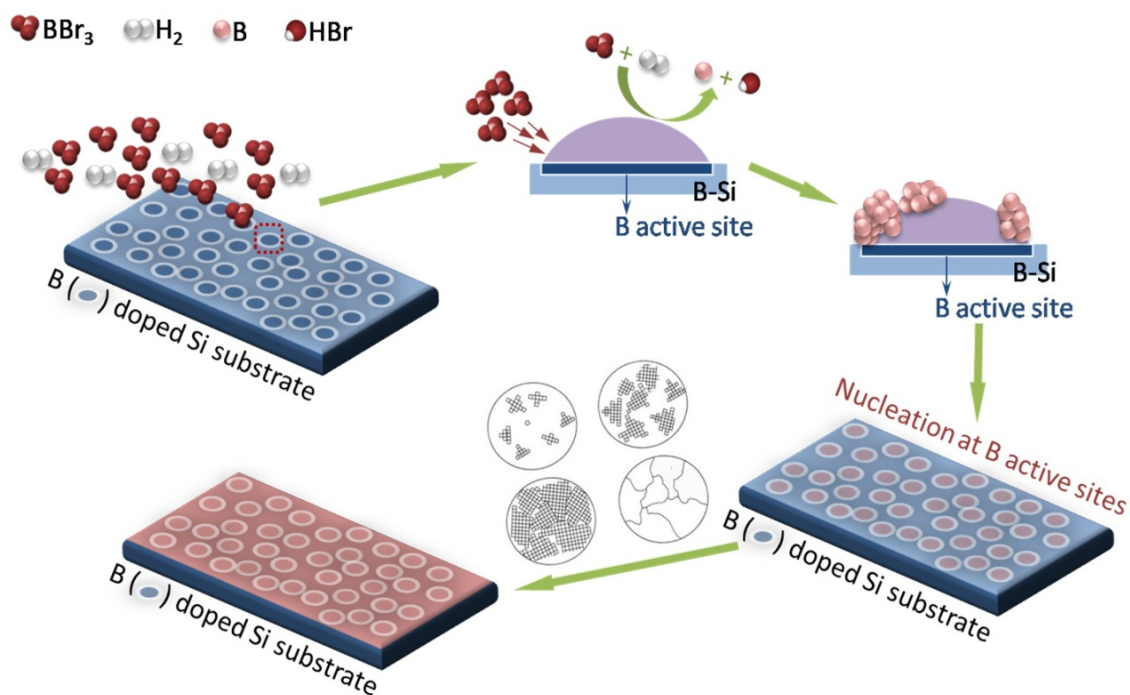


Figure 4.10. Schematic representation of CVD synthesis of the crystalline boron nanoparticles.

The sizes of boron nanoparticles can be regulated through controlling the BBr_3 volatilizing temperature. In our experiment, the sizes of boron nanoparticles increased with elevating BBr_3 volatilizing temperature, as shown in TEM images of Figure 4.11.

Figure 4.11a shows the boron nanoparticles synthesized from the BBr_3 that was kept at 0 °C. We can see that these boron nanoparticles have narrow size distribution and small particle sizes, ~ 5 nm, as shown in Figures 4.11a (circled in red) and 4.11d. The small boron nanoparticles aggregate together due to the surfactant-free CVD process. When we increased the BBr_3 volatilizing temperature, large boron nanoparticles and even micro-particles would appear. Figures 4.11b and 4.11c show boron nanoparticles synthesized from the BBr_3 keeping at 10 °C and 20 °C, sized at ~ 20 nm (Figure 4.11e) and hundreds of nms (Figure 4.11f), respectively. On one hand, sphere is the thermodynamically favorable shape for nanomaterials.^{252,253} It is believed that boron dopants on the B-doped-Si substrate can play a role as activation sites for growth of boron nucleus into boron spherical nanoparticles.²⁵⁴⁻²⁵⁶ These sites attract and absorb BBr_3 vapor molecules. On a B-doped-Si substrate with certain area, there are limited numbers of these sites. On the other hand, the higher the volatilizing temperature, the quicker the BBr_3 volatilizes. At a low volatilizing temperature (e.g. 0 °C), a relatively small amount of BBr_3 is absorbed during a certain period, and they can nucleate on the activation sites in an orderly and moderate manner. As boron nanoparticle grows, the increased tension between it and Si substrate will lead to detaching itself from the activation site. Continuous flow of BBr_3 enables the process, nucleation, growth, and detachment, to go on until synthesis is done as shown in Figure 4.10. The aggregated small boron nanoparticles are thus observed in Figure 4.11a at a low volatilizing temperature. If we increase the volatilizing temperature (e.g., to 10 °C and 20 °C), great amounts of BBr_3 is absorbed by the limited activation sites in a very short period.

Simultaneous nucleation and growth of these boron atoms will lead to formation of large boron nanoparticles, as consecutively shown in Figures 4.11b and 4.11c. Therefore, we prepared several boron nanoparticles with different sizes by CVD.

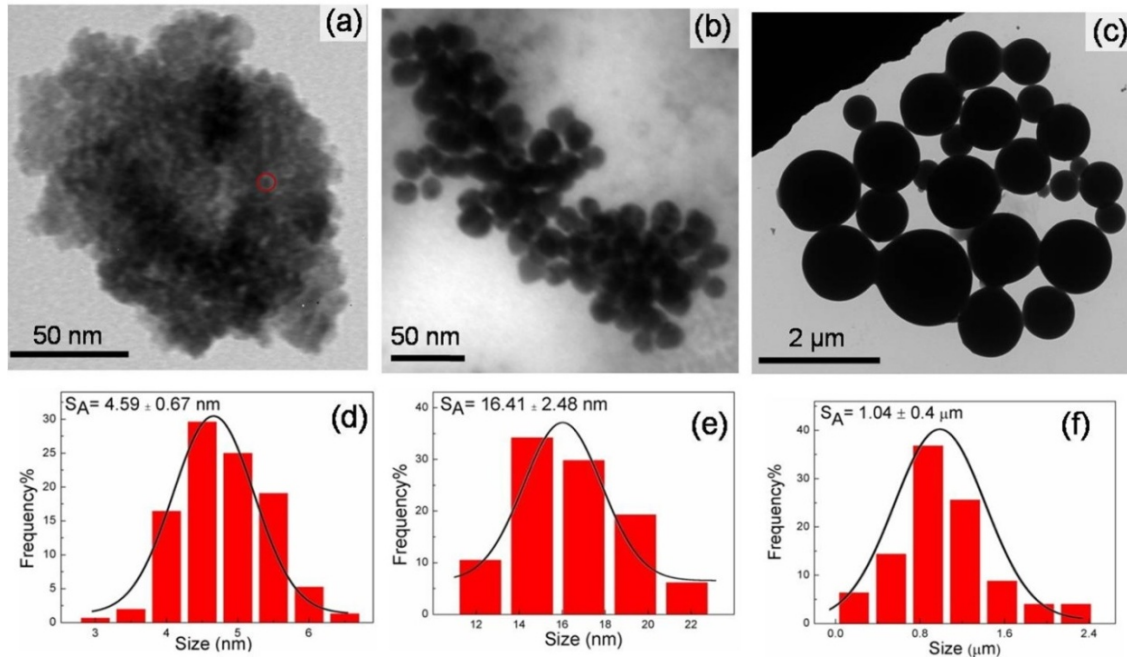


Figure 4.11. TEM images show increased boron nanoparticles' sizes by increasing BBr_3 volatilizing temperatures: 0 °C (a), 10 °C (b), and 20°C (c). Size distributions of those boron nanoparticles are shown in (d) through (f) accordingly.

4.3.2. Preparation of boron- B_2O_3 composited nanoparticles

For later tribological investigation, the as-synthesized boron nanoparticles are surface oxidized. It is well known that boron trioxide (B_2O_3) is an excellent solid lubricant,²⁵⁷⁻²⁵⁹ from which boric acid (H_3BO_3) with 2D nanostructured feature can be generated. In order to confirm the crystalline boron, the example XRD characterization

is shown in Figure 4.12 for the powder synthesized from BBr_3 volatilized at 10°C . All peaks from the black (bottom) plot in this figure are in good agreement with the diffraction patterns of α -rhombohedral boron (JCPDS Files No. 12-0377). This indicates that the CVD method is an effective way to prepare crystalline boron under an ordinary pressure and at the temperature much lower than previously reported.^{221,224,246} After synthesis of boron powders, the same is oxidized by keeping the sample at 900°C in the air for 45 minutes. As marked on red (top) plot of Figures 4.12, several peaks match diffraction patterns of B_2O_3 (JCPDS Files No. 06-0297). In addition, there are some relatively weak α -rhombohedral peaks that are compatible with the same of boron. Among these B_2O_3 peaks, it is worth noting that strong diffraction appeared at 2θ of $\sim 28^\circ$ that are attributed to the diffraction happened on the B_2O_3 crystalline plane of (310). TEM image showing in inset of Figure 4.12 clearly reveal that a surface oxidizing layer of B_2O_3 is formed on the crystalline boron nanoparticles. The composite boron- B_2O_3 nanoparticles are prepared for tribological application.

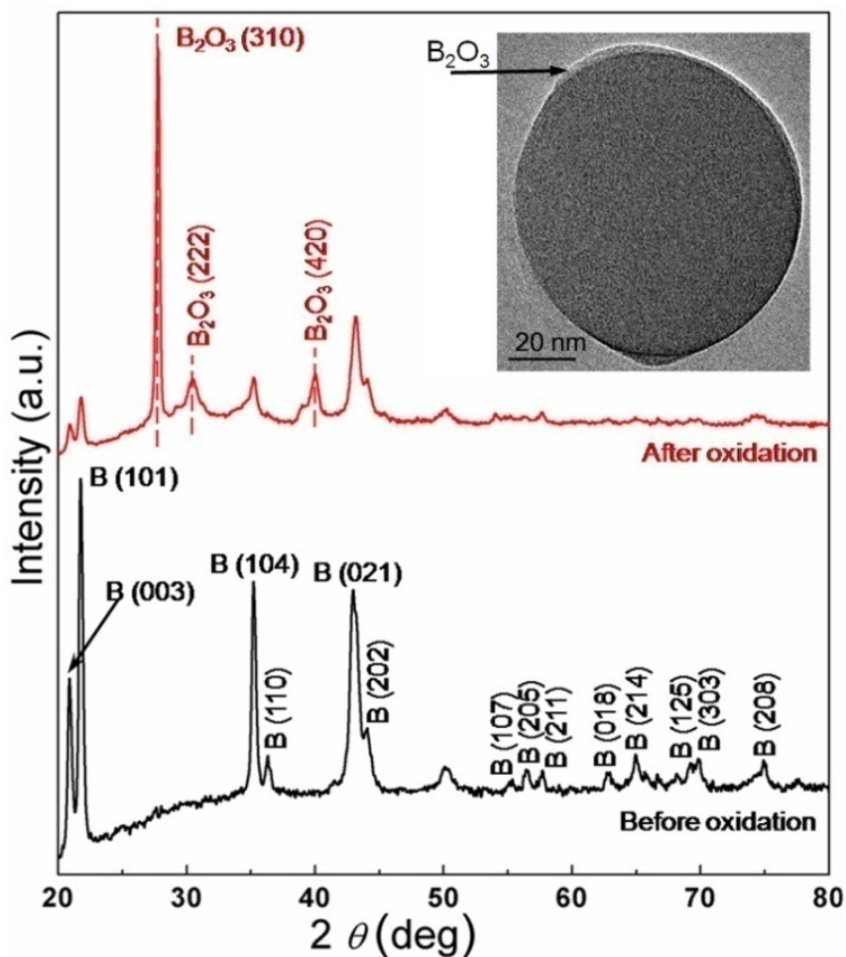


Figure 4.12. XRD patterns for the boron nanoparticles before (black, bottom) and after (red, top) oxidation. Inset: TEM image of a boron-B₂O₃ composited nanoparticles.

4.4. Summary

In this chapter, synthesis and characterization of three nanomaterials are discussed. They are yttrium oxide (Y₂O₃) nanosheets, α -zirconium phosphate (ZrP) nanoplatelets, and boron (B)-B₂O₃ composited nanoparticles.

Synthesis and characterization of Y₂O₃ nanomaterials are introduced first. During the hydrothermal reactions, 2D Y₂O₃ nanoparticles were synthesized by controlling the

reaction temperature. A transformation of the Y_2O_3 nanosheets from multiphase to single-phase was observed during the synthesis. An interesting negative resistance was obtained in the single-phase Y_2O_3 -Cu nanosheet. It is the unique 2D nano-morphology that enables Y_2O_3 nanosheet such a novel property.

Simultaneously, the facile hydrothermal method has been used to synthesize the α -ZrP nanoplatelets. Characterizations confirmed their unique two-dimensional morphology at nanoscale. The 2D morphology of α -ZrP nanoplatelet was due to its atomically-layered structure.

Boron- B_2O_3 composited nanoparticles are the third nanomaterials synthesized in this research. They were prepared at low temperature under atmospheric pressure using a substrate-catalyzed CVD method. 2D nanostructured boric acid is expected to be formed from the surface oxide layer of B_2O_3 in the later tribological processing.

As discussed in the Chapters I and II, 2D nanomaterials could be a promising candidate for the desirable viscosity modification in the fluidic lubrication. The 2D morphology and structural features those three nanomaterials will be utilized in tribological examination and the rheological investigation in the following chapters.

CHAPTER V

TRIBOLOGICAL EVALUATION OF 2D NANOPARTICLES[†]

This chapter explores tribological applications of 2D nanoparticles. It contains four sections: the first is to investigate 2D nanoparticles as additives in lubrication; the second is to examine the lubricating behavior under different dynamic conditions; the third is to discuss the intermolecular interaction between the lubricant molecules and the additive surface; and the fourth is to evaluate the benefits of the low-friction process in chemical-mechanical planarization (CMP).

5.1. Frictional behavior

Friction is the resistance to the relative motion during one solid body is in contact with another and moves tangentially.^{260,261} The resisting tangential force is known as the friction force that has an opposite direction to the body motion. Friction needs to be minimized when energy loss occurs. When two rough solids are in a sliding contact, friction presents due to difference in intermolecular and surface forces, ruggedness, roughness, and unevenness of surface. The asperity contacts cannot be avoided if the applied load is high and the speed of motion is low. The 2D sheet-like nano-additives are

[†] Part of this chapter reproduced with permission from “Boron-based nanoparticles for chemical-mechanical polishing of copper films” by Xingliang He, et al., *ECS J. Solid State Sci. Technol.*, **2013**, 2, P20-P25 (Copyright © 2013, The Electrochemical Society); “Y₂O₃ nanosheets as slurry abrasives for chemical-mechanical planarization of copper” by Xingliang He, et al., *Friction*, **2013**, 1, 327-332 (Copyright © 2013, Springer); and “ α -zirconium phosphate nanoplatelets as lubricant additives” by Xingliang He, et al., *Colloids Surf., A*, **2014**, 452, 32-38 (Copyright © 2014, Elsevier).

thus introduced into a non-aqueous (mineral oil) or aqueous (DI water) lubricant to show the promising potential in reducing friction. The friction experiments discussed in this chapter were carried out via a pin-on-disk configuration consisting of a rotating glass disk and a fixed E52100 alloy steel pin.

5.1.1. 2D nanoparticles as additives in lubricants

In order to improve mechanical efficiency and reduce energy loss, friction-induced surface damage can be avoided by adding an appropriate additive to lubricants. Three different Y_2O_3 nanomaterials are used as additives for mineral oil to identify the importance of morphology at nanoscale in friction reduction. Figure 5.1 shows the transmission electron microscope (TEM) images of Y_2O_3 NS, Y_2O_3 nanoparticles (NP), and Y_2O_3 nanowires (NW) used in the pin-on-disk frictional experiment. A 2D nano-shape is observed from TEM image (Figure 5.1a) for the square Y_2O_3 NS (316.6 ± 49.4 nm side and 16.1 ± 0.9 nm thick). The characteristic size of Y_2O_3 NP is measured to be 18.2 ± 3.4 nm as marked in green in the TEM image of Figure 5.1b. This size is highly comparable with the thickness of the Y_2O_3 NS. The diameter and the length of the Y_2O_3 NW are measured to be ~ 100 nm and ~ 15 μ m, respectively (Figure 5.1c). The contacted counterparts undergo a friction process when rotational speed is low.

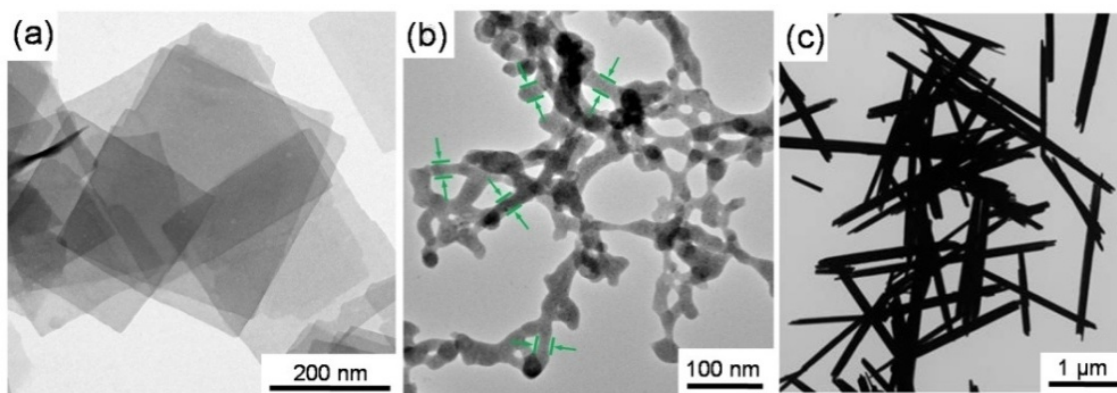


Figure 5.1. TEM images of the Y₂O₃ NS (a), Y₂O₃ NP (b), and Y₂O₃ NW used in experiments.

In Figure 5.2, reduction in coefficient of friction (green curves) is observed solely for the mineral oil that contains 0.5 wt % of Y₂O₃ NS. The parameters used in the friction experiments are also indicated in each figure. The friction coefficients are reduced by ~ 20 %, ~ 12 %, and ~ 20 %, respectively in Figure 5.2a through 5.2c. On the contrary, coefficient of friction shows a notable increase when the same concentration (0.5 wt %) of Y₂O₃ NP and Y₂O₃ NW are present in mineral oil. In particular, abnormal variation of friction coefficient with time is observed for mineral oil containing Y₂O₃ NW under smaller applied load (red curves in Figures 5.2b and 5.2c). This is believed to be caused by rotation or spin of the NW in the mineral oil during the friction. Therefore, the unique 2D morphology at nanoscale enables Y₂O₃ NS to perform as an effective additive in decreasing the friction. It is indeed necessary to explore the 2D sheet-like nanomaterials for friction reduction.

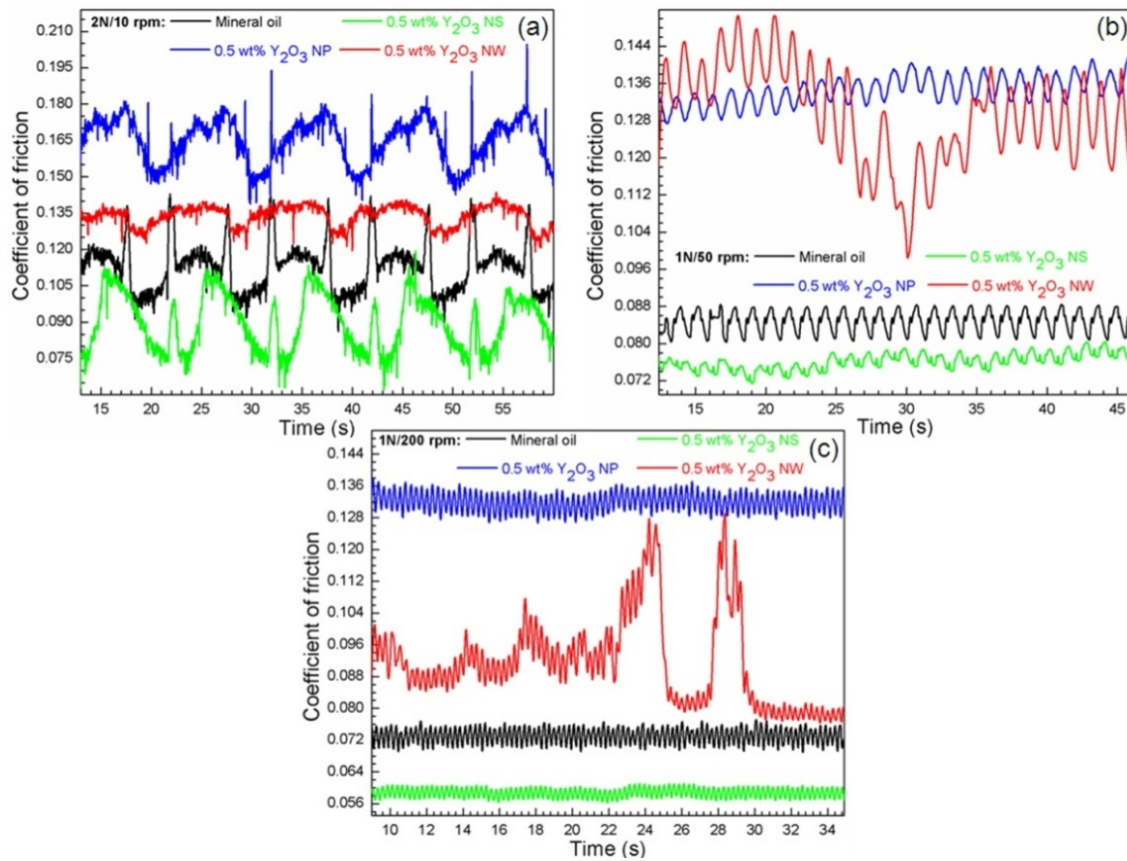


Figure 5.2. Under different friction tests, comparison of friction coefficient of mineral oils without (black curve) and with different types (colored curves) of Y₂O₃ nanomaterials additives (0.5 wt %).

5.1.2. Roles of concentration in friction

Before systematic investigation of friction reduction, critical concentration of the 2D nano-additives for a certain type of base liquid should be evaluated. For the non-aqueous liquid (mineral oil), three different concentrations (1 wt %, 0.5 wt %, and 0.1 wt %) of Y₂O₃ NS were selected initially. During those friction experiments, the speed was fixed at 10 rpm, and three loads, 1 N, 2 N, and 3 N, were applied. The results are shown in Figure 5.3. High concentration of the Y₂O₃ NS significantly increases the friction of

coefficient, as shown by the blue curves in Figures 5.3a through 5.3c. The friction coefficient fluctuates markedly with time during the test, comparing to the pure mineral oil (black curves in Figure 5.3) or the mineral oil containing low concentration of Y_2O_3 NS (red and green curves in Figure 5.3). The friction is reduced by $\sim 30\%$, $\sim 20\%$, and $\sim 25\%$ in Figures 5.3a, 5.3b, and 5.3c, respectively, using 0.5 wt % of Y_2O_3 NS additives (red curves). The lower concentration (0.1 wt %) Y_2O_3 NS reduces the friction coefficient as well (green curves in Figure 5.3), yet not as much as the mineral oil containing the 0.5 wt % additives. Among the three concentrations we measured, 0.5 wt % is the most suitable percentage for Y_2O_3 NS additives in mineral oil.

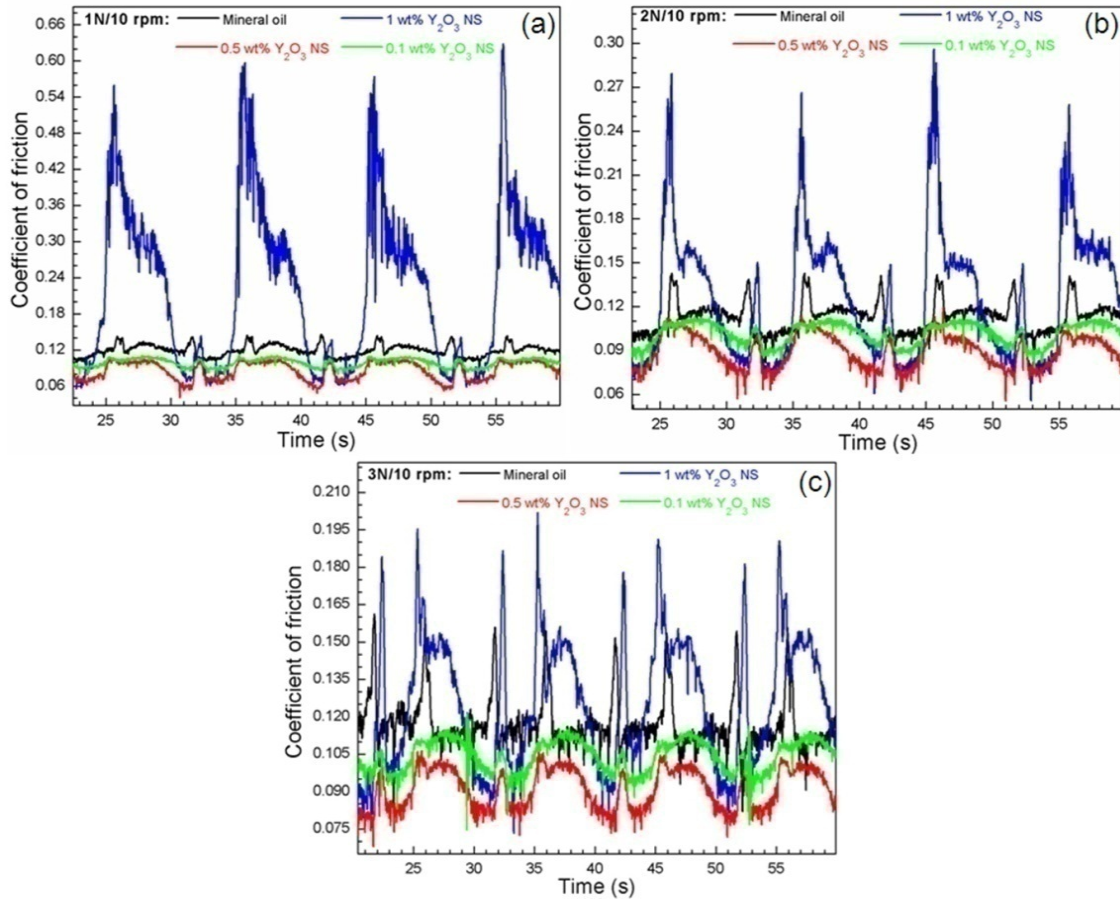


Figure 5.3. Under different friction tests, comparison of friction coefficient of mineral oils without (black curve) and with different concentrations (colored curves) of Y_2O_3 NS additives.

It is understandable that high concentration of Y_2O_3 NS increases coefficient of friction. The high concentration of additives leads to significant aggregation of the additives. The aggregation-induced abrasion or dry contact is responsible for the significant friction. Besides, non-uniform distribution of additives in the base liquid presents when aggregation occurs, resulting in the great fluctuation of friction coefficient. There is a critical concentration level for additives in base liquid, as 0.5 wt % of Y_2O_3 NS is found for mineral oil. The greatest friction reduction could be achieved

at this concentration. An important role played by the 2D nanosheet additives is that it can deliver lubricant molecules into the asperity-contacted area between two solid surfaces. If concentration is too low, limited amount of Y_2O_3 NS cannot carry enough lubricant molecules to the localized contact area. The friction can be decreased to a limited level. For the other base liquids and different 2D nano-additives, the critical concentration level would be different from each other. On the basis of mineral oil, 0.5 wt % is the optimized additive concentration for Y_2O_3 NS.

5.2. Effects of experimental parameters on friction

By dividing the friction force with the force pressing two bodies together, a dimensionless scalar value (the coefficient of friction) is obtained. The frictional resistance can be deemed as a constant value provided the speed is low. The friction force required to keep an object moving at a constant velocity is normally smaller than that to move it starting from rest. Coefficient of kinetic friction is used more frequently than coefficient of static friction in depicting two moving surfaces. This coefficient is highly dependent on the applied loads and the rotational speeds in the present study. In order to prove that the 2D nanoparticle additives can certainly be a friction-reduction additive, a dynamic study of friction coefficient by varying the applied load and the rotational speed is necessary.

5.2.1. Effects of applied loads

Friction reducing behavior is studied firstly with the appearance of 2D nano-additives in mineral oil. During the investigation of the critical concentration level (Figure 5.3), low concentrations (0.5 wt % and 0.1 wt %) of Y_2O_3 NS show capability of friction reduction at a low rotational speed (10 rpm) and under different applied loads (3 N, 2 N, and 1 N). In the other pin-on-disk experiments (Figures 5.4 and 5.5), a moderate rotational speed was fixed at 300 rpm while another three different small loads, 1 N, 0.5 N, and 0.25 N, were applied. Such results are shown in Figure 5.4. When the optimized additive concentration (0.5 wt %) is used, Y_2O_3 NS is able to decrease coefficient of friction significantly. The friction coefficient is reduced by ~ 25 %, ~ 35 %, and ~ 40 % under applied loads of 1 N (Figure 5.4a), 0.5 N (Figure 5.4b), and 0.25 N (Figure 5.4c), respectively.

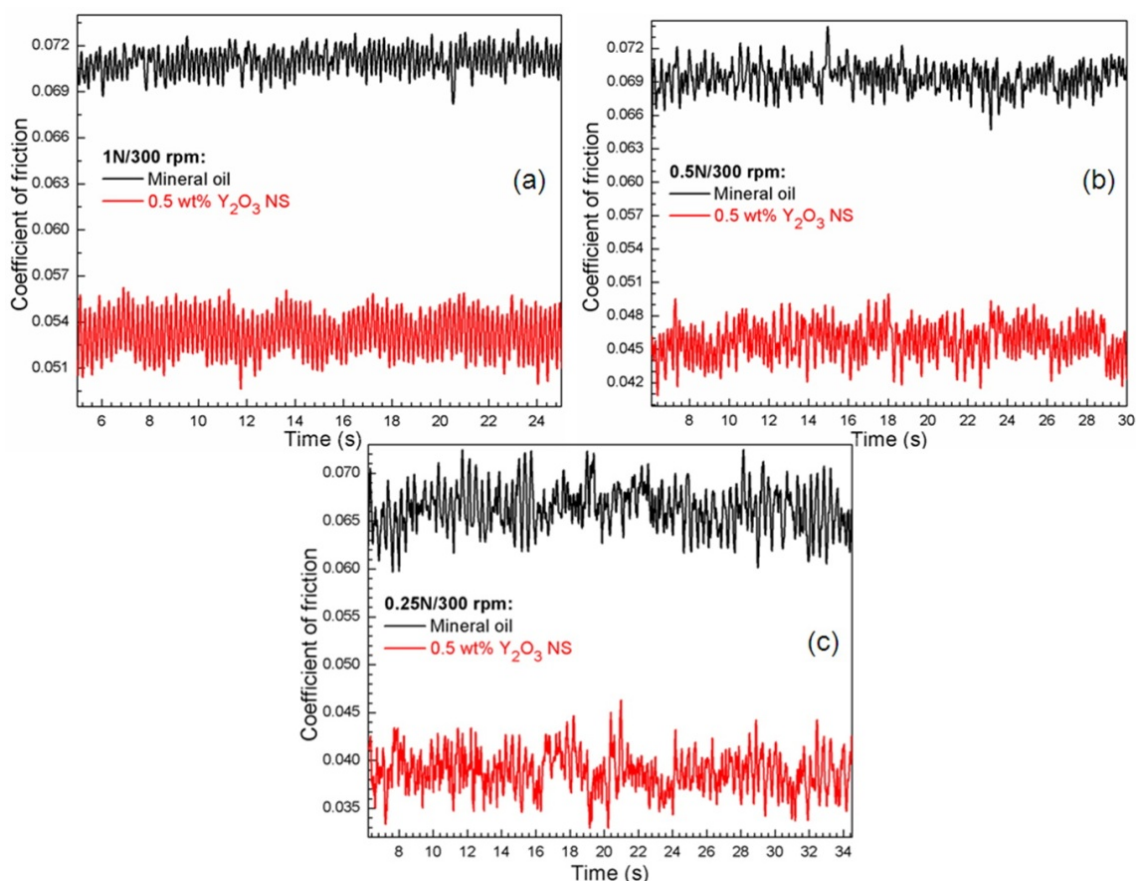


Figure 5.4. Under different loads, comparison of friction coefficient of mineral oils without (black curve) and with 0.5 wt % of Y_2O_3 NS additives (red curve).

Simultaneously, frictional performance of mineral oil containing 0.5 wt % α -ZrP nanoplatelets is studied as well, under different applied loads and at the fixed rotational speed of 300 rpm. The results are shown in Figure 5.5. It is observed that the coefficient of friction is reduced by $\sim 55\%$, $\sim 65\%$, and $\sim 50\%$ under applied loads of 1 N (Figure 5.5a), 0.5 N (Figure 5.5b), and 0.25 N (Figure 5.5c), respectively. α -ZrP nanoplatelet is found to be a better friction-reducing additives than Y_2O_3 NS. As we discussed in Chapter III, there are plenty of uniformly distributed hydroxyl-phosphate groups (–

POH), on the surface of α -ZrP nanoplatelet, while the surface of Y_2O_3 NS is decorated with hydroxyl groups ($-OH$). The $-POH$ group has stronger polarity than $-OH$ group, enabling the α -ZrP nanoplatelets to have higher surface energy than Y_2O_3 NS. The high surface energy enables the edges and the dangling bonds of the basal planes to be passivated by the organic molecules from mineral oils. Comparing to α -ZrP nanoplatelets, Y_2O_3 NS has poorer intermolecular interactions with the lubricant liquid. Therefore, α -ZrP nanoplatelets are believed to deliver more lubricant molecules to the localized asperity-contact region, leading to more reduction in the coefficient of friction. When we applied a constant rotational speed, both 2D nano-additives reduce friction significantly.

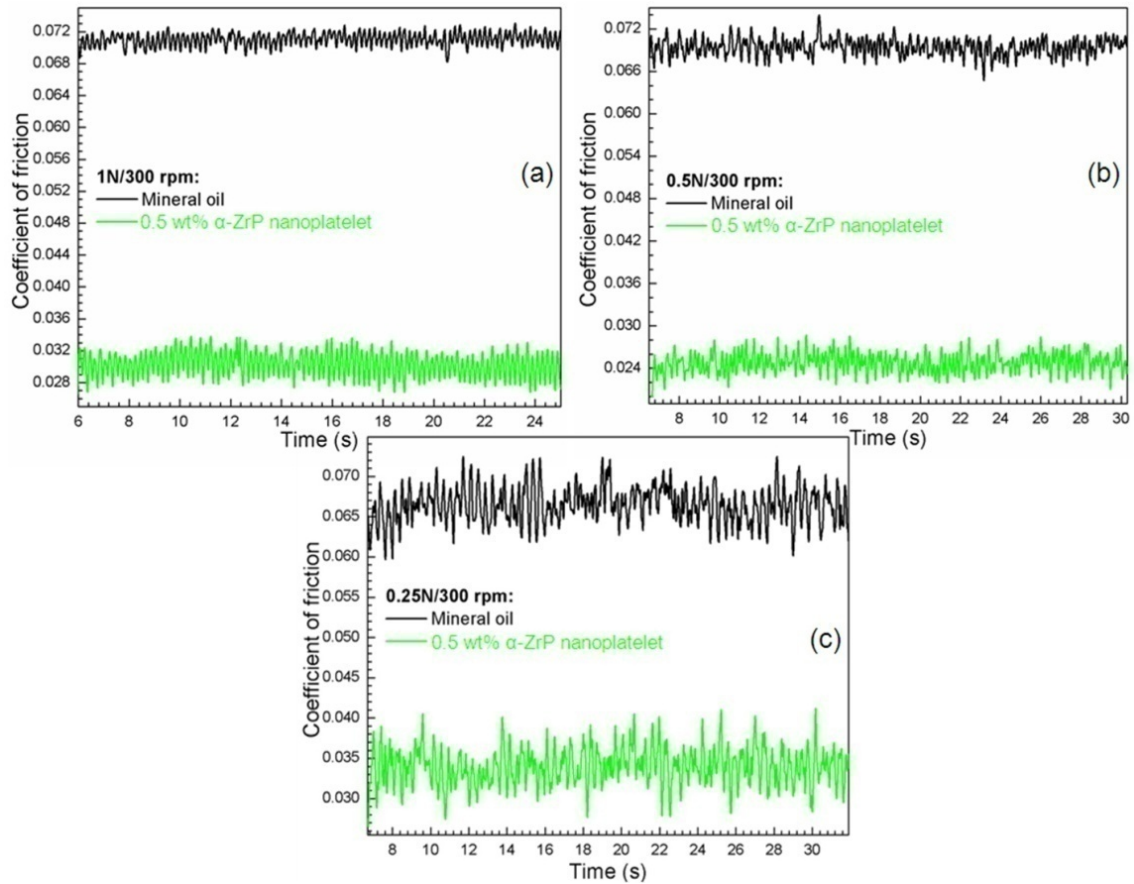


Figure 5.5. Under different loads, comparison of friction coefficient of mineral oils without (black curve) and with 0.5 wt % of α -ZrP nanoplatelet additives (green curve).

5.2.2. Effects of rotational speeds

Besides applied load, rotational speed is another critical dynamic parameter that can noticeably affect the friction between two relatively-motion solid bodies. The assumption that friction force is independent of relative velocity of two moving surface is part of the surface-friction standard model. For a narrow range of low-speed friction, the assumption is approximately true. However, it is found that the friction depends on the square or higher power of the relative velocity. This is mainly due to air friction or

liquid-involved friction with the increased rotational speed. Figures 5.6 and 5.7 show the frictional results of mineral oil containing additives of Y_2O_3 NS and α -ZrP nanoplatelets, under a fixed load (1 N) and at different rotating speeds (30 rpm, 50 rpm, and 100 rpm). 0.5 wt % of Y_2O_3 NS in mineral oil reduces coefficient of friction by $\sim 20\%$, $\sim 10\%$, and $\sim 15\%$ at rotational speeds of 30 rpm (Figure 5.6a), 50 rpm (Figure 5.6b), and 100 rpm (Figure 5.6c), respectively. Similarly, 0.1 wt % of α -ZrP nanoplatelets also shows reduction of friction coefficient in mineral oil, by $\sim 35\%$, $\sim 20\%$, and $\sim 60\%$ at rotational speeds of 30 rpm (Figure 5.7a), 50 rpm (Figure 5.7b), and 100 rpm (Figure 5.7c), respectively. Thus, the both 2D nanomaterials prepared in this research are capable of reducing friction regardless of friction-dynamic variation (either applied loads or rotational speeds).

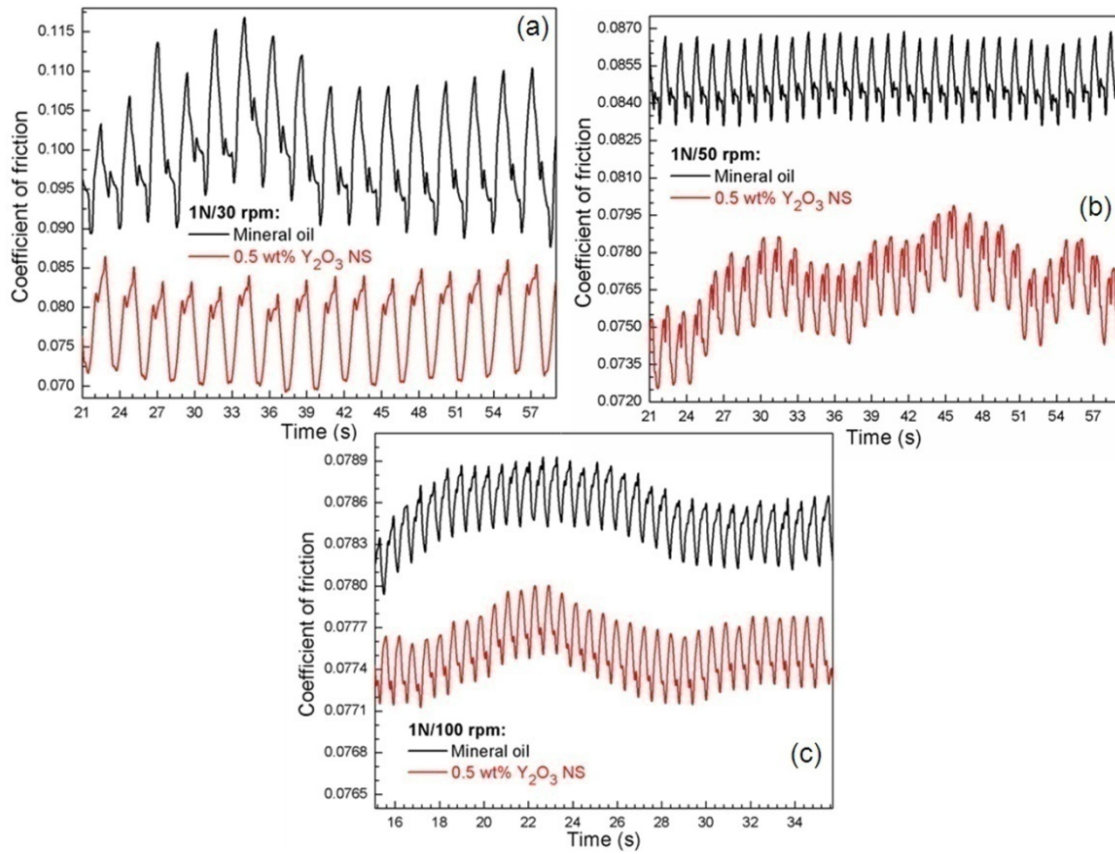


Figure 5.6. Under different speeds, comparison of friction coefficient of mineral oils without (black curve) and with 0.5 wt % of Y_2O_3 NS additives (red curve).

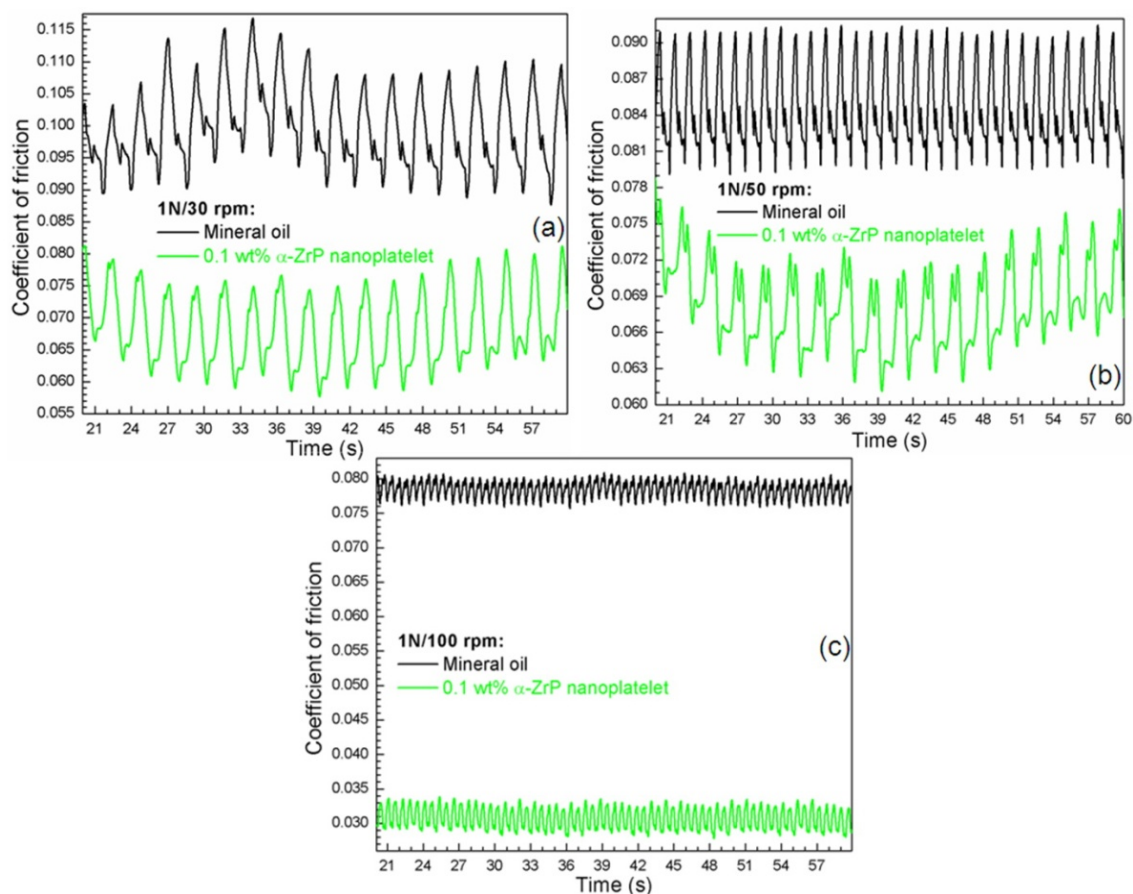


Figure 5.7. Under different speeds, comparison of friction coefficient of mineral oils without (black curve) and with 0.1 wt % of α -ZrP nanoplatelet additives (green curve).

5.2.3. Aqueous lubricants

In addition to the organic liquids, aqueous solution can also be used as carrier for the 2D nano-additives. The pin-on-disk frictional behavior in the presence of DI water is characterized. As water molecules have markedly smaller size than long-chain alkane molecules of mineral oil, severe asperity contact between two solid surfaces occurs. This induces obvious friction in experiments. As shown in Figure 5.8, the friction coefficient is high at the initial stage, due to friction-induced oxidation and elastic or plastic

deformation on the surface. The coefficient starts to drop as the friction continues because of surface roughing and debris effects.²⁶⁰

In order to verify whether the 2D nano-additives can reduce friction in an aqueous media, the friction test was carried out with the same pin-disk configuration but in DI water. As shown in Figure 5.8, α -ZrP nanoplatelets are found to reduce coefficient of friction at an extremely low concentration (0.002 wt %, the bottom green curve) when the sliding occurs in DI water. 0.1 wt % α -ZrP nanoplatelets additives increase the friction coefficient (see the top blue curve in Figure 5.8) for the similar frictional experiment in DI water. The additive concentration needed for the friction reduction in aqueous environment (0.002 wt %) is much smaller than that in non-aqueous environment (0.1 wt %). This can be understood by the significantly smaller size of water molecule than organic oil molecules. On the same area of α -ZrP nanoplatelets, much more water molecules can be attached than the long-chain alkane molecules of mineral oil. Very small amount of α -ZrP nanoplatelets is able to carry enough water molecules that are necessarily needed for friction reduction. With the -POH group on its surface, α -ZrP nanoplatelets would interact with water molecules easily. The oxygen is more electronegative than the hydrogen and phosphate. As a result, the polarity of P-O-H can be increased due to that the electron density is pulled away from the hydrogen and phosphate by the oxygen.²⁶² The group becomes electrophilic, and induces strong interaction with water molecules via hydrogen bonding. In short, the 2D nano-additive shows a promising potential to reduce friction in the aqueous lubricant.

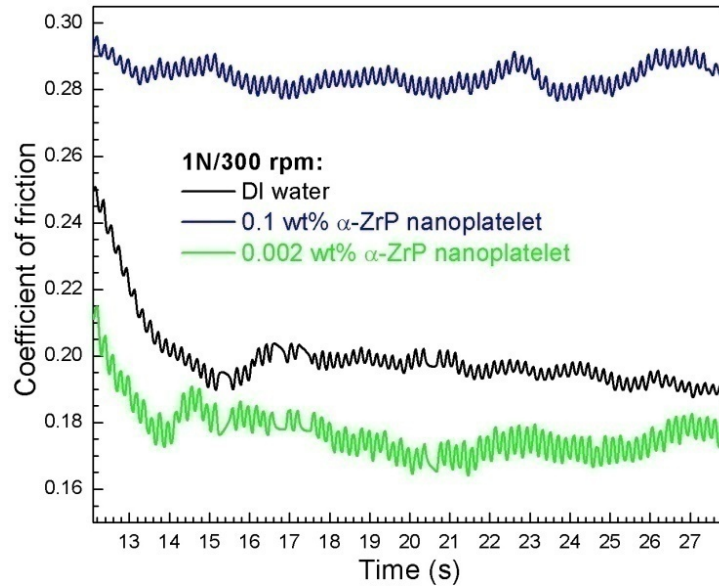


Figure 5.8. Example comparison of friction coefficient of DI water without (middle black curve) and with 0.1 wt % (top blue curve) and 0.002 wt % (bottom green curve) of α -ZrP nanoplatelet additives.

5.3. Intermolecular interactions between fluid molecules and nano-additives

Our results have shown that friction can be effectively reduced with addition of 2D nanoparticles. It is the Y_2O_3 NS or α -ZrP nanoplatelet that is able to carry the lubricant molecules into the localized contact region, leading to the friction reduction. The friction reduction could be caused by intermolecular interactions between the lubricant molecules and the additives.

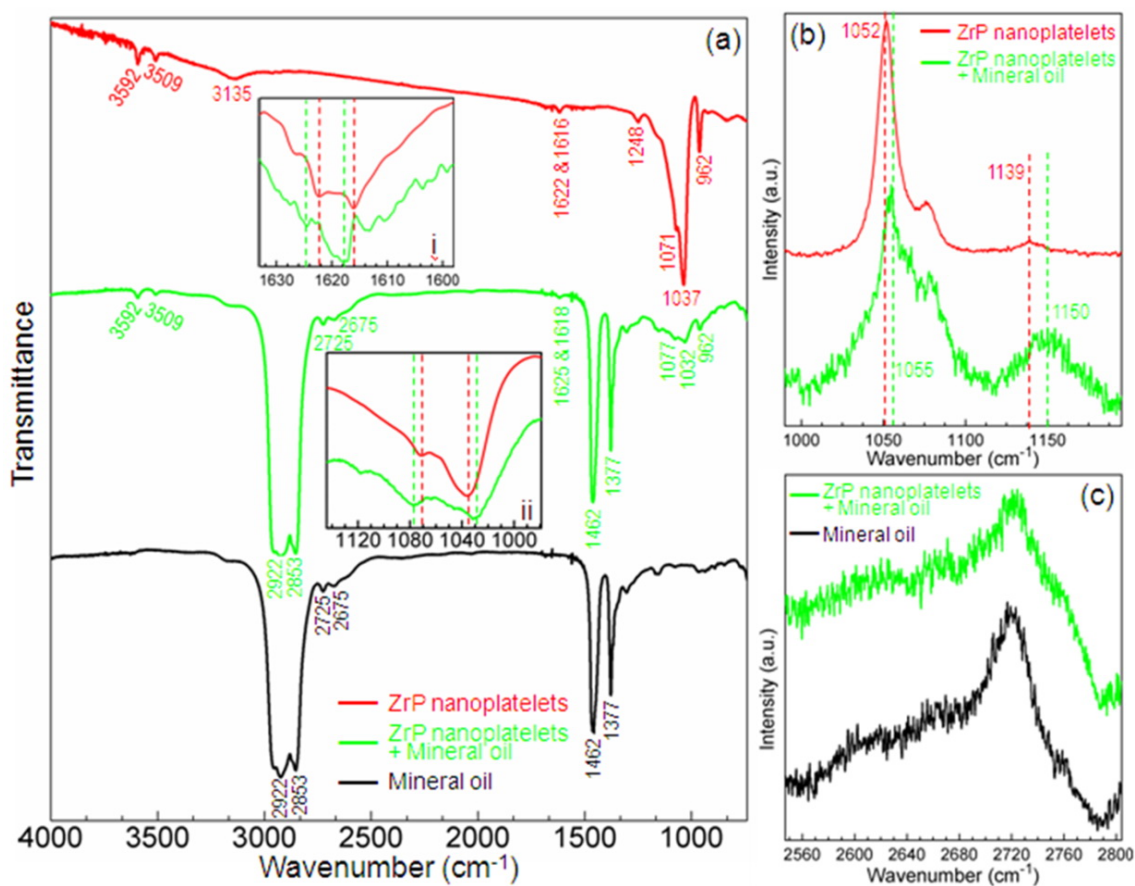


Figure 5.9. (a) Comparison of infrared spectra of α -ZrP nanoplatelets (top red curve), mineral oil (bottom black curve), and mineral oil containing 0.5 wt % α -ZrP nanoplatelets (middle green curve). (b) Comparison of Raman spectra between α -ZrP nanoplatelets (top red curve) and mineral oil containing 0.5 wt % α -ZrP nanoplatelets (bottom green curve). (c) Comparison of Raman spectra between mineral oil containing 0.5 wt % α -ZrP nanoplatelets (top green curve) and pure mineral oil (bottom black curve).

Interaction between the organic molecules in mineral oil and additives was investigated. Figure 5.9 are the infrared and Raman spectra. The mineral oil is a mixture of alkanes in the C15 to C40 range. Its infrared spectrum (bottom black plot in Figure 5.9a) shows a series of characteristic vibrations on the long-chain alkane molecules: C-H

(CH₃-CH₂-) asymmetric and symmetric stretching vibrations (2853 and 2922 cm⁻¹), C-H (-CH₂- and -CH₃) bending deformation (1377 and 1462 cm⁻¹), and C-H aldehyde stretching vibration (2675 and 2725 cm⁻¹). Other characteristic vibration modes are observed from the infrared spectrum of α -ZrP nanoplatelets (top red plot in Figure 5.9a): -O-H stretching vibrations in water molecules (~ 3509 and 3592 cm⁻¹), P-O-H stretching vibration (3135 cm⁻¹), intermediate vibrations of water molecules (1616 and 1622 cm⁻¹), P-O-H deformation vibration (1248 cm⁻¹), vibrations of the orthophosphate group (1037 and 1071 cm⁻¹), and formation of pyrophosphate groups (962 cm⁻¹).^{263,264} Shift of some of those vibration modes are observed after mixing α -ZrP nanoplatelets with mineral oil (middle green plot in Figure 5.9a). Inset i of Figure 5.9a shows shifts of intermediate vibrations of water molecules (1616 \rightarrow 1618 cm⁻¹ and 1622 \rightarrow 1625 cm⁻¹, respectively). Vibration mode shifts in the orthophosphate group (1037 \rightarrow 1032 cm⁻¹ and 1071 \rightarrow 1077 cm⁻¹) are shown in inset ii of Figure 5.9a with peak broadening. The shifts represent modification of vibration-induced stress/strain states on the surface of α -ZrP nanoplatelets. The enlarged width indicates that the orthophosphate groups are involved in interactions with organic molecular groups from the mineral oil. In Figure 5.9b, characteristic vibration-based inelastic scattering from orthophosphate group of α -ZrP nanoplatelets displays shifts and peak widening on Raman spectra. A peak broadening is also observed in Figure 5.9c for the C-H aldehyde stretching Raman spectra. It is evident that long-chain organic molecules in mineral oil interact with the surface of α -ZrP nanoplatelets. The interaction results in friction and fluid drag reduction.

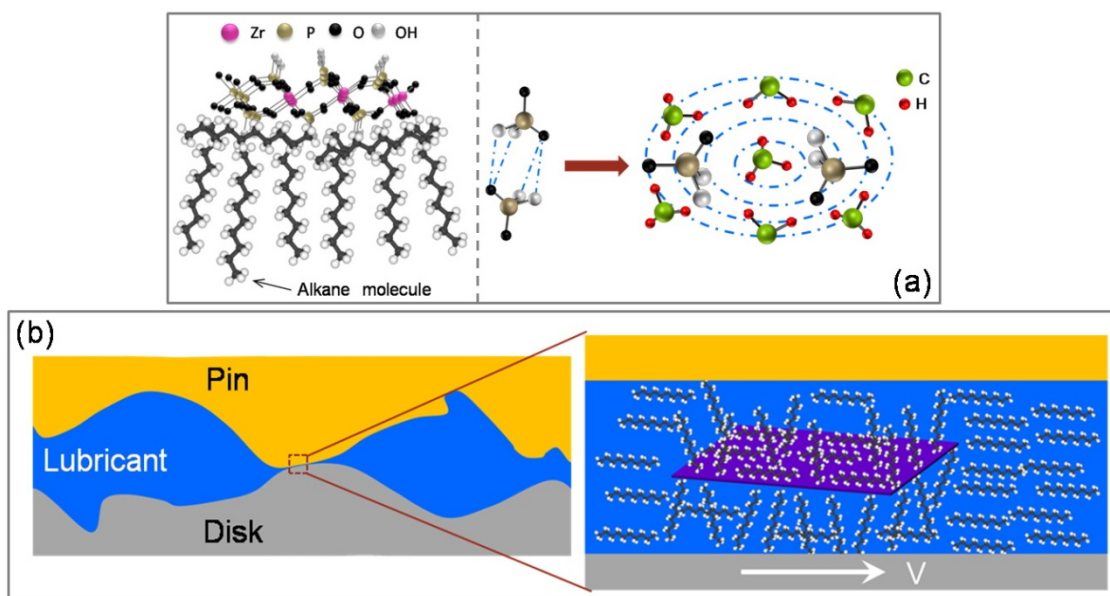


Figure 5.10. (a) Schematics showing interaction between lubricant molecules and α -ZrP surface (the left), and formation of dipole-dipole complex (the right). (b) Schematic explanation of friction reduction with localized asperity-contact.

In order to understand the mechanisms of friction reduction in the localized asperity-contact, a schematic is shown in Figure 5.10. Interaction between lubricant molecules and the surface of 2D nanomaterials is believed to be the principle reason. As an instance, the α -ZrP having a layered structure (see the Figure 3.9a in Chapter III) is discussed here.^{213,214} Three oxygen atoms from one phosphate group bond to three different zirconium atoms, forming a cross-linked covalent network inside the plane. The fourth oxygen atom of the phosphate is perpendicular to the layer pointing toward the interlayer region. Between two atomic layers of α -ZrP, a basal water molecule resides in a zeolitic cavity, forming a hydrogen bonding with the OH group of the phosphate. After adding the α -ZrP nanoplatelets in mineral oil, the alkane molecules, interact with the

surface of α -ZrP via van der Waals dispersion forces (the left of Figure 5.10a). In the α -ZrP nanoplatelets, the hydrogen bonding is mainly between phosphate groups and/or water molecules.^{265,266} Mineral oil brings more organic groups, e.g. methyl, methylene, aldehyde, etc, in contact with the surface of α -ZrP nanoplatelets. The shifts and peak broadening in infrared and Raman spectra suggest the formation of a dipole-dipole complex among these functional groups (the right of Figure 5.10a). In the localized contact region, protuberant areas are in contact due to surface asperity (the left of Figure 5.10b). Mineral oil is resisted due to the contact, inducing the friction. When the 2D sheet-like nanoparticles (tens of nm thin) are added, they are promoted to enter the contacted area driven by the flow of lubricant. Simultaneously, their large surface area supplies more lubricant molecules in the contact area (the right of Figure 5.10b). The lubricant molecules brought by the 2D nano- additives are capable of reducing friction by inserting into the localized area and separating the contacted surfaces. Therefore, the 2D sheet-like nanoparticles-based intermolecular interaction plays a critical role in friction reduction.

5.4. Tribological performance in Cu CMP

CMP is a tribology-based processing technique widely used in microelectronic manufacturing.^{267,268} It is a hybrid of free abrasive polishing and chemical etching. High-precision fabrication in modern CMP demands for a CMP slurry containing novel abrasive particles. Many inorganic materials such as alumina,²⁶⁹ ceria,²⁷⁰ silica,²⁷¹ and diamond²⁷² have been used as abrasive particles in CMP. Each has been selected based

on their effectiveness in polishing under particular conditions. Although abrasive particles enhance the mechanical removal of surface materials, defects such as scratch and pitting might be induced due to agglomerated particles and debris. To improve energy efficiency, it is essential to utilize abrasive particles that can reduce friction while maintaining the high processing efficiency.

5.4.1. Utilization of nanosheets as slurry abrasives

To date, global planarization in CMP remains to be a major concern, particularly for patterned wafers where the metal/dielectric density differs across the wafer.²⁷³ The limitation of ion and slurry transfer is one of the key factors affecting planarization. The planarization is characterized by the within-wafer-non-uniformity (WIWNU).^{274,275} Previous studies in this regard have been focused on optimization of polishing parameters and utilization of corrosion inhibitors.²⁷⁶⁻²⁷⁹ It is always desirable to develop a slurry that improves the slurry transport and contact between the polishing pad and the wafer surface. Investigation in previous chapters has demonstrated great potential of 2D nanomaterials in tribological applications. Wear optimization in CMP process is reported here using a novel slurry containing yttrium oxide (Y_2O_3) nanosheets (NS) as abrasives. Cu film (2 μm thick) coated silicon wafers ($\text{\O} 300$ mm) were used as target substrates for the planarization evaluation here. A commercial SiO_2 -based slurry ($\text{\O} \sim 35$ nm, Fujimi Corporation) was used in comparison of planarization efficiency with a home-made slurry, which consisted of citric acid (0.01 M), BTA (0.05 wt %), H_2O_2 (3 vol %), Y_2O_3 NS abrasive (3 wt %), and DI water.

The comparison of WIWNU before and after CMP experiments in different slurries is shown in Figure 5.11. The trend in the WIWNU after CMP is indicated by the arrows in the figure. It is interesting to see that the WIWNU is reduced by 30 percent using the Y_2O_3 slurry. Using the commercial SiO_2 slurry, on the contrary, it shows an increase in the WIWNU by 48 percent. Meanwhile, the wafer polished using the Y_2O_3 slurry also has better surface quality. As shown in Figure 5.12, wafers polished using the Y_2O_3 slurry have lower arithmetic-averaged surface roughness than that polished with the SiO_2 slurry. The former is $\sim 48\%$ smaller than the later. In microelectronic devices, an important factor to planarize a wafer is elimination of Cu dishing.^{280,281} Results of Cu dishing in our CMP are shown in Figure 5.13. Wafers polished with the Y_2O_3 slurry obtained $\sim 23\%$ less Cu dishing than that polished with the SiO_2 slurry.

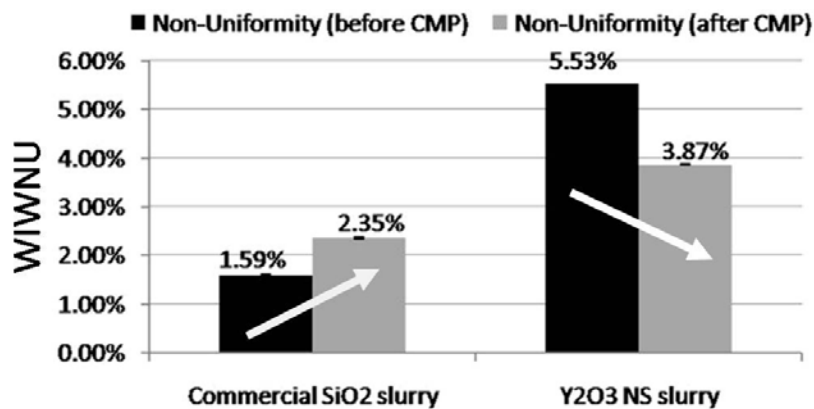


Figure 5.11. Changes of WIWNU before (black) and after (gray) CMP using different slurries.

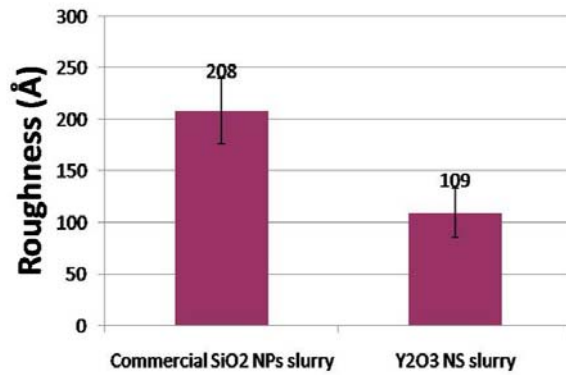


Figure 5.12. The arithmetic averaged surface roughness of wafers that are polished using different slurries.



Figure 5.13. The Cu dishing in wafers that are polished using different slurries.

Planarization is significantly improved using the 2D nano-abrasive in Cu CMP. As discussed in above, the 2D nanomaterials have unique capability in lubrication. It is indeed rational to hypothesize that the 2D sheet-like nanoparticles are able to reduce friction via modifying the CMP slurry's fluid dynamics. In order to understand the effects of abrasives on WIWNU and surface roughness, frictional and rheological investigations are conducted for the CMP slurries. The results are shown in Figures 5.14 and 5.15, respectively. In Figure 5.14, it is observed that the Y₂O₃ NS-based slurry has

lower coefficient of friction than the commercial SiO₂ slurry. In Figures 5.15a and 5.15b, it is clear that the SiO₂ slurry with higher concentration has the larger slope in shear stress-shear rate plots. With the increase in SiO₂ concentration, the slurry becomes more viscous. Viscosity is directly related to the friction and mass transfer among fluid layers.²⁸² The change in slope of the shear stress-rate plots implies movement of one fluid layer respect to another with significant mass (or momentum) transfer. This is the evidence of a turbulent flow.²⁸³ With the same concentration, the shear stress in SiO₂ slurry changes at a faster rate against the shear rate than the Y₂O₃ slurry, as shown in Figure 5.15c. It is interesting to observe in Figure 5.15d that the ratio of shear stress to shear rate in water is not affected by the addition of Y₂O₃ NS. The unchanged slope of the shear stress-rate plots indicates the movement of one fluid layer past another with little matter transfer. This is the evidence of a laminar flow.²⁸⁴ It is concluded from rheological measurements that SiO₂ NP increases the viscosity of slurries while Y₂O₃ NS shows no effects.

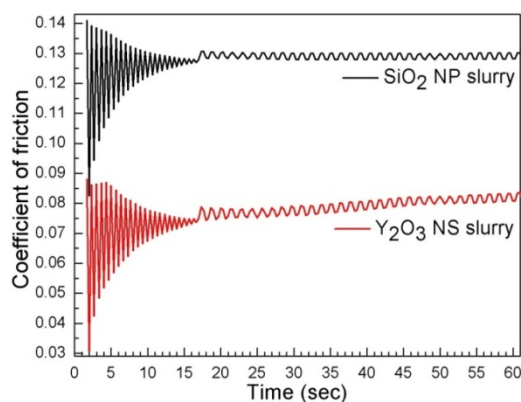


Figure 5.14. Results of friction between the Cu film and the polishing pad in SiO₂ NP (black, top) and Y₂O₃ NS (red, bottom) slurries.

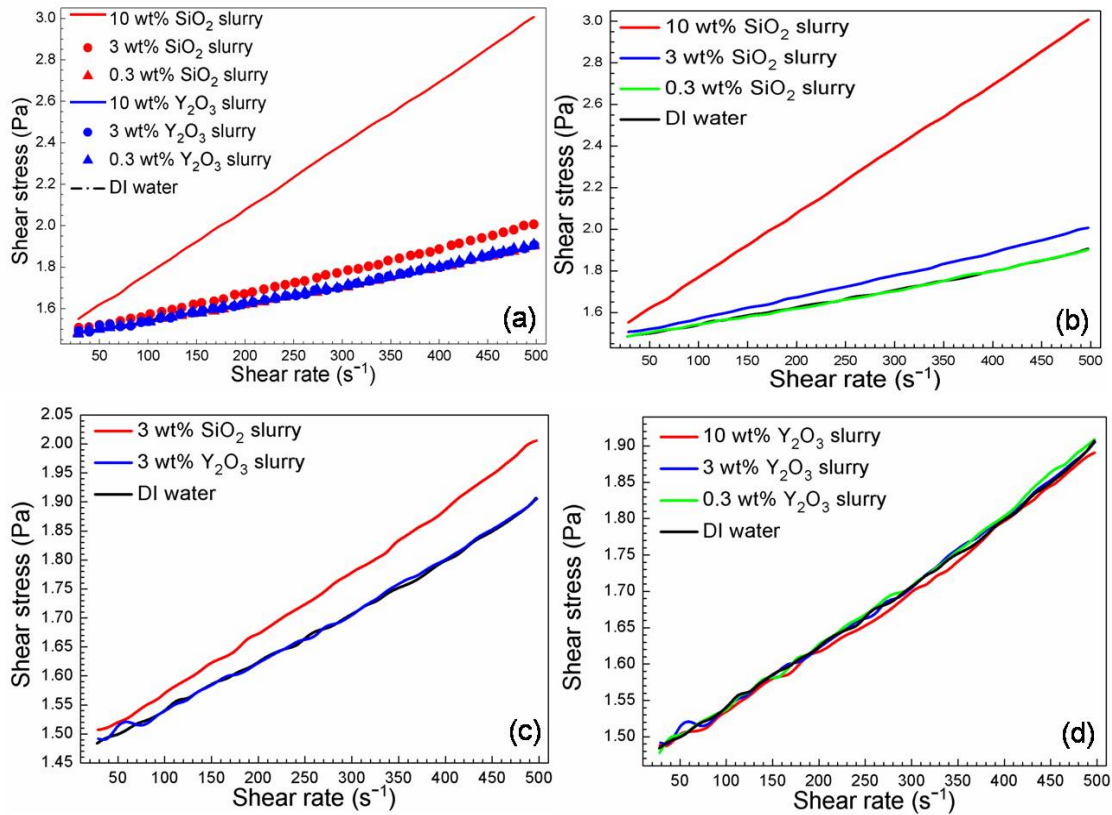


Figure 5.15. Results of rheological measurements: (a) the comparison of shear stress-shear rate plots in different slurries with different abrasive concentrations; (b) variation of shear stress to shear rate in SiO₂ NP slurries with different concentrations; (c) the clear comparison of shear stress-shear rate plots in different slurries with the same abrasive concentration (3 wt %); (d) variation of shear stress to shear rate in Y₂O₃ NS slurries with different concentrations.

Based on frictional behaviors and rheological properties of slurries, mechanisms in reduction of WIWNU are proposed in schemes illustrated in Figure 5.16. When wafer is polished using the SiO₂ slurry, spherical NP (see inset of Figure 5.16a) can embed in the wafer and abrade it through particle-wafer contact mode (Figure 5.16a).^{285,286} Such abrasion through 3-body and 2-body wear is believed to be responsible for materials

removal in CMP. On the contrary, when square Y_2O_3 NS (see inset of Figure 5.16b) is used, it enables them to have larger contact area. The increased contact leads to a uniform distribution of the down force and the reduced contact pressure. When the applied pressure is low, a fluid film will be able to form between the pad and wafer (Figure 5.16b).^{287,288} As a result, the uniformed contact and improved slurry transport lead to more effective lubrication.^{289,290} This is confirmed by the friction results. Accordingly, polishing under the lubricating condition can reduce the WIWNU after CMP.²⁹¹ In addition, when slurries entered the interface between the pad and wafer, Y_2O_3 NS can be deemed as parallel layers whereas SiO_2 NP distribute chaotically and stochastically. As demonstrated by rheological experiments (Figure 5.15), a laminar flow and a turbulent flow are believed to form in Y_2O_3 and SiO_2 slurries, respectively. A laminar slurry flow that has low viscosity with little flow fluctuation leads to uniform distributions of relative velocity and abrasive movement trajectories.^{274,292} In such the WIWNU is decreased.

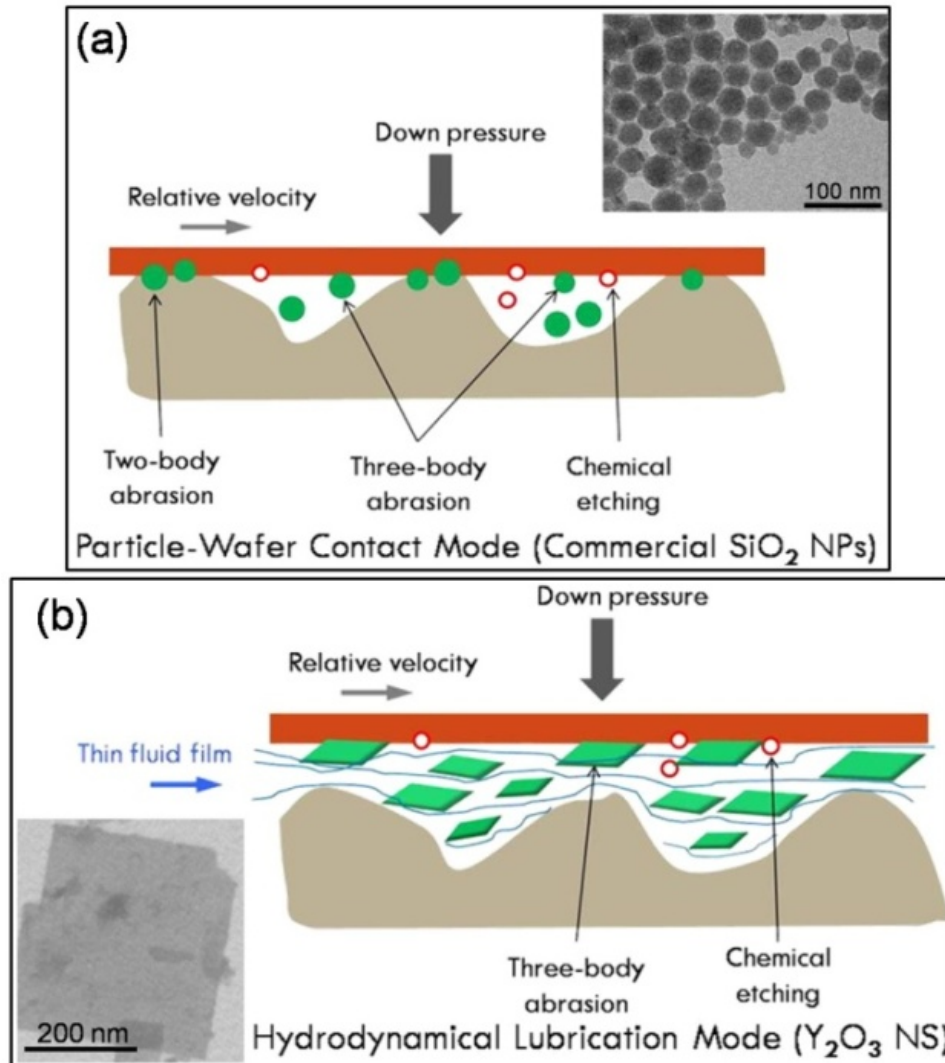


Figure 5.16. Schematic representations of abrasion modes using the commercial SiO_2 NP (inset) slurry (a) and the Y_2O_3 NS (inset) slurry (b).

It is also noted that the protruded areas are polished during the CMP, while the low areas are passivated resulting in a smooth surface.^{285,286} Localized pad deformation occurs and has been reported to be an important reason causing metal dishing.^{280,293,294} In the current work, however, Y_2O_3 NS has larger contact area than SiO_2 NP. The down

force distributes uniformly in the contact area. The low area undertakes a comparable pressure to that protruded area experiences. A uniform pressure distribution is beneficial for reduction in dishing.²⁸⁰ In addition, dishing can be reduced through gentle contacts of pad through Y_2O_3 NS to wafer, which is similar to soft landing in abrasive free polishing.²⁹⁵⁻²⁹⁷ Therefore, the CMP conducted using the Y_2O_3 NS-based slurry obtains little Cu dishing.

5.4.2. Utilization of B- B_2O_3 composite nanoparticles as slurry abrasives

Boron compounds have been used as abrasives in sandblasting nozzles,^{298,299} while 2D nanostructured B_2O_3 is widely known as an excellent solid lubricant.^{168,257,258} Due to the unique properties of abrasion and lubrication, B- B_2O_3 composite nanoparticles (NP) can be new promising candidates for CMP slurry abrasive. Tribological application of the B- B_2O_3 NP (sized ~ 5 nm)-based slurry is explored here. The detailed information about synthesis and characterization of the B- B_2O_3 NP can be found in Chapter III. The CMP slurry contains the following additives; silica (SiO_2) and/or B- B_2O_3 NP as abrasives, H_2O_2 as an oxidizer, citric acid as a complexing agent, and benzotriazole (BTA) as a corrosion inhibitor. During polishing, the oxidizer reacts with Cu and forms porous copper oxide which can be easily removed through friction between wafer, pad, and abrasives. Citric acid is able to increase Cu dissolution and material removal rate. Since excessive addition of the complexing agent can cause more Cu dissolution which leads to poor surface roughness and planarization, the component that can provide controllability of removal rate is required.^{300,301} The inhibitor BTA was

used to suppress Cu dissolution. The copper oxide complexed with citric acid plays the role of protective layer in the recessed area and an opposite role of sacrificial layer in the protruded area, where peak material can be removed by mechanical action induced through the pad and abrasive particles. With these slurry components, CMP experiment was performed on Cu wafers which have five pyramidal micro-indent ($\sim 1 \mu\text{m}$ deep) on each surface (see Figure 5.17). The line of micro-indent was parallel to the edge of squared Cu-Si wafer and 5 mm away from it. The distance between each micro-indent was 0.5 mm. Three different abrasives were measured in CMP: 1). 3 wt % SiO_2 NP (sized $\sim 35 \text{ nm}$) abrasive; 2). 0.05 wt % $\text{B-B}_2\text{O}_3$ NP abrasive; and 3). 3 wt % SiO_2 NP-based abrasive containing 1 wt % $\text{B-B}_2\text{O}_3$ NP.

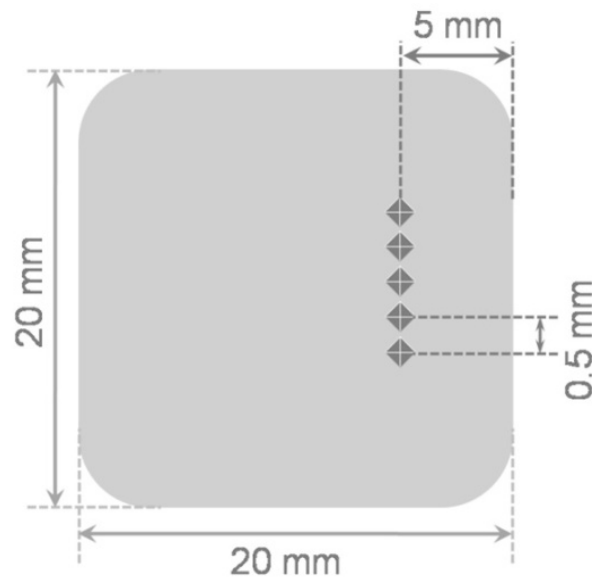


Figure 5.17. Five pyramidal micro-indentations on the Cu-coated Si wafers prepared for CMP.

The height-removal rates can be calculated through measuring the dimension of micro-indentations before and after CMP. Using an atomic force microscope (AFM), the average depths of micro-indentations could be measured by the height differences between the lowest point inside the indentations and the flat surface around them after leveling. AFM images around the indent and rest area of the Cu surface before and after CMP are shown in Figure 5.18. The less the micro-indent depth is, the higher the height-removal rate would be. Results are shown in Figure 5.19, from which height-removal rate can be calculated (Figure 5.20). Using pure B-B₂O₃ NP abrasive, the height-removal rate is increased by ~ 13 %, even with a minimum abrasive concentration (0.05 wt %). Using the 3 wt % SiO₂ NP-based abrasive containing 1 wt % B-B₂O₃ NP, the highest material-removal rate is obtained, which is improved by ~ 32 %.

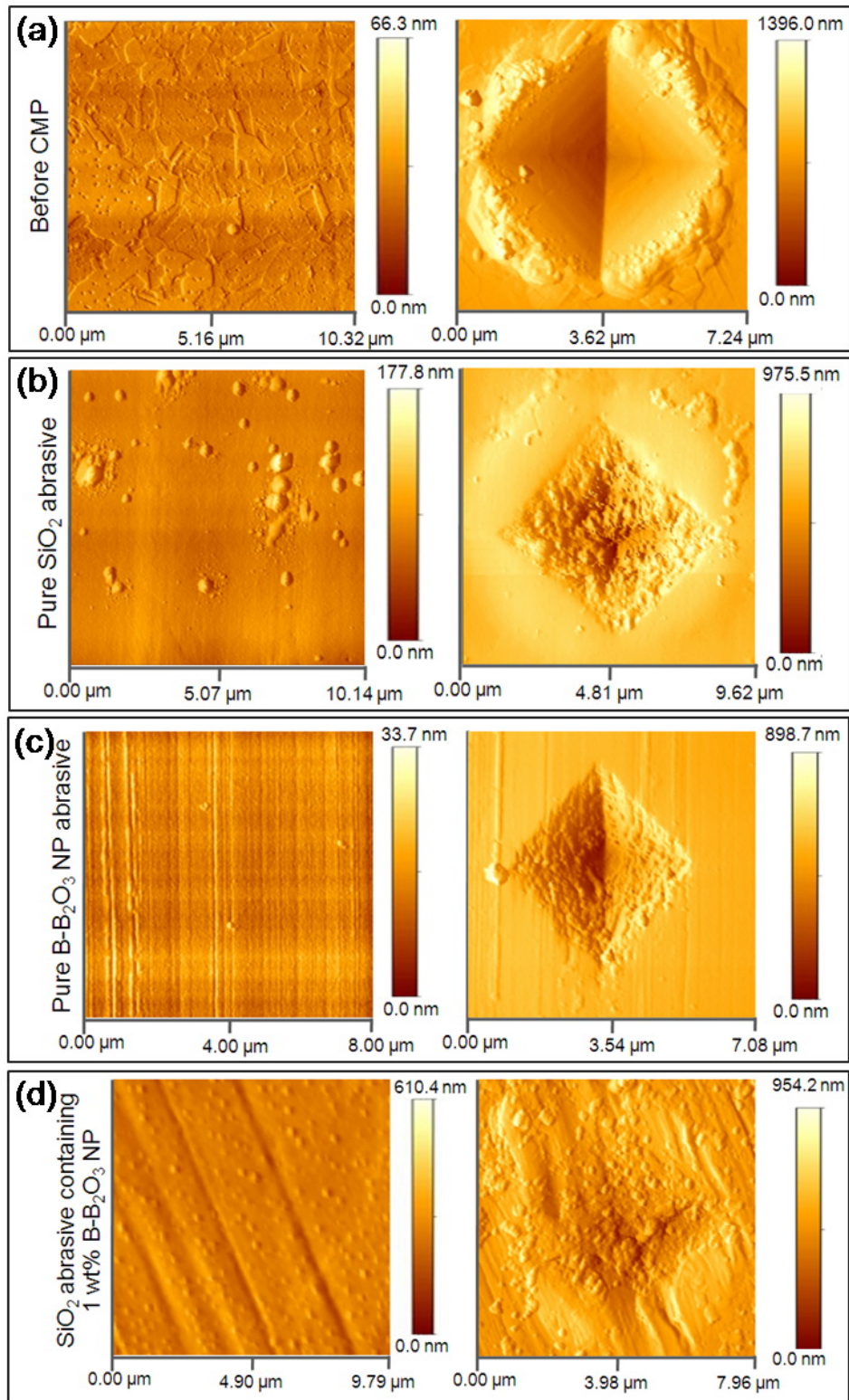


Figure 5.18. AFM images before and after CMP in different slurries (as labeled).

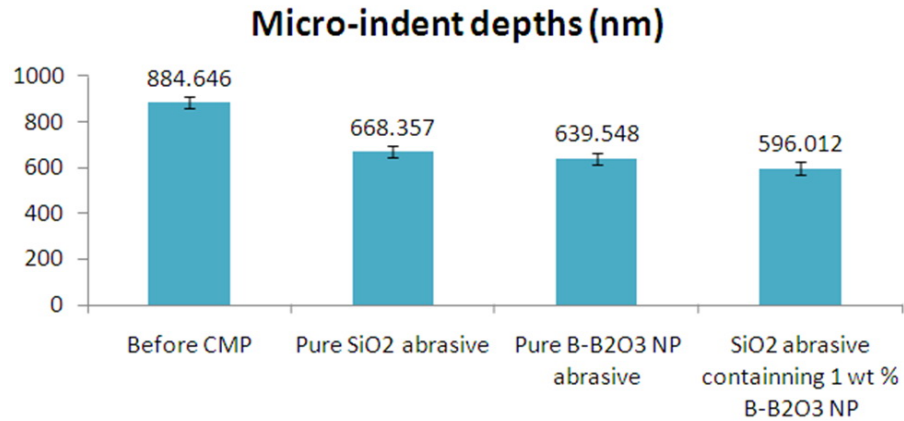


Figure 5.19. Averaged micro-indent depth on Cu films before and after CMP in different slurries.

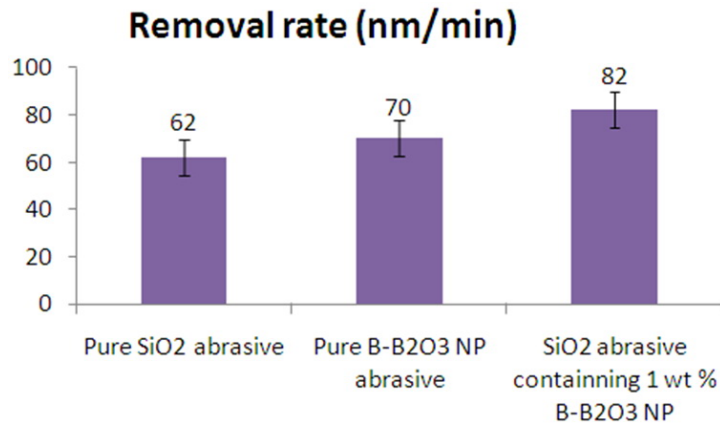


Figure 5.20. Comparison of materials removal rate using different CMP slurries.

During polishing, the contacted area between the Cu wafer and abrasive particles increases by adding smaller B-B₂O₃ NP (~5 nm). In addition, the surface chemistry of nanoparticles is largely dependent on their sizes, i.e., the smaller the particle, the more reactive the particle.^{302,303} Such will further enhance the interfacial interaction between wafer and nanoparticles.^{304,305} As a result, an increase in the height reduction, i.e., removal rate, is obtained. Another possible reason for the increased removal rate is the

electrostatic interaction between B-B₂O₃ NP and the Cu surface. The relationship between the interaction (electrostatic) force and removal rate has been reported.^{306,307} The H₂O₂ oxidizes Cu surface, and positively charged copper oxide surface is formed.^{308,309} The zeta potentials of SiO₂ NP and B-B₂O₃ NP are negative in the acidic environment of our CMP experiment.³¹⁰ During the CMP, the oxidized Cu surface and the abrasive particles would attract each other electrostatically due to their oppositely charging states. This is believed to assist an increase in material-removal rate during CMP as well.

In order to avoid generation of defects and obtain a smooth surface, low coefficient of friction during CMP is highly desirable. 2D nanostructured B₂O₃ surface on the B-B₂O₃ NP enables the CMP process to undergo smoothly. The novel composited NP-based slurry leads to an improved surface after CMP. Figure 5.21 shows friction results during the CMP experiment. In the absence of abrasive particles, the coefficient of friction is visibly higher, as shown in the top black line in Figure 5.21. It is well known that silica is able to work as a lubricant when hydrated.^{311,312} The addition of silica hence apparently reduces the friction coefficient by ~ 10 % (see middle red line in Figure 5.21). The boron based additives, such as boron, boron oxide, and boron acid, have been used to eliminate friction in various applications.^{234,313,314} In the present research, both slurries, containing pure B-B₂O₃ NP as abrasives and SiO₂ NP-based abrasive containing 1 wt % B-B₂O₃ NP, decrease the friction coefficient further, as shown in the bottom (blue and green) lines in Figure 5.21. In the presence of B-B₂O₃ NP, the maximum friction reduction that can be calculated from Figure 5.21 is by ~ 28 %.

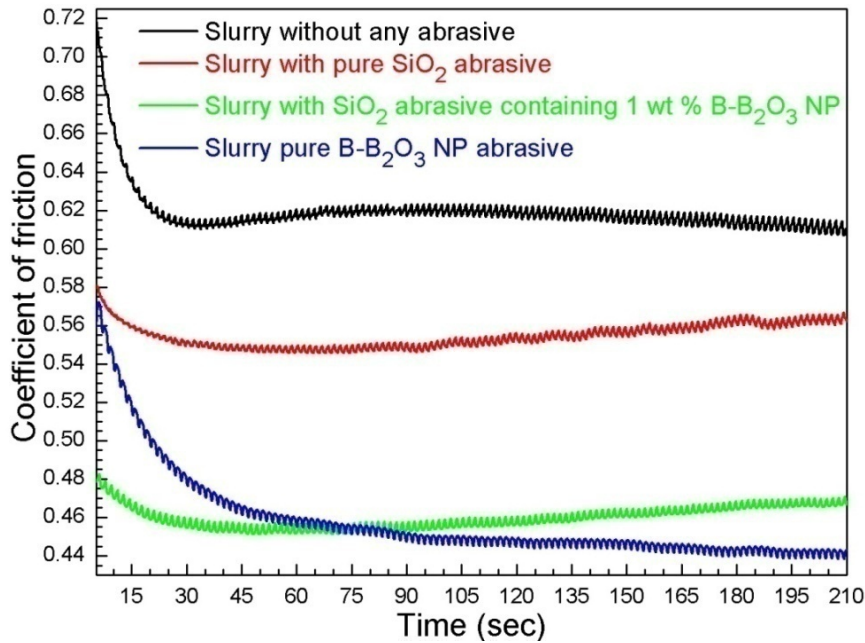


Figure 5.21. Comparison of coefficient of friction for CMP experiments conducted in different slurries.

Transmission electron microscope (TEM) images of B-B₂O₃ NP before and after CMP experiment are shown in the left of Figure 5.22. Different sized NP imaged here to show the oxidized surface (B₂O₃) clearly. After CMP, the B₂O₃ surface is removed, while the decrease in size of B-B₂O₃ NP is observed. When the B-B₂O₃ NP abrades the Cu surface in a water solution, boric acid (H₃BO₃) can be spontaneously generated from the B₂O₃ (see reactions shown in Figure 5.22). The H₃BO₃ has a 2D nanostructured-layered structures (see the right of Figure 5.22). It thus can be used to reduce friction in humid atmosphere.^{168,258} During the CMP, the B-B₂O₃ NP shows promising in improving the lubricating property due to the unique 2D nanostructured surface.

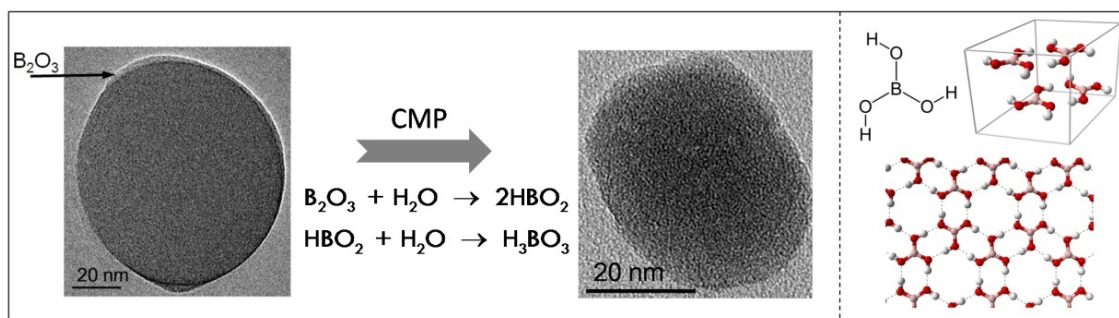


Figure 5.22. 2D nanostructured B_2O_3 -induced surface improvement during CMP (left); layered nanostructure of B_2O_3 (right).

The 2D nanostructured surface of B- B_2O_3 NP makes the CMP efficiency improve. From AFM images shown in Figure 5.18, it is observed that CMP increases the flatness of Cu surface (Figure 5.18b). Addition of B- B_2O_3 NP into SiO_2 NP-based slurry results in an increased uniformity and cleanness for Cu surface (Figure 5.18d). The surface polished using the pure B- B_2O_3 NP displays the best quality, from which a uniform and clean surface is obtained (Figure 5.18c). Accordingly, measurement of surface roughness after CMP confirms the improved surface quality. Results are shown in Figure 5.23. The surface roughness, arithmetic average (R_a) and root mean-square-average (R_q), are obtained using the AFM. It is seen that utilization of B- B_2O_3 NP as abrasive provides a visibly smoother polished surface than that polished with pure SiO_2 NP-based slurry. In the presence of B- B_2O_3 NP, the surface roughness is reduced maximally by $\sim 58\%$ and $\sim 72\%$ for R_a and R_q , respectively. Therefore, the B- B_2O_3 NP-based abrasives improve CMP performance by increasing the materials-removal rate and enhancing the lubricating performance. After CMP, the optimized planarization efficiency and the

increased surface quality are believed to be caused by the 2D nanostructured surface on B-B₂O₃ NP.

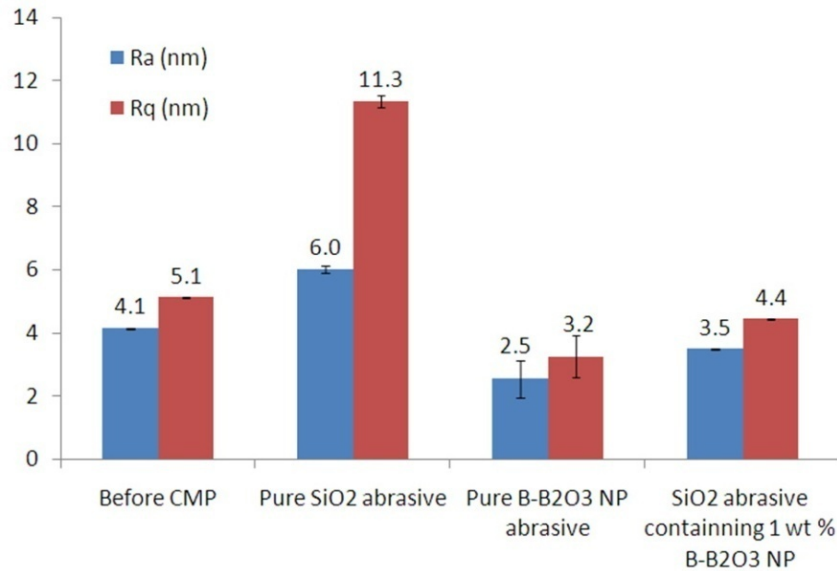


Figure 5.23. Surface roughness on Cu films before and after CMP in different slurries.

5.5. Summary

This chapter discussed effects of 2D nanomaterials on friction in liquid lubricants. Firstly, morphology of the nanomaterials additives was found to be important for the friction reduction. Only the 2D nano-additives showed capability in reducing friction. Secondly, a critical concentration was observed, below which the friction was reduced. Thirdly, the 2D nano-additives showed friction reduction no matter how the friction changed with experimental parameters. Lastly, the friction reduction was found to be partially responsible by the intermolecular interaction between lubricant molecules and additive. The friction discussed here was mainly caused by the localized asperity-

contact. The 2D nanomaterials could enter the localized contact area driven by the lubricant flow. The intermolecular interaction enabled them to deliver lubricant molecules into the contact area and reduce the friction.

Further efforts in identifying applications of the nanomaterials were made, and two case studies were discussed here. The first case was to use the Y_2O_3 nanosheet as slurry abrasives for Cu CMP. The low-friction process using the Y_2O_3 nanosheet showed reduction of surface non-uniformity, decrease in roughness, and elimination of Cu dishing. The second was to enhance the lubrication performance during the CMP using the B- B_2O_3 nanoparticles. Results showed that the nanoparticles are able to significantly reduce the surface roughness while increasing the materials-removal rate. This was due to the low-friction CMP process resulting from its 2D nanostructured oxide surface.

Tribological evaluation in the present chapter reveals great potential of the 2D nanomaterials as additives in fluidic lubrication. Mechanisms for this will be analyzed and addressed in the next chapter by conducting rheological investigations.

CHAPTER VI

VISCOSITY MODIFICATION USING 2D NANO-ADDITIVES[‡]

This chapter discusses the non-Einstein-like viscosity reduction using 2D nanoparticles in a fluidic lubricant. It includes the following section: 1) analyses of the Stribeck curves of lubricants containing 2D nanomaterial; 2) non-Einstein-like viscosity reduction using 2D nanoparticles; 3) relationships between structure and fluid-lubricants. Fluid mechanics, viscous flow analysis, and computational simulation were carried out and it was discovered that inclination of the 2D nano-additives was responsible for the viscosity reduction.

6.1. Effects of 2D nano-additives on lubricating performance

6.1.1. Evaluation via Stribeck curves

How the lubrication regimes respond to friction can be reflected through plotting Stribeck curves.^{260,261} Stribeck curves were originally designed for differentiating the lubrication regimes. The friction coefficient is plotted against the Sommerfeld number, a ration of viscosity and velocity to applied load.^{315,316} A Stribeck curve is shown in Figure 6.1a with three basic lubrication regimes: 1) boundary lubrication (regime I, with very high friction); 2) mixed lubrication (regime II, experiencing continuous decrease of

[‡] Part of this chapter reproduced with permission from “ α -zirconium phosphate nanoplatelets as lubricant additives” by Xingliang He, et al., *Colloids Surf., A*, **2014**, 452, 32-38 (Copyright © 2014, Elsevier) and “Two-dimensional nanostructured Y₂O₃ particles for viscosity modification” by Xingliang He, et al., *Appl. Phys. Lett.*, **2014**, 104, 163107 (Copyright © 2014, AIP Publishing LLC).

friction); and 3) hydrodynamic lubrication (regime III, with stable and low friction). In the boundary lubrication two surfaces are mostly in contact with each other (the left inset of Figure 6.1a) when load is high and viscosity and speed are low. Characteristics of boundary lubrication are high friction (see top black plot in Figure 6.1b), large surface contact, and little fluid between two surfaces. As the load decreases, or the viscosity and speed increase, a fluid film forms while the surfaces are separated. The film begins to support load, even though it is still very thin (the middle inset of Figure 6.1a). A steep drop in friction is often observed on the Stribeck curve when reaching the mixed lubrication regime. The surfaces are lifted more with increased viscosity and speed, or with a decreased load. A transition from mixed lubrication to hydrodynamic lubrication is obtained when the minimum friction is observed on the Stribeck curve (see bottom green plot in Figure 6.1b). In the hydrodynamic-lubrication regime, two surfaces are completely separated by a fluid film (the right inset of Figure 6.1a). More loads can be applied to the thicker fluid film, and a relatively low and stable friction coefficient is obtained (see middle red plot in Figure 6.1b). Due to fluid drag, the friction increases slightly in the later stage.

In order to understand the effects of 2D nanomaterials on lubrication, the average coefficient of friction is used in plotting Stribeck curves (Figures 6.2). Those curves obtained from testing yttrium oxide (Y_2O_3) nanosheets (NS) and α -zirconium phosphate (ZrP) nanoplatelets. As shown in Figure 6.2, standard deviation of the average value is used to label the error. The lubrication experiments discussed in this chapter were all

conducted using a pin-on-disk configuration consisting of a rotating glass disk and a fixed E52100 alloy steel pin.

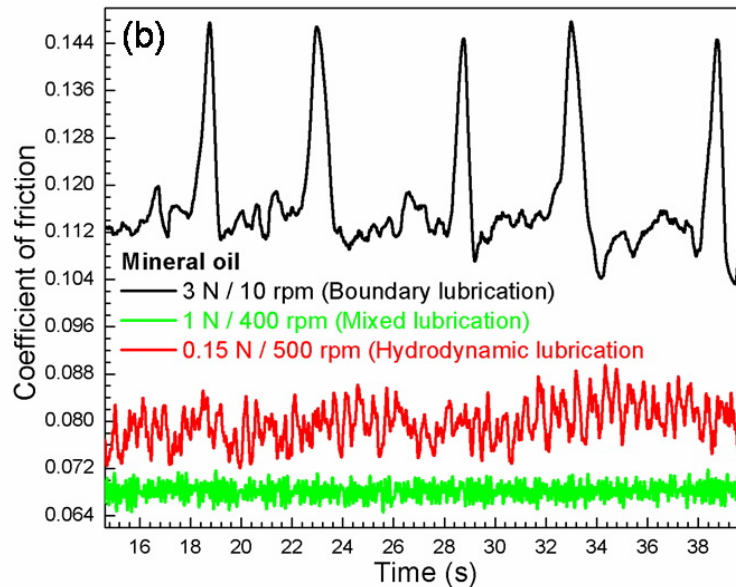
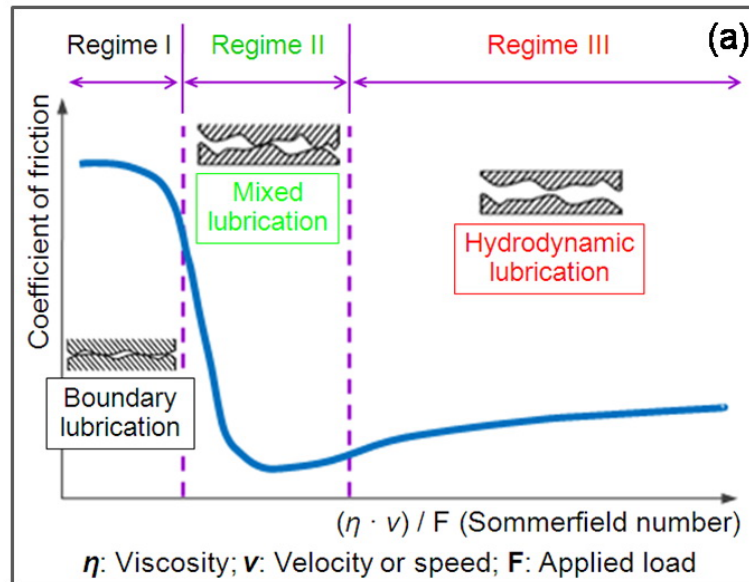


Figure 6.1. (a) A Stribeck curve with different lubrication regimes schematically showing in inset; (b) Example comparison of friction coefficient in different lubricant regimes using mineral oils; the applied loads and the rotational speeds used in the experiments are labeled in the figure.

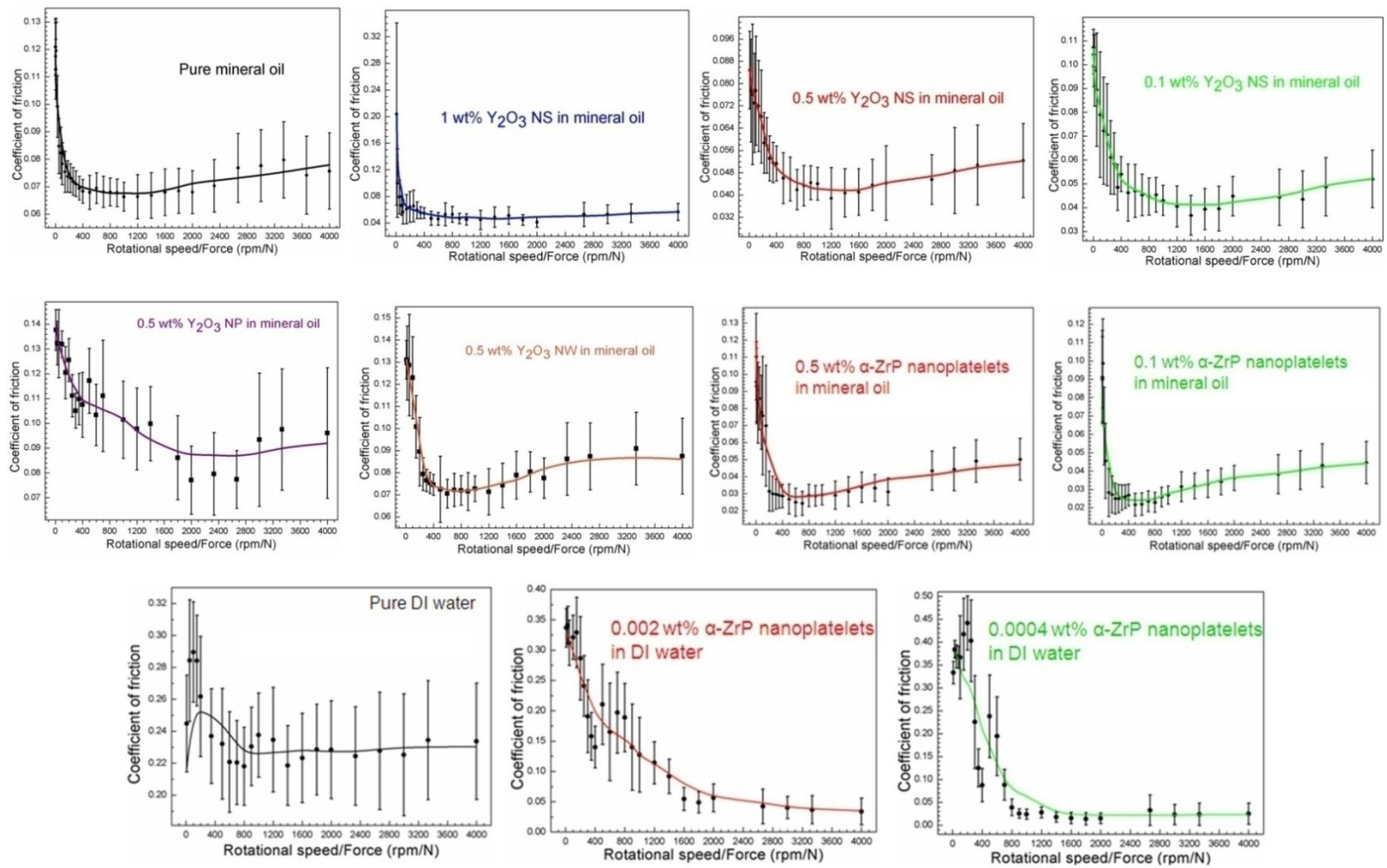


Figure 6.2. Plotting Stribeck curves of different lubricants using the average coefficient of friction.

6.1.2. Lubricating behavior of 2D nanomaterials

The effectiveness of 2D Y_2O_3 NS as additives in a mineral oil is shown in Figure 6.3. In Figure 6.3a, both Y_2O_3 nanoparticles (NP, purple line) and nanowires (NW, orange line) additives lead to the increase in coefficient of friction. On the contrary, Y_2O_3 NS (green line) additive drops the coefficient of friction significantly. At the same low concentration (0.5 wt %), presence of the Y_2O_3 NP and NW in the mineral oil deteriorates its lubricating performance. Only Y_2O_3 NS is capable of enhancing lubrication of mineral oil as an effective additive. Lubricating performances of mineral oil containing different concentrations (1 wt %, 0.5 wt %, and 0.1 wt %) of Y_2O_3 NS are examined in Figure 6.3b as well. The low concentration of Y_2O_3 NS additives leads to reduction in friction. At a concentration of 0.1 wt %, the Y_2O_3 NS additive decreases the coefficient of friction as much as by ~ 40 %. A small amount of Y_2O_3 NS additive is enough to greatly improve lubricating performance in all regimes, from the boundary-lubrication regime (I) to hydrodynamic-lubrication regime (III). For the lubricant with relatively high concentration (1 wt %), a poor lubricating performance is observed in boundary lubrication (blue plot in regime I in Figure 6.3b), which displays visibly higher coefficient of friction than that of pure mineral oil. This could be due to agglomeration of Y_2O_3 NS under the high load and low rotational speed in the boundary-lubrication regime.³¹⁷ The fluid film of the mineral oil would be blocked as the excessive Y_2O_3 NS piled up (the left of Figure 6.4). Direct contact between the Y_2O_3 nanosheets results in a noticeable frictional drag. When the rotation speeds up and the load decreases, the agglomerated particles would be dispersed by the fluid shear (the right of Figure 6.4).

Once the lubrication becomes mixed or hydrodynamic, the Y_2O_3 NS additives improve the lubricating performance via modifying the fluid behavior.

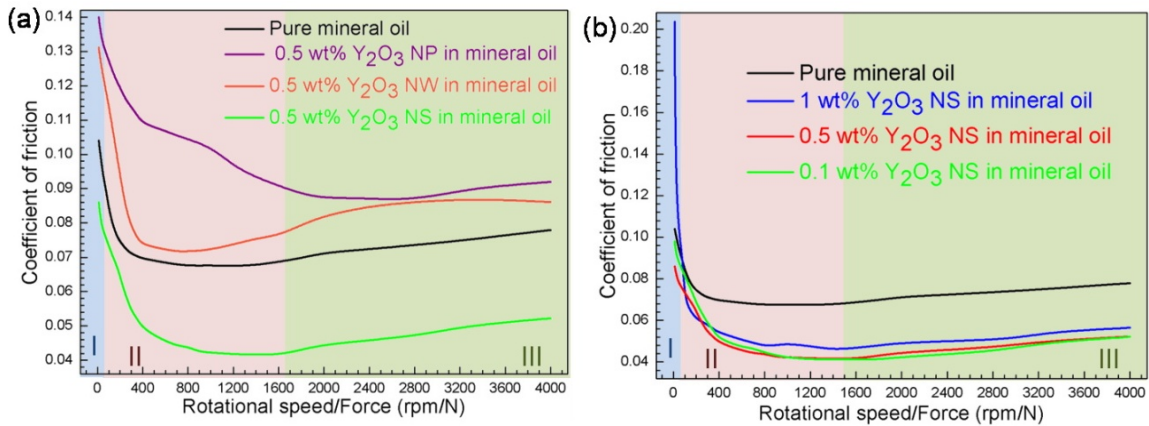


Figure 6.3. (a) Comparison of Stribeck curves using mineral oils without (black curve) and with different types (colored curves) of Y_2O_3 nano-additives (0.5 wt %). (b) Comparison of friction coefficient using mineral oils without (black curve) and with different concentrations (colored curves) of Y_2O_3 NS additives.

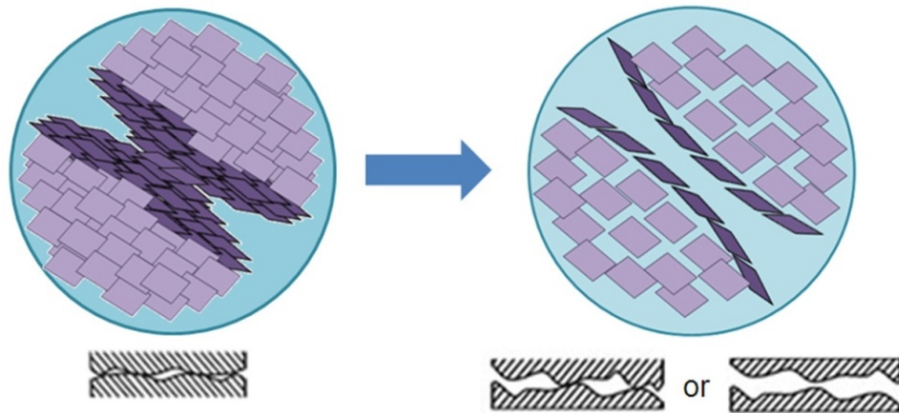


Figure 6.4. Diagram schematically showing the transition from boundary-lubrication regime to mixed- or hydrodynamic-lubrication regime with relatively high concentration (1 wt %) of Y_2O_3 NS additives.

The similar effects of α -ZrP nanoplatelets in mineral oil are found and shown in Figure 6.5a. It is observed that the addition of 0.5 wt % and 0.1 wt % α -ZrP nanoplatelets, the friction coefficient is reduced significantly in ranges from boundary-lubrication regime I, to mixed-lubrication regime II, and through hydrodynamic-lubrication regime III. The mineral oil containing 0.1 wt % of α -ZrP nanoplatelets shows slightly lower friction coefficient than that contains 0.5 wt % of α -ZrP nanoplatelets. In addition, friction in water is reduced in the presence of α -ZrP nanoplatelets additives as well (Figure 6.5b). A lower concentration of α -ZrP nanoplatelets leads to further decrease in coefficient of friction. It is observed from Figure 6.5 that addition of 0.1 wt% α -ZrP nanoplatelets in mineral oil and in water reduced friction maximally by 65 % and 90 %, respectively.

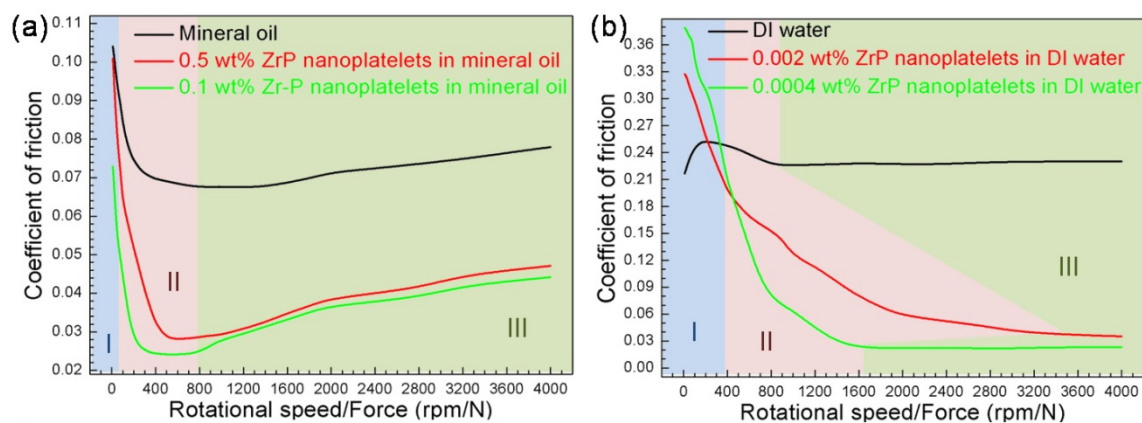


Figure 6.5. (a) Comparison of Stribeck curves using mineral oils without (black curve) and with different concentrations (colored curves) of α -ZrP nanoplatelet additives. (b) Comparison of Stribeck curves using DI water without (black curve) and with different concentrations (colored curves) of α -ZrP nanoplatelet additives.

6.2. Non-Einstein-like reduction of viscosity

To further understand the effects of 2D nano-additives on lubricating behavior, we examined the viscosity of the fluidic lubricants. According to Reynolds' theory, once a continued lubricant film is formed between two bodies in relative motion, a hydrodynamic pressure is built up to separate the two surfaces.^{318,319} The viscosity of a fluid reflects its load-carrying capability, which determinates the thickness and performance of a lubricant film.

6.2.1. Viscosity modification using 2D nano-additives

The viscosity against shear rate was measured, as shown in Figures 6.6 and 6.7. Figure 6.6a shows that Y_2O_3 NP and NW additives result in viscosity increase of the mineral oil (purple and orange curves). The Y_2O_3 NP and NW additives make the mineral oil fluid not flow easily. This is because that high shear stress is needed to drive the lubricant flow in which Y_2O_3 NP and NW are randomly dispersed. Oppositely, after Y_2O_3 NS are added into the mineral oil, a lower viscosity is obtained (green curve in Figure 6.6a). By decreasing the concentration of the Y_2O_3 NS, the viscosity was reduced further (Figure 6.6b). At the concentration of 0.1 wt %, Y_2O_3 NS could reduce the viscosity as much as by ~ 4 %. Figure 6.7 shows the similar results based on the α -ZrP nanoplatelets additives in non-aqueous and aqueous lubricants. The most reduction of viscosity was achieved at the lowest concentration (0.1 wt %) of α -ZrP nanoplatelets, i.e, by ~ 3 % in mineral oil (Figure 6.7a) and by ~ 12 % in water (Figure 6.7b). Therefore, well corresponding to the results based on Stribeck curves (Figures 6.3 and 6.5), a low

viscosity is obtained once the 2D sheet-like nano-additives are added into the lubricants, which implies that they have the capability to improve lubrication via modification of the lubricants' rheological property.

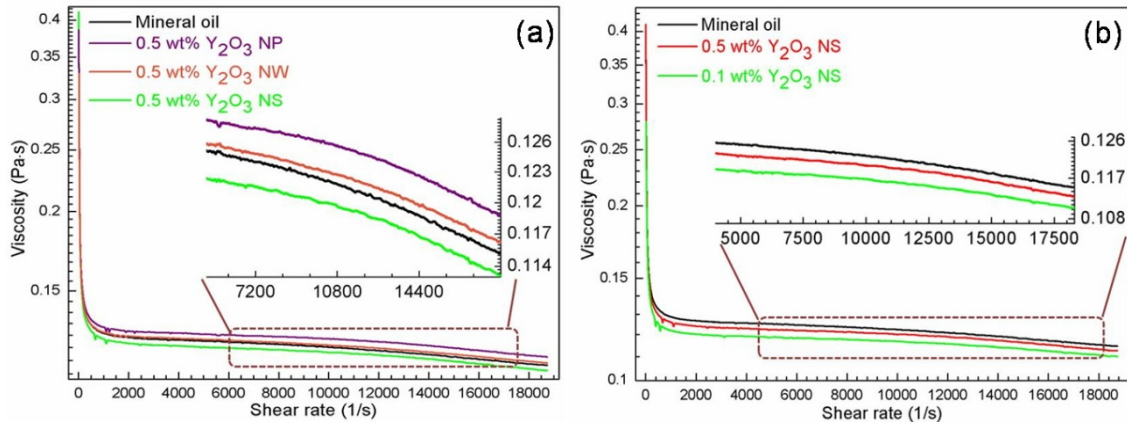


Figure 6.6. (a) Variation of viscosity with shear rate in mineral oil (top black plot), and with addition of different types (colored curves) of Y_2O_3 nano-additives (0.5 wt %). (b) Variation of viscosity with shear rate in mineral oil (top black plot), and with addition of 0.5 wt % (middle red plot) and 0.1 wt % (bottom green plot) Y_2O_3 NS additives.

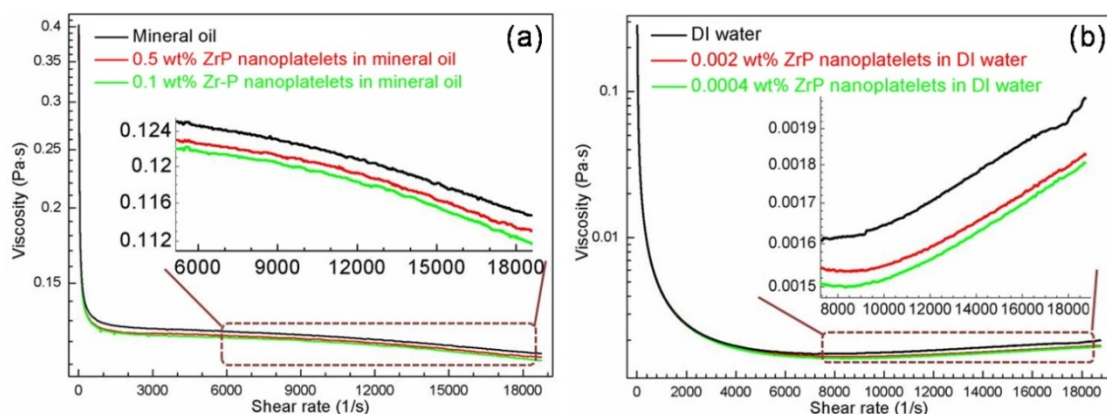


Figure 6.7. (a) Variation of viscosity with shear rate in mineral oil (top black plot), and with addition of 0.5 wt % (middle red plot) and 0.1 wt % (bottom green plot) α -ZrP nanoplatelet additives. (b) Variation of viscosity with shear rate in DI water (top black plot), and with addition of 0.002 wt % (middle red plot) and 0.0004 wt % (bottom green plot) α -ZrP nanoplatelet additives.

6.2.2. Thixotropic study

From Figures 6.6 and 6.7, the viscosity reduction with increasing shear rate is observed as well, indicating the shear thinning characteristic of the lubricants.³²⁰ To further understand this phenomenon, a thixotropic study was conducted to investigate the shear thinning properties of the liquid lubricants with the 2D nanostructured additives. The results are shown in Figure 6.8. In mineral oil, the fluid structure is deconstructed initially by applying a constant shear rate ($10,000 \text{ s}^{-1}$), leading to the quick drop of viscosity at the beginning ($< 60 \text{ s}$, Figures 6.8a and 6.8b). As mineral oil is mainly composed of long-chain alkane molecules, the physical interactions between them enable the deconstructed structure to rebuild continuously. The process that breaks the molecular structures competes with that rebuilds the molecular bonding. The dynamic balance between them results in a relatively stable viscosity at later stage ($> 60 \text{ s}$,

Figures 6.8a and 6.8b). In the case of water, its viscosity keeps decreasing under a constant shear rate ($10,000 \text{ s}^{-1}$, see Figure 6.8c). This indicates that the aqueous fluid structure undergoes an irreversible shearing process.

From Figure 6.8a, Y_2O_3 NS additives are found to reduce viscosity in the thixotropic study. Under the constant shear rate ($10,000 \text{ s}^{-1}$), the 0.1 wt % Y_2O_3 NS reduces the viscosity by $\sim 4 \%$, which is more than that of 0.5 wt % Y_2O_3 NS. As seen in Figures 6.8b and 6.8c, under the same shear rate, the α -ZrP nanoplatelets additive reduces viscosity as much as by 7 % for mineral oil (Figure 6.8b) and by 14 % for DI water (Figure 6.8c), respectively. It is noted that the classic Einstein theory could be used to explain linear increase in viscosity of the suspension with low-concentration particulate additives.³²¹⁻³²³ Einstein's theory permits the viscosity of a suspension to increase with the addition of particulates, while recent studies showed that the viscosity was made to decrease with addition of organic nanoparticles only.^{55,324-326} Interestingly in the present work, suspension of inorganic 2D nanomaterials in liquid lubricants is found to show a novel non-Einstein-like viscosity reduction. The 2D nano-additives-induced lubrication improvement is believed to be a consequence of the non-Einstein-like viscosity reduction.

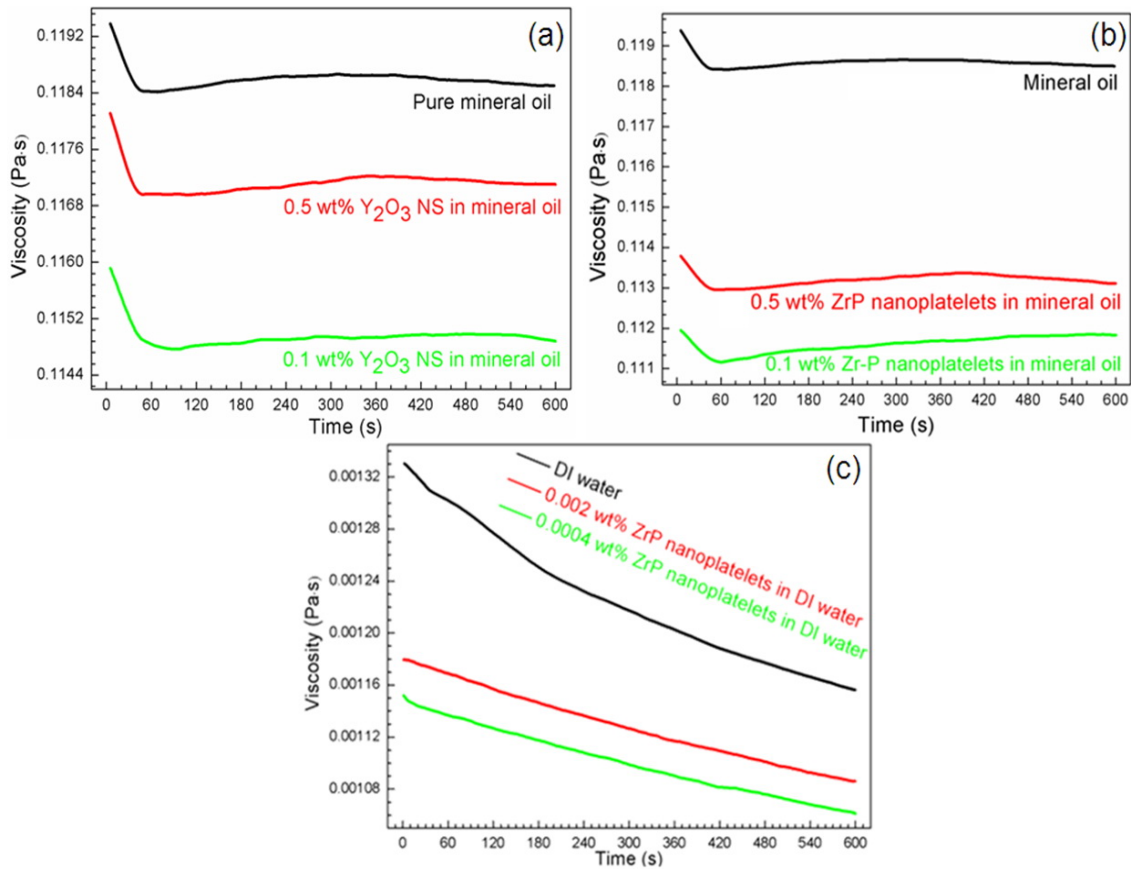


Figure 6.8. Under a constant shear rate ($10,000 \text{ s}^{-1}$), (a) reduction in viscosity of mineral oil (top black plot) in the presence of Y_2O_3 NS with concentrations of 0.5 wt % (middle red plot) and 0.1 wt % (bottom green plot); (b) reduction in viscosity of mineral oil (top black plot) in the presence of α -ZrP nanoplatelets with concentrations of 0.5 wt % (middle red plot) and 0.1 wt % (bottom green plot); (c) reduction in viscosity of DI water (top black plot) in the presence of α -ZrP nanoplatelets with concentrations of 0.002 wt % (middle red plot) and 0.0004 wt % (bottom green plot).

6.3. Mechanisms

In order to investigate the mechanisms of fluidic modification, analyses based on fluid mechanics are carried out.

6.3.1. Fluid mechanics calculation

Fluid motions of lubricants are investigated and calculated. As shown in equation (6.1), a fluid element is in a dynamic equilibrium status between surface forces, body forces, and inertia forces.^{260,261,327,328}

$$\text{Surface forces} + \text{Body forces} = \text{Inertia forces} \quad (6.1)$$

1) Surface forces

Surface stresses acting on a fluid element are shown in Figure 6.9. τ denotes the shear stresses, and σ designates the normal stresses. The shear stress can be expressed in equations (6.2). The first and the second subscripts represent the perpendicular and shear directions, respectively.

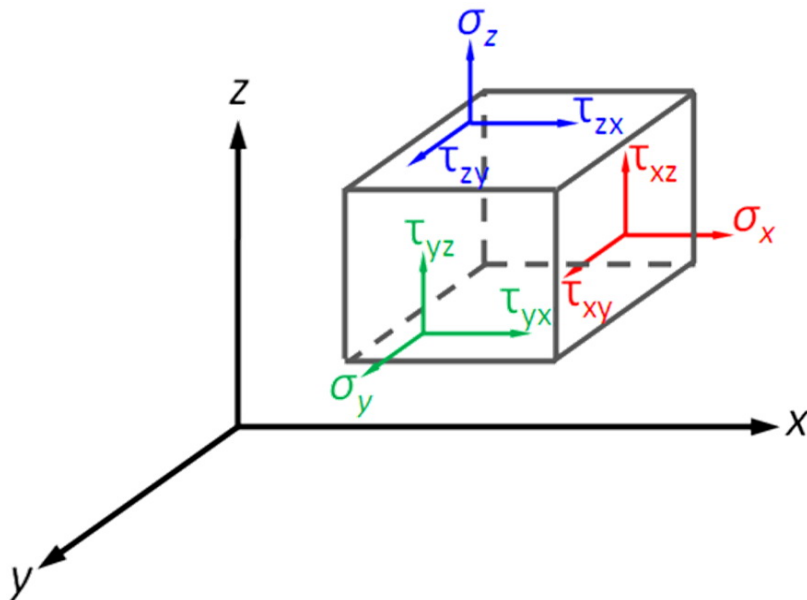


Figure 6.9. Designating surface stresses on a fluid element.

$$\tau_{ij} = \eta \left(\frac{\partial u_i}{\partial x_j} + \frac{\partial u_j}{\partial x_i} \right) \quad (6.2)$$

η = averaged viscosity across the lubricant film, Pa • s

x_i = coordinator vectors, m ($x_i = x$; $x_j = y$; $x_k = z$)

u_i = velocity vectors, m / s ($u_i = u$; $u_j = v$; $u_k = w$)

The shear stresses are symmetric [the equation (6.3)], due to that the moments are in equilibrium in the fluid element.

$$\tau_{xy} = \tau_{yx}; \quad \tau_{xz} = \tau_{zx}; \quad \tau_{yz} = \tau_{zy} \quad (6.3)$$

Simultaneously, the normal stress is written as shown in the equation (6.4):

$$\sigma_i = -P - \frac{2}{3}\eta \left(\frac{\partial u}{\partial x} + \frac{\partial v}{\partial y} + \frac{\partial w}{\partial z} \right) + 2\eta \frac{\partial u_i}{\partial x_i} \quad (6.4)$$

P = pressure, Pa

x_i = coordinator vectors, m ($x_i = x$; $x_j = y$; $x_k = z$)

u_i = velocity vectors, m / s ($u_i = u$; $u_j = v$; $u_k = w$)

The fluid element moves in the x, y, and z directions, driven together by the shear stress [F_s , the equation (6.5)] and normal stress [F_N , the equation (6.6)].

$$F_s = \frac{\partial \tau_{ij}}{\partial x_j} dx dy dz \quad (6.5)$$

$$F_N = \frac{\partial \sigma_i}{\partial x_i} dx dy dz \quad (6.6)$$

2) Body forces

A body force is the force that acts throughout the volume of the fluid element.

Such forces can be expressed in the equation (6.7):

$$F_{Bx} = X_a \rho dx dy dz \quad F_{By} = Y_a \rho dx dy dz \quad F_{Bz} = Z_a \rho dx dy dz \quad (6.7)$$

X_i (X_a , Y_a , or Z_a) = Body constants in different directions, $\frac{Ns^2}{m^4}$

3) Inertia forces

The inertia forces are the forces that are needed to accelerate or decelerate the fluid element. They are written in the equation (6.8).

$$F_{ix} = \rho \frac{Du}{dt} dx dy dz \quad F_{iy} = \rho \frac{Dv}{dt} dx dy dz \quad F_{iz} = \rho \frac{Dw}{dt} dx dy dz \quad (6.8)$$

$$\text{where } \frac{Du_i}{Dt} = \frac{\partial u_i}{\partial t} dt + \frac{\partial u}{\partial x} dx + \frac{\partial u}{\partial y} dy + \frac{\partial u}{\partial z} dz$$

Substituting the equations (6.5) through (6.8) into the equation (6.1), the Navier-Stokes equation is obtained [the equation (6.9)].

$$\begin{aligned} \rho \frac{Du_i}{Dt} &= \rho X_i + \frac{\partial \sigma_i}{\partial x_i} + \frac{\partial \tau_{ij}}{\partial x_j} + \frac{\partial \tau_{ik}}{\partial x_k} \\ &= \rho X_i - \frac{\partial P}{\partial x_i} - \frac{2}{3} \frac{\partial}{\partial x_i} \left[\eta \left(\frac{\partial u_i}{\partial x_i} + \frac{\partial u_j}{\partial x_j} + \frac{\partial u_k}{\partial x_k} \right) \right] + 2 \frac{\partial}{\partial x_i} \left(\eta \frac{\partial u_i}{\partial x_i} \right) \\ &\quad + \frac{\partial}{\partial x_j} \left[\eta \left(\frac{\partial u_i}{\partial x_j} + \frac{\partial u_j}{\partial x_i} \right) \right] + \frac{\partial}{\partial x_k} \left[\eta \left(\frac{\partial u_i}{\partial x_k} + \frac{\partial u_k}{\partial x_i} \right) \right] \end{aligned} \quad (6.9)$$

For the pin-on-disk tribological experiment conducted in this research, the viscous lubricant can be considered as a flow between two parallel flat plates (see Figure 6.10; $x_i = x$, $x_j = y$, and $x_k = z$). The reason is that the thickness of the fluid film is much smaller than the dimensions of the pin-on-disk configuration. Such flow configuration imposes the below assumptions:

- 1) Both body and inertia forces can be ignored;
- 2) Transient density change makes it constant;
- 3) Pressure gradient exists along the flow only (i.e. x direction), $\partial P / \partial x_j = \partial P / \partial x_k = 0$;

4) There is no leakage during the lubrication, terms $\partial u/\partial x_j = 0$.

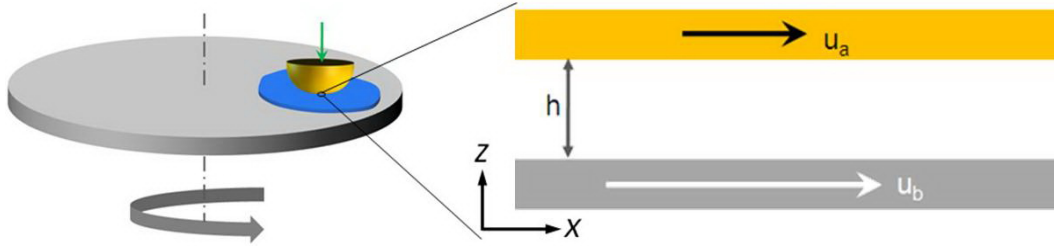


Figure 6.10. Lubricant flow between two parallel flat plates (top: pin; bottom: disk).

Having considered the assumptions listed above, the reduced Navier-Stokes equation is obtained in the equation (6.10):

$$\frac{dP}{dx} = \frac{d}{dz} \left[\eta \left(\frac{du}{dz} \right) \right] \quad (6.10)$$

η is treated as the averaged viscosity across the whole film. Solving the equation (6.10) with a no-slip boundary condition ($u = u_b$ when $z = 0$; $u = u_a$ when $z = h$), expression of the flow velocity across the film between the parallel plates is obtained [the equation (6.11)]:

$$u = u_b - z \left(\frac{h-z}{2\eta} \right) \frac{dp}{dx} - \frac{(u_b - u_a)z}{h} \quad (6.11)$$

Due to mass-conservation principle, the mass reduction within a fluid volume must be the same as the net out-mass-flow from it. The continuity equation can be expressed in the equation (6.12):

$$\int_0^h \left(\frac{\partial \rho}{\partial t} + \frac{\partial(\rho u)}{\partial x} \right) dz = 0 \quad (6.12)$$

Solving the integral based on the assumed simplification, the Reynolds equation is obtained for the present study in the equation (6.13):

$$\frac{\partial}{\partial x} \left(\frac{\rho h^3}{12\eta} \frac{\partial P}{\partial x} \right) = \frac{\partial}{\partial x} \left[\frac{\rho h (u_a + u_b)}{2} \right] - \rho u_a \frac{\partial h}{\partial x} \quad (6.13)$$

The reduced Reynolds equation (6.13) will be used to calculate the change of viscosity in a lubricant with or without the nano-additives.

6.3.2. Viscous flow analysis

6.3.2.1. Viscosity expression in pure lubricant

As a normal load is applied on the pin during the tribological measurements (Figure 6.10), the lubricant tends to be squeezed out from the spacing between the mating surfaces. The velocity profile of this normal squeeze-induced flow is shown in the top-left of Figure 6.11. The flow at the entrance has an opposite direction to that at the exit. Besides, shearing by the bottom disk, an entraining flow exists between the parallel plates. This flow rate decreases with the distance from the bottom-moving disk (see the bottom-left of Figure 6.11). Taking those two effects together into consideration, the localized flow-rate profile for the pure lubricant in this study is obtained in the right of Figure 6.11. More lubricant flows out of the exit, and a positive gradient for the hydrodynamic pressure is built within the film between the pin and the disk. A physical wedge is obtained, and the lubricant film thickness decreases in the flow direction.

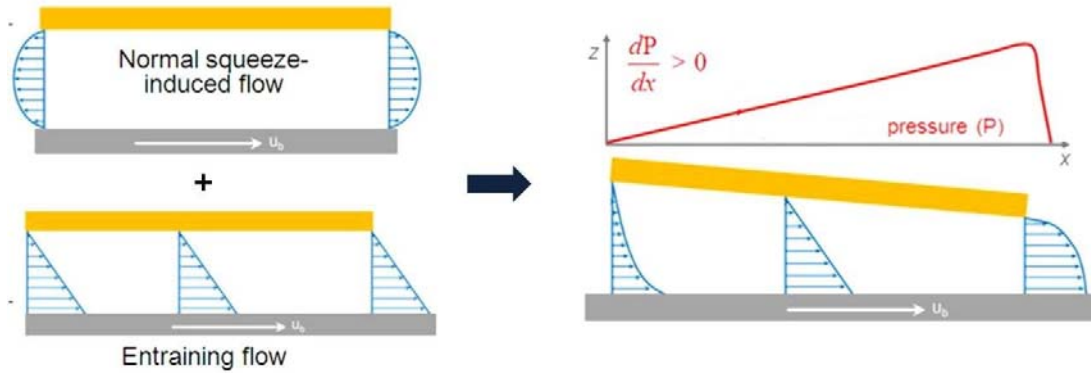


Figure 6.11. Flow-rate profile of pure lubricant flow.

It is noted that the pin is fixed in our tribological experiment ($u_a = 0$). The viscosity of the pure lubricant is calculated using the equation (6.13) and expressed as:

$$\eta_l = \frac{\rho h^3 \left(\frac{\partial P}{\partial x} \right)}{6\rho u_b h + C} = \frac{\text{Shear stress}}{\text{Shear rate}} \quad (6.14)$$

$C = \text{Constant}$

6.3.2.2. Viscosity with spherical nanoparticles as additives

When a spherical nanoparticle is added in the lubricant, the fluid dynamic behavior of the lubricant is modified. Flow rate close to the moving disk is higher than that far away from the disk. There is a higher flow rate (u_1 in Figure 6.12a) on the bottom surface of the nanoparticle than that on its top surface. As a result, the nanoparticle starts to rotate around its center in the lubricant flow, i.e. the nanoparticle spins. When the nanoparticle spins, the internal friction takes part in the lubricant flowing process. In such, the inertia contribution becomes visible. Vortices would form in the lubricant fluid and smooth flow condition is broken down. In addition, for the pure

lubricant, density variation associating with elastic vibration of lubricant molecules is a transient phenomenon. With the existence of nanoparticle, however, those elastic vibrations along the fluid direction are hindered. It is because the inorganic nanomaterials used in this research have much smaller elastic modulus, comparing to the long-chain lubricant molecules. Thus, freely expansion of flow is repressed evidently. The transient change of lubricant density cannot be maintained.

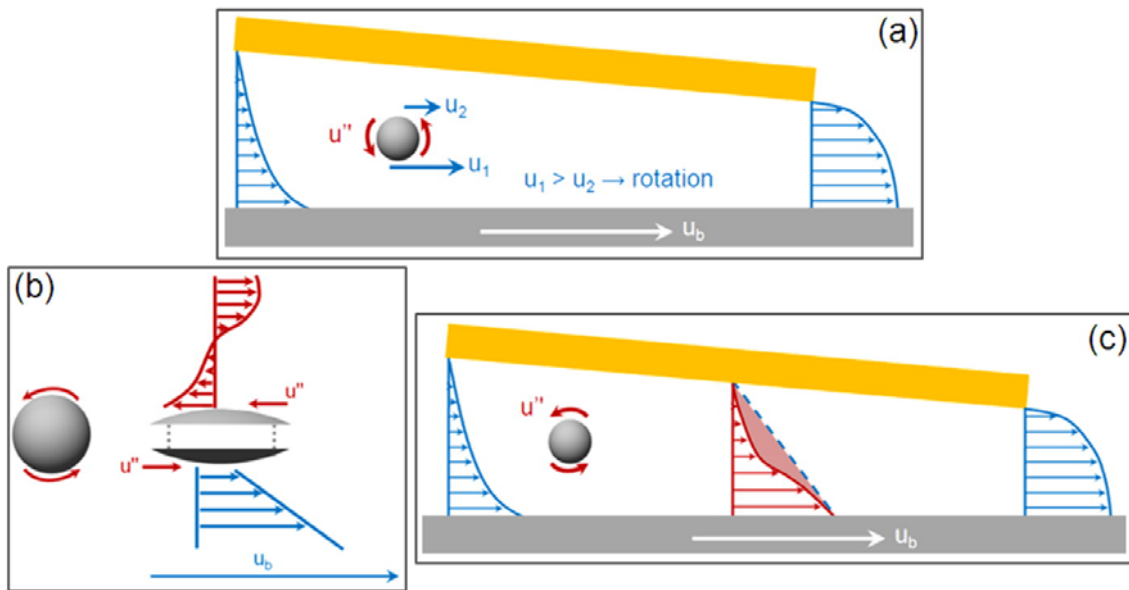


Figure 6.12. (a) Rotation (or spin) of the spherical nanoparticle under flow shearing; (b) flow distribution close to the nanoparticle surface; (c) flow-rate profile in lubricant that contains the nanoparticle additive.

Due to the nanoparticle rotation (or spin), both inertia effects and the repressed expansion leads to inhibiting the shearing process. The viscosity of the lubricant containing the nanoparticle additives can be rewritten as:

$$\eta_2 = \frac{\rho h^3 \left(\frac{\partial P}{\partial x} \right)}{6\rho u_b h + C - i(u,t) - \rho(u,t)} = \frac{\text{Shear stress}}{\text{Shear rate}} \quad (6.15)$$

C = Constant

$i(u,t)$ = Inertia effects

$\rho(u,t)$ = Repressed expansion-induced non-transient density change

As expressed in the equation (6.15), shear rate is decreased because of the inertia effects and the repressed expansion-induced non-transient density change. Consequently, viscosity is increased with the presence of nanoparticle in the lubricant. Such result is in accordance to the findings in tribological and rheological experiments discussed above.

The increased viscosity can be understood by analyzing the localized flow rate, as shown in Figures 6.12b and 6.12c. During the spin of nanoparticle, an opposite flow (u'' in Figure 6.12) to the lubricant flow is generated in the localized area close to its top surface (see Figure 6.12b). The flow-rate distribution approaching the nanoparticle's surface is negative. After integrating the flow-rate profile below and above the nanoparticle, the velocity distribution becomes narrow (see Figure 6.12c). The reddish area indicates schematically how much the velocity distribution is shrunk. In brief, the rotation of nanoparticle in lubricant enables the inertia effects and flow expansion to hinder the shearing process. Viscosity increased as a consequence of the decreased shear rate.

6.3.2.3. Viscosity with 2D nanosheets as additives

In the present research, an interesting non-Einstein-like viscosity reduction is observed, with which the reason for lubrication improvement is addressed. The 2D

sheet-like nano-additive is critical to the viscosity reduction. The lubricant with it behaves totally different from the other two lubricants discussed above. Similarly to that observed for the nanoparticle, the nanosheet would rotate in a lubricant flow as well. This is also due to the decreased flow rate in z direction (the left of Figure 6.13a). As the nanosheet has a much larger aspect ratio than the nanoparticle, a minor physical wedge forms (the right of Figure 6.13a). The height of this wedge is a function of its length [see the equation (6.16) and the right of Figure 6.13a]. The viscosity of the lubricant containing the nanosheet can be expressed as the equation (6.17).

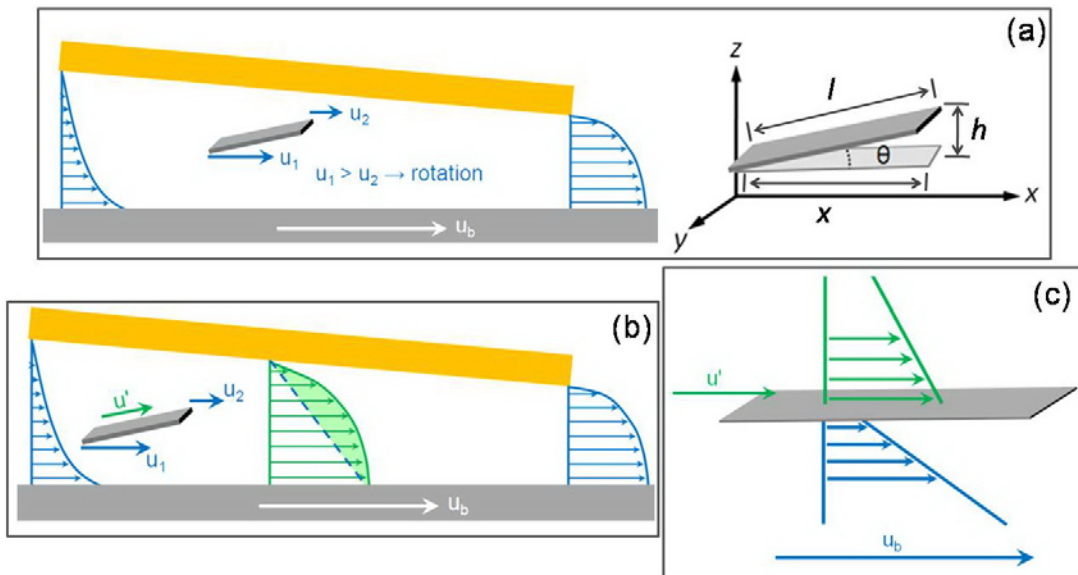


Figure 6.13. (a) Rotation of the 2D nanosheet under flow shearing; (b) flow-rate profile in lubricant that contains the 2D nano-additive; (c) flow distribution close to the nanosheet surface.

$$\frac{h}{x} = \tan \theta \quad \text{or} \quad \frac{h}{l} = \sin \theta \quad (6.16)$$

$$\eta_3 = \frac{\rho h^3 \left(\frac{\partial P}{\partial x} \right)}{6 \rho u_b l \sin \theta + C} = \frac{\text{Shear stress}}{\text{Shear rate}} \quad (6.17)$$

C = Constant

Depending on the rotating angle (θ), the viscosity expressed in the equation (6.17) is investigated under three conditions: 1) the nanosheet is parallel to the flow ($\theta \sim 0^\circ$, $\sin \theta \sim 0$); 2) the nanosheet inclines a little bit [θ is small ($45^\circ < \theta < 45^\circ$), $0 < \tan \theta \ll 1$]; and 3) the nanosheet rotates a lot [θ is large ($\theta > 45^\circ$, $\tan \theta > 1$)].

When nanosheet is parallel to the flow ($\theta \sim 0^\circ$, $\sin \theta \sim 0$):

The viscosity equation (6.17) can be reduced to:

$$\eta_{3-1} = \frac{\rho h^3 \left(\frac{\partial P}{\partial x} \right)}{C} = \frac{\text{Shear stress}}{\text{Shear rate}} \quad (6.18)$$

Comparing with the equation (6.14), the localized viscosity in the minor physical wedge is increased.

When nanosheet inclines a little bit [θ is small ($0^\circ < \theta < 45^\circ$), $0 < \tan \theta \ll 1$]:

The equation (6.17) is used to express the localized viscosity in the minor physical wedge. The small inclination (increased θ) would induce an increase in the shear rate, leading to the viscosity (η_3) reduction. Driven by the moving disk, shearing process in the minor physical wedge undergoes easily, and the lubricant flow along with the inclined nanosheet experiences less fluid drag. It is reasonable to believe that the

novel finding of viscosity reduction observed in the experiments is caused by the inclination of the 2D sheet-like nano-additives.

When nanosheet rotates a lot [θ is large ($\theta > 45^\circ$, $\tan \theta > 1$):

Elastic vibration of lubricant molecules is impeded by the solid surface of the nanosheet, resulting in localized variation in lubricant density. Similar to that occurs for the nanoparticle additives, the internal friction participates in elimination of the smooth lubricant flow. The inertia effects [$i(u,t)$] and the non-transient density variation [$\rho(u,t)$] should be included in the expression of localized viscosity for the minor physical wedge:

$$\eta_{3-2} = \frac{\rho h^3 \left(\frac{\partial P}{\partial x} \right)}{6\rho u_b l \sin \theta + C - i(u,t) - \rho(u,t)} = \frac{\text{Shear stress}}{\text{Shear rate}} \quad (6.19)$$

The inertia effects and the non-transient density variation are able to slow down the shearing process. Viscosity is thus increased due to the reduced shear rate, when there is notably rotated nanosheet in the lubricant.

Therefore, only the inclined nanosheet is capable of reducing viscosity of the lubricant. The localized flow rate analysis could account for such viscosity reduction. The results are schematically shown in Figures 6.13b and 6.13c. As there is a flow-rate difference ($u_1 > u_2$), another lubricant flow (u' in Figures 6.13b and 6.13c) presents on the top surface of the nanosheet in order to maintain the small inclined angle. This flow across the top surface of nanosheet is larger than that underneath it (see Figure 6.13c). In such, the flow-rate distribution is broadened with the nanosheet additive in lubricant (see Figure 6.13b). Greenish area schematically represents the widened flow-rate profile. In

sum, only the inclined nanosheet shows capability in reducing viscosity via an efficient shearing process.

6.3.3. Particle hydrodynamic simulation

The nanomaterial in a non-Newtonian fluid is modeled utilizing smoothed-particle hydrodynamics (SPH) with the addition of rigid body inclusions.³²⁹⁻³³¹ Total viscosity of the composite fluid matrix with a single inclusion of Y_2O_3 nanosheet (NS) or nanoparticle (NP) was simulated, and the results are shown in Figure 6.14. As we discussed in Sections 6.3.1 and 6.3.2, the Y_2O_3 NS is capable of inclining in the flow direction due to the unique 2D morphology at nanoscale. Figure 6.14a is the modeling domain of a rectangular shear cell. Having the Y_2O_3 NS oriented directly parallel (inclining at 0 degree) to the flow or with slight inclination (at 2 degree and 4 degree), a little bit increase in viscosity with respect to that of pure mineral oil is obtained (red dotted curves in Figure 6.14b). Having calculated 6, 8, and 10 degree inclination angles, it is observed that the steeper inclined angle results in more viscosity reduction (green dotted curves Figure 6.14b). On the contrary, the viscosity is increased with a single inclusion of Y_2O_3 NP (Figure 6.14c) in the SPH modeling. The non-Einstein-like viscosity reduction is further confirmed to be responsible by the inclination of Y_2O_3 NS in mineral oil under shear.

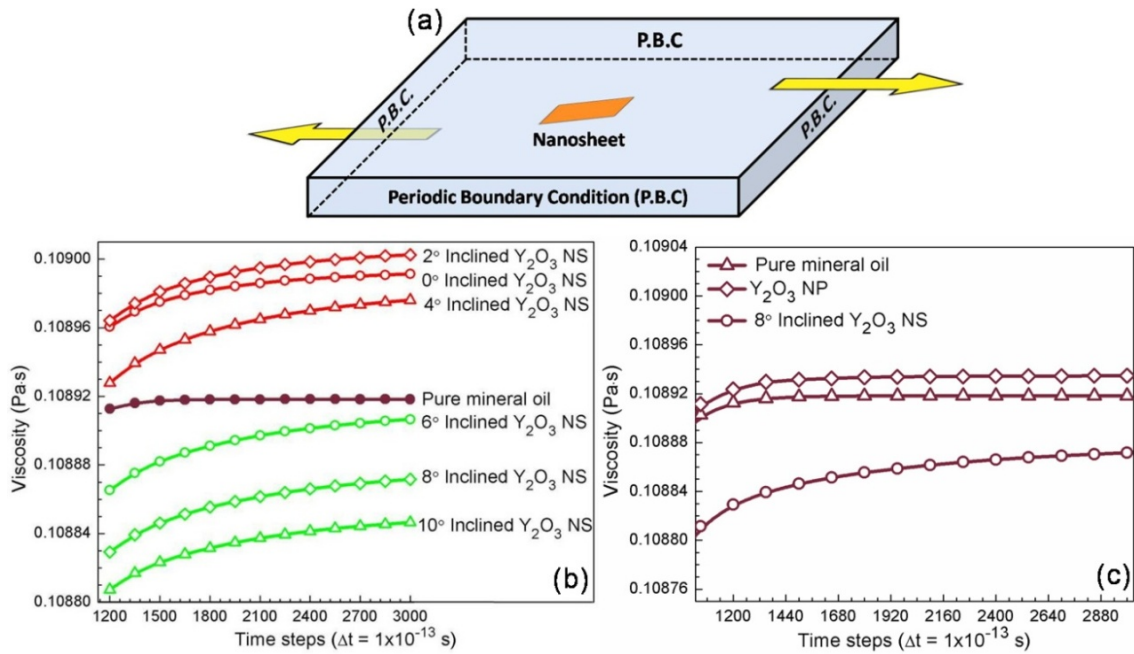


Figure 6.14. (a) Inclined Y_2O_3 NS in mineral oil modeled in a rectangular shear cell with periodic boundary conditions. (b) Total viscosity of the fluid matrix without and with a single inclusion of inclined Y_2O_3 NS at different degrees (0° , 2° , 4° , 6° , 8° , and 10°), under a constant shear rate ($10,000 \text{ s}^{-1}$). (c) Total viscosity of the fluid matrix without and with a single inclusion of Y_2O_3 NP and inclined Y_2O_3 NS.

The simulation results could be capitalized to provide insight into why the 2D nano-additives affect the shear behavior and improve the lubrication. The viscosity used in this chapter is the dynamic (shear) viscosity, defined as the ratio of shear stress to shear rate. Being proportional to viscosity, the shear stress is represented by three contributions: an interactive stress component, a Brownian stress component, and a hydrodynamic stress component.^{35,332-337} For a hard particle system (the Y_2O_3 NS and α -ZrP nanoplatelet), the interactive stress is zero.³³⁸ The random fluctuation of nanoparticles in a liquid suspension resulted in the Brownian stress.^{35,333,334} The

inclination of the 2D nanomaterials with respect to the flow of lubricant would significantly eliminate the chance of the random movement. The Brownian stress is reduced under shearing. On the other hand, a hydrodynamic stress is caused by the delay of the motion of dispersed particles with respect to the increase in shear strain.^{336,337} The inclined 2D sheet-like nano-additives in fluid direction are believed to decrease the time needed to build up the shear strain, resulting in the reduced hydrodynamic stress. On the contrary, the pure lubricant liquid is unable to keep up with the increased shear strain and leads to the high viscosity. As a whole, the inclination of the 2D nanomaterial additives with lubricant flow reduces the shear stress. The viscosity reduction induced by the 2D nano-additives is responsible for lubrication improvement.

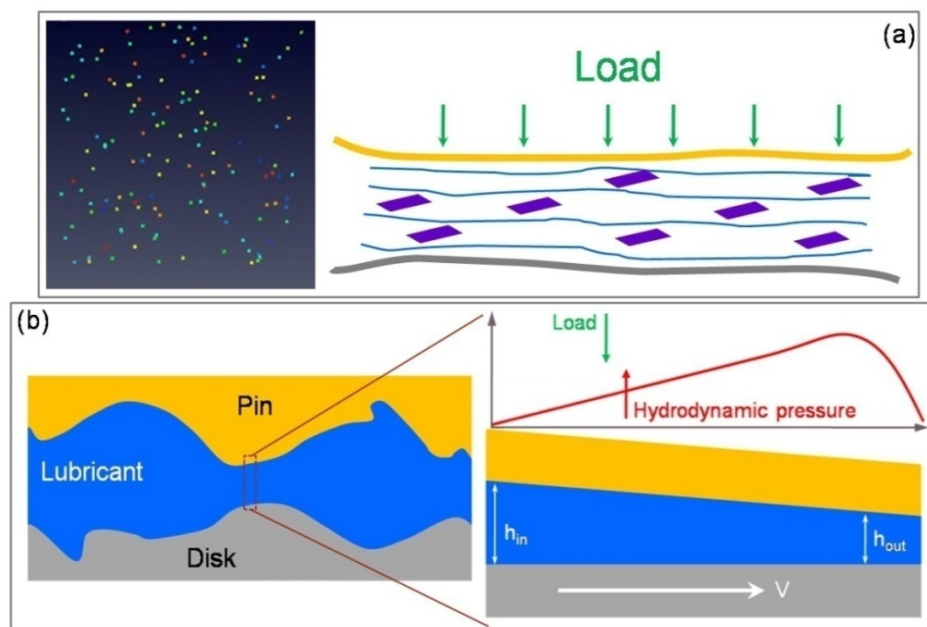


Figure 6.15. (a) Schematic top-view (the left) and side-view (the right) showing inclined alignment of the 2D nano-additives in the lubricants. (b) Schematic explanation of lubrication improvement via viscosity modification.

In order to understand the mechanisms of lubrication, a schematic is shown in Figure 6.15. The inclined alignment of the 2D sheet-like nano-additives (Figure 6.15a) is capable of reducing viscosity of lubricants. It is the non-Einstein-like viscosity reduction that improves the lubrication. The 2D morphology can facilitate alignment of the NS and the nanoplatelets in an inclined manner by applying a perpendicular fluid pressure and a parallel shearing (see discussion in Section 6.3.2). Such an inclined alignment would separate lubricant flow layers by laminar cutting,^{339,340} leading to decreased dynamic interaction (including momentum transfer). As a result, the laminar separation-induced reduction in fluid drag leads to the viscosity reduction (see Figures 6.6 through 6.8 and Figures 6.12 and 6.13).³³⁹⁻³⁴¹ In hydrodynamic lubrication, the characteristic is that a complete lubricant film forms as the contact surfaces are separated (the left of Fig. 6.15b). The separation is a result of hydrodynamic lift. A converging gap is the necessary geometry to produce hydrodynamic lubrication (also see Fig. 6.11).^{342,343} The hydrodynamic pressure and the applied load are in the kinetic equilibrium state in hydrodynamic-lubrication regime^{267,344}. Low viscosity of the lubricants increases localized fluid flow [see the equation (6.11)] and leads to higher hydrodynamic pressure, generating an extra hydrodynamic lift. The direction of the hydrodynamic pressure is opposite to the load. The extra hydrodynamic lift causes friction reduction in the hydrodynamic lubrication. In sum, the low viscosity of the lubricants with the presence of inclined 2D nanomaterial additives is evident (Figures 6.9 and 6.14). The lubrication improvement is caused by the novel non-Einstein-like viscosity reduction revealed in this study.

6.4. Summary

In this chapter, effective lubricating performance of 2D nanomaterials was evaluated first using Stribeck curves. The nano-additives were found to significantly improve lubricating performance in all lubrication regimes. Specifically, 0.1 wt % of Y_2O_3 nanosheets and α -ZrP nanoplatelets in mineral oil reduced the friction as much as by $\sim 40\%$ and $\sim 65\%$, respectively.

Their rheological behaviors were investigated to understand the lubricating behavior. A novel non-Einstein-like viscosity reduction was observed with the addition of 2D nanoparticles. In mineral oil, the viscosity was reduced by $\sim 4\%$ and $\sim 7\%$, respectively, using Y_2O_3 nanosheets and α -ZrP nanoplatelets.

In order to understand the fluidic-modification mechanisms, structure-fluid-lubrication relationship was established using fluid mechanics calculation, viscous flow analysis, and computational simulation. It was discovered that the 2D nanoparticles could reduce viscosity via inclination in flow direction. On the contrary, the spherical nanoparticles increased viscosity due to the inertia effects and the non-transient density variation. The non-Einstein-like viscosity reduction led to the improved lubricating performance. The utilization of 2D nanomaterials provides an innovative solution in improving fluidic lubricating efficiency. Based on the tribological and rheological investigation, the conclusions and the recommendation for future works will be described in Chapter VII.

CHAPTER VII

CONCLUSIONS AND FUTURE WORKS

7.1. Conclusions

This research investigated the use of two-dimensional (2D) nanomaterials to improve lubricating performance via a non-Einstein-like viscosity reduction. The 2D nanoparticles are an entirely new family of lubricant additives. When compared to other shaped nano-additives, the 2D showed exceptional performance in the friction reduction and the viscosity modification for fluidic lubricants.

In this work, two types of 2D nanoparticles were synthesized using a facile hydrothermal method: yttrium oxide (Y_2O_3) nanosheets (sized ~ 320 and ~ 15 nm thick) and α -zirconium phosphate (ZrP) nanoplatelets (sized ~ 600 nm to $1 \mu\text{m}$ and ~ 30 nm thick). Their 2D morphology at nanoscale was confirmed with various characterizations. Especially for the Y_2O_3 nanosheets, an interesting transformation from multiphase to single-phase was observed. The single-phase Y_2O_3 nanosheets were found to possess a unique negative resistance, while the multiphase counterpart shows a Schottky-barrier behavior. It was the 2D shape that enables the Y_2O_3 nanosheets to have such a novel property. Furthermore, a chemical vapor deposition system was built to synthesize B- B_2O_3 composited nanoparticles. On a catalyzed substrate, the size of the nanoparticles could be regulated (from ~ 5 nm to ~ 100 s nm) by controlling the deposition rate. 2D nanostructured surface on the B- B_2O_3 nanoparticles were characterized as well.

Pin-on-disk configured tribological experiments were conducted to examine the lubrication using different additives. There was a critical concentration, below which friction reduction would present. The morphology of the additive at nanoscale was critical in friction reduction. Only the 2D nanoparticles showed significant friction reduction in all cases of combination in applied loads, rotational speeds, and base liquids. The improved lubricating performance was further proved by plotting the Stribeck curves for lubricants containing 2D nano-additives. Lubricating efficiency was found to be increased significantly in all lubrication regimes. The Y_2O_3 nanosheets and the α -ZrP nanoplatelet additives reduced the friction by $\sim 40\%$ and $\sim 65\%$, respectively, in mineral oil. In addition, such low-friction process was applied to chemical mechanical planarization (CMP) of copper. A high degree of flatness was obtained after CMP, using the slurry containing the 2D nanomaterials.

Rheological investigation revealed that a non-Einstein-like viscosity reduction was responsible for friction reduction. Utilizing the additives of Y_2O_3 nanosheets and α -ZrP nanoplatelets, the viscosity of mineral oil was reduced by $\sim 4\%$ and $\sim 7\%$, respectively. In order to investigate the mechanisms of fluidic modification, fluid mechanics calculation, viscous flow analysis, and computational simulation were carried out. The inclination of the sheet-like nanoparticle in the lubricant flow was found to induce the viscosity reduction. Consequently, improvement in the tribological performance was caused by the viscosity reduction.

Using 2D nanomaterials, novel solution was developed to improve tribological performance and the rheological behaviors. The findings in the present research will

broaden the materials scope for a wide range of fluidic-related applications. The structure-fluid-lubrication relationship established here is believed to shed new light on the research of nano-fluid and nano-lubrication. Such understanding would have great impacts on engineering and science communities that concern about nanomaterials innovation, energy saving, and manufacturing efficiency.

7.2. Future works

The challenging needs of viscosity reduction for next generation of lubricants can be fulfilled using the 2D nano-additives. Future study will focus on integration of the novel additives with a broad range of existed lubricants. Based on results founded in this research, the below actions and works are suggested:

- 1) More efficient viscosity-reduction additives: As summarized in the Table 1.1, 2D nanoparticles are a big family of materials. Further improvement would be obtained using better 2D nano-particulate additives in lubricant. Their dimension, structure, and surface functionalization can be modified depending on the tribological or fluidic applications.
- 2) Investigation of chemical/physical interaction: The current research emphasizes the effects of the 2D nano-additives on the fluidic behavior of lubricant. Interactions between the lubricant molecules also play equivalently important roles in determining lubricant's viscosity. Further

detailed study regarding the interactions between the additives and lubricant molecules indeed necessary.

- 3) Synergetic effects: The lubricants used in this research consisted of a base liquid and one type of additives. However, a real lubricant should also have: demulsibility, hydraulic and thermal stability, high viscosity index, corrosion resistance, and low freezing point and high boiling point. Conventional additives discussed in the Chapter I were used to enable the lubricant to possess those characteristics. The performance of the 2D nano-additives should be evaluated synergistically with the conventional additives.

- 4) *In-situ* fluidic characterization: The fluidic behaviors of the 2D nanoparticles were investigated theoretically in the present research. *In-situ* fluid dynamic characterizations of the flow-rate distribution, pressure distribution, and lubricating film thickness would ultimately provide solid foundation for the wide applications of the novel additives in a real world.

REFERENCES

- 1 Holmberg, K., Andersson, P. & Erdemir, A. Global energy consumption due to friction in passenger cars. *Tribol. Int.* **47**, 221-234 (2012).
- 2 Rudnick, L. R. *Lubricant additives: Chemistry and applications*. Boca Raton, FL, CRC Press, (2009).
- 3 Ahmed, N. S. & Nassar, A. M. *Tribology - Lubricants and lubrication*. Rijeka, Croatia, InTech, (2011).
- 4 Rizvi, S. Q. A. *A comprehensive review of lubricant chemistry, technology, selection, and design*. West Conshohocken, PA, ASTM International, (2009).
- 5 Buckley, D. H. *Properties of surfaces*. New York, NY, CRC Press, (1988).
- 6 Israelachvili, J. N. *Intermolecular and surface forces*. San Diego, CA, Academic Press, (2011).
- 7 MORTIER, R. M., MALCOLM, F. F., ORSZULIK, S. T., *Chemistry and technology of lubricants*. Houten, Netherlands, Springer, (2010).
- 8 Tonck, A., Martin, J. M., Kapsa, P. & Georges, J. M. Boundary lubrication with anti-wear additives: study of interface film formation by electrical contact resistance. *Tribol. Int.* **12**, 209-213 (1979).
- 9 Spikes, H. Low- and zero-sulphated ash, phosphorus and sulphur anti-wear additives for engine oils. *Lubr. Sci.* **20**, 103-136 (2008).
- 10 Taylor, L., Dratva, A. & Spikes, H. A. Friction and wear behavior of zinc dialkyldithiophosphate additive. *Tribol. Trans.* **43**, 469-479 (2000).
- 11 Qian, Z., Minnikanti, V. S. & Archer, L. A. Surface segregation of highly branched polymer additives in linear hosts. *J. Polym. Sci. Part B Polym. Phys.* **46**, 1788-1801 (2008).
- 12 Leonov, A. I. & Prokunin, A. N. *Nonlinear phenomena in flows of viscoelastic polymer fluids*. Houten, Netherlands, Springer, (1994).
- 13 Kajdas, C. Additives for metalworking lubricants-a review. *Lubr. Sci.* **1**, 345-409 (1989).

- 14 Ratoi, M. & Spikes, H. A. Lubricating properties of aqueous surfactant solutions. *Tribol. Trans.* **42**, 479-486 (1999).
- 15 Hamblin, P. C., Kristen, U. & Chasan, D. Ashless antioxidants, copper deactivators and corrosion inhibitors: Their use in lubricating oils. *Lubr. Sci.* **2**, 287-318 (1990).
- 16 Kang, J., Fu, R.-D., Luan, G.-H., Dong, C.-L. & He, M. In-situ investigation on the pitting corrosion behavior of friction stir welded joint of AA2024-T3 aluminium alloy. *Corros. Sci.* **52**, 620-626 (2010).
- 17 Carvalho, M. J. S. d., Seidl, P. R., Belchior, C. R. P. & Sodr e, J. R. Lubricant viscosity and viscosity improver additive effects on diesel fuel economy. *Tribol. Int.* **43**, 2298-2302 (2010).
- 18 Marsden, K. Literature review of OCP viscosity modifiers. *Lubr. Sci.* **1**, 265-280 (1989).
- 19 Jukić, A., Tomašek, L. J. & Janović, Z. Polyolefin and poly(alkyl methacrylate) mixed additives as mineral lubricating oil rheology modifiers. *Lubr. Sci.* **17**, 431-449 (2005).
- 20 Einstein, A. On the theory of Brownian movement. *Ann. Phys. (Leipz.)* **19**, 371-381 (1906).
- 21 Yao, Z. L., Grishkewich, N. & Tam, K. C. Swelling and shear viscosity of stimuli-responsive colloidal systems. *Soft Matter* **9**, 5319-5335 (2013).
- 22 Romeo, G., Imperiali, L., Kim, J.-W., Fernández-Nieves, A. & Weitz., D. A. Origin of de-swelling and dynamics of dense ionic microgel suspensions. *J. Chem. Phys.* **136**, 124905-124909 (2012).
- 23 Senff, H. & Richtering, W. Temperature sensitive microgel suspensions: Colloidal phase behavior and rheology of soft spheres. *J. Chem. Phys.* **111**, 1705-1711 (1999).
- 24 Liu, J., Zhang, L., Cao, D. & Wang, W. Static, rheological and mechanical properties of polymer nanocomposites studied by computer modeling and simulation. *Phys. Chem. Chem. Phys.* **11**, 11365-11384 (2009).
- 25 Duan, F., Kwek, D. & Crivoi, A. Viscosity affected by nanoparticle aggregation in Al₂O₃-water nanofluids. *Nanoscale Res. Lett.* **6**, 248 (2011).

- 26 VanDerWerff, J. C. & de Kruif, C. G. Hard-sphere colloidal dispersions: the scaling of rheological properties with particle size, volume fraction, and shear rate. *J. Rheol.* **33**, 421-454 (1989).
- 27 Russel, W. B., Saville, D. A. & Schowalter, W. R. *Colloidal Dispersions*. New York, NY, Cambridge Univ. Press, (1989).
- 28 Batchelor, G. K. The effect of Brownian motion on the bulk stress in a suspension of spherical particles. *J. Fluid Mech.* **83**, 97-117 (1977).
- 29 Mazur, P. & Van Saarloos, W. Many-sphere hydrodynamic interactions and mobilities in a suspension. *Physica A* **115**, 21-57 (1982).
- 30 Beenakker, C. W. J. & Mazur, P. Diffusion of spheres in a concentrated suspension. II. *Physica A* **126**, 349-370 (1984).
- 31 Beenakker, C. W. J. The effective viscosity of a concentrated suspension of spheres (and its relation to diffusion). *Physica A* **128**, 48-81 (1984).
- 32 Cichocki, B. & Felderhof, B. U. Short-time diffusion coefficients and high frequency viscosity of dilute suspensions of spherical Brownian particles. *J. Chem. Phys.* **89**, 1049-1055 (1988).
- 33 Clercx, H. J. H. & Schram, P. P. J. M. High-frequency effective viscosity of hard-sphere suspensions. *Phys. Rev. A* **45**, 860-872 (1992).
- 34 Ladd, A. J. C. Hydrodynamic transport coefficients of random dispersions of hard spheres. *J. Chem. Phys.* **93**, 3484-3494 (1990).
- 35 Bossis, G. & Brady, J. F. The rheology of Brownian suspensions. *Journal of Chemical Physics* **91**, 1866-1874 (1989).
- 36 Mewis, J. & J. Wagner, N. Current trends in suspension rheology. *J. Non-Newtonian Fluid Mech.* **157**, 147-150 (2009).
- 37 Aveyard, R. R., Brinks, B. P. & Clint, J. H. Emulsions stabilised solely by colloidal particles. *Adv. Colloid Interface Sci.* **100**, 503-546 (2003).
- 38 Ladd, A. J. C. Numerical simulations of particulate suspensions via a discretized Boltzmann equation,. *J. Fluid Mech.* **271**, 311-319 (1994).
- 39 Martys, N. S. Study of a dissipative particle dynamics based approach for modeling suspensions,. *J. Rheol.* **49**, 401-424 (2005).

- 40 Pozrikidis, C. Orientation statistics and effective viscosity of suspensions of elongated particles in simple shear flow. *Eur. J. Mech. B/Fluids* **24**, 125-136 (2005).
- 41 Tanaka, H. & Araki, T. Simulation method of colloidal suspensions with hydrodynamic interactions: fluid particle dynamics. *Phys. Rev. Lett.* **85**, 1338-1341 (2000).
- 42 Yurkovetsky, Y. & Morris, J. F. Particle pressure in sheared Brownian suspensions. *J. Rheol.* **52**, 141-164 (2008).
- 43 Shapley, N. C., Armstrong, R. C. & Brown, R. A. Evaluation of particle migration models based on laser Doppler velocimetry measurements in concentrated suspensions. *J. Rheol.* **48**, 255-279 (2004).
- 44 Ovarlez, G., Bertrand, F. & Rodts, S. Local determination of the constitutive law of a dense suspension of noncolloidal particles through magnetic resonance imaging. *J. Rheol.* **50**, 259-292 (2006).
- 45 Wierenga, A., Philipse, A. P. & Lekkerkerker, H. N. W. Aqueous dispersions of colloidal boehmite: structure, dynamics, and yield stress of rod gels. *Langmuir* **14**, 55-65 (1998).
- 46 Mohraz, A. & Solomon, M. J. Gelation and internal dynamics of colloidal rod aggregates. *J. Colloid Interface Sci.* **300**, 155-162 (2006).
- 47 Egres, R. G., Nettekheim, F. & Wagner, N. J. Rheo-SANS investigation of acicular-precipitated calcium carbonate colloidal suspensions through the shear thickening transition. *J. Rheol.* **50**, 685-709 (2006).
- 48 Scirocco, R., Vermant, J. & Mewis, J. Effect of the viscoelasticity of the suspending fluid on structure formation in suspensions. *J. Non-Newtonian Fluid Mech.* **117**, 183-192 (2004).
- 49 Meins, J.-F. L., Moldenaers, P. & Mewis, J. Suspensions of monodisperse spheres in polymer melts: particle size effects in extensional flow. *Rheol. Acta* **42**, 184-190 (2003).
- 50 Green, D. L. & Mewis, J. Connecting the wetting and rheological behaviors of poly(dimethylsiloxane)-grafted silica spheres in poly(dimethylsiloxane) melts. *Langmuir* **22**, 9546-9553 (2006).
- 51 Buscall, R. & Ettelaie, R. Colloidal dispersions in polymer melts. *Ind. Eng. Chem. Res.* **45**, 6915-6922 (2006).

- 52 Jain, S., Goossens, J. G. P., Peters, G. W. M., Duin, M. V. & Lemstra, P. J. Strong decrease in viscosity of nanoparticle-filled polymer melts through selective adsorption. *Soft matter* **4**, 1848 (2008).
- 53 Tan, Y., Song, Y. & Zheng, Q. Hydrogen bonding-driven rheological modulation of chemically reduced graphene oxide/poly(vinyl alcohol) suspensions and its application in electrospinning. *Nanoscale* **4**, 6997 (2012).
- 54 Thomas, S. P., Girei, S. A., Atieh, M. A., De, S. K. & Al-Juhani, A. Rheological behavior of polypropylene nanocomposites at low concentration of surface modified carbon nanotubes. *Polym. Eng. Sci.* **52**, 1868-1873 (2012).
- 55 Mackay, M. E. *et al.* Nanoscale effects leading to non-Einstein-like decrease in viscosity. *Nat. Mater.* **2**, 762-766 (2003).
- 56 Sacanna, S., Kegel, W. K. & Philipse, A. P. Thermodynamically stable Pickering emulsions. *Phys. Rev. Lett.* **98**, 158301 (2007).
- 57 Ashby, N. P., Binks, B. P. & Paunov, V. N. Bridging interaction between a water drop stabilised by solid particles and a planar oil/water interface. *Chem. Commun.*, 436-437 (2004).
- 58 Horozov, T. S. & Binks, B. P. Particle-stabilized emulsions: A bilayer or a bridging monolayer? *Angew. Chem. Int. Ed.* **45**, 773-776 (2006).
- 59 Horozov, T. S., Aveyard, R., Clint, J. H. & Neumann, B. Particle zips: vertical emulsion films with particle monolayers at their surfaces. *Langmuir* **21**, 2330-2341 (2005).
- 60 Xu, H., Lask, M., Kirkwood, J. & Fuller, G. Particle bridging between oil and water interfaces. *Langmuir* **23**, 4837-4841 (2007).
- 61 Hsu, S. M. Nano-lubrication: concept and design. *Tribol. Int.* **37**, 537-545 (2004).
- 62 Greco, A., Mistry, K., Sista, V., Eryilmaz, O. & Erdemir, A. Friction and wear behaviour of boron based surface treatment and nano-particle lubricant additives for wind turbine gearbox applications. *Wear* **271**, 1754-1760 (2011).
- 63 Rapoport, L. *et al.* Friction and wear of bronze powder composites including fullerene-like WS₂ nanoparticles. *Wear* **249**, 149-156 (2001).
- 64 Greenberg, R., Halperin, G., Etsion, I. & Tenne, R. The effect of WS₂ nanoparticles on friction reduction in various lubrication regimes. *Tribol. Lett.* **17**, 179-186 (2004).

- 65 Chen, C. S., Chen, X. H., Xu, L. S., Yang, Z. & Li, W. H. Modification of multi-walled carbon nanotubes with fatty acid and their tribological properties as lubricant additive. *Carbon* **43**, 1660-1666 (2005).
- 66 Lin, J., Wang, L. & Chen, G. Modification of graphene platelets and their tribological properties as a lubricant additive. *Tribol. Lett.* **41**, 209-215 (2011).
- 67 Tenne, R. Hollow nanoparticles of WS₂ as potential solid-state lubricants. *Angew. Chem. Int. Ed.* **42**, 5124-5132 (2003).
- 68 Rapoport, L. *et al.* Polymer nanocomposites with fullerene-like solid lubricant. *Adv. Eng. Mater.* **6**, 44-48 (2004).
- 69 Rapoport, L., Fleischer, N. & Tenne, R. Applications of WS₂ (MoS₂) inorganic nanotubes and fullerene-like nanoparticles for solid lubrication and for structural nanocomposites. *J. Mater. Chem.* **15**, 1782-1788 (2005).
- 70 Brown, S. *et al.* Bulk vs nanoscale WS₂: Finite size effects and solid-state lubrication. *Nano Lett.* **7**, 2365-2369 (2007).
- 71 Rapoport, L. *et al.* Hollow nanoparticles of WS₂ as potential solid-state lubricants. *Nature* **387**, 791-793 (1997).
- 72 Kim, K.-S. *et al.* Chemical vapor deposition-grown graphene: The thinnest solid lubricant. *ACS Nano* **5**, 5107-5114 (2011).
- 73 Savan, A., Pflüger, E., Voumard, P., Schröer, A. & Simmonds, M. Modern solid lubrication: Recent developments and applications of MoS₂. *Lubr. Sci.* **12**, 185-203 (2000).
- 74 Watanabe, S., Noshiro, J. & Miyake, S. Tribological characteristics of WS₂/MoS₂ solid lubricating multilayer films. *Surf. Coat. Technol.* **183**, 347-351 (2004).
- 75 Yadgarov, L. *et al.* Tribological studies of rhenium doped fullerene-like MoS₂ nanoparticles in boundary, mixed and elasto-hydrodynamic lubrication conditions. *Wear* **297**, 1103-1110 (2013).
- 76 Song, H. & Li, N. Frictional behavior of oxide graphene nanosheets as water-base lubricant additive. *Appl. Phys. A* **105**, 827-832 (2011).
- 77 Eswaraiyah, V., Sankaranarayanan, V. & Ramaprabhu, S. Graphene-based engine oil nanofluids for tribological applications. *ACS Appl. Mater. Interfaces* **3**, 4221-4227 (2011).
- 78 Huang, H. D., Tu, J. P., Gan, L. P. & Li, C. Z. An investigation on tribological properties of graphite nanosheets as oil additive. *Wear* **261**, 140-144 (2006).

- 79 Rapoport, L., Fleischer, N. & Tenne, R. Fullerene-like WS₂ nanoparticles: superior lubricants for harsh conditions. *Adv. Mater.* **15**, 651-655 (2003).
- 80 Novoselov, K. S. *et al.* A roadmap for graphene. *Nature* **490**, 192-200 (2012).
- 81 Zomer, P. J., Dash, S. P., Tombros, N. & Wees, B. J. v. A transfer technique for high mobility graphene devices on commercially available hexagonal boron nitride. *Appl. Phys. Lett.* **99**, 232104 (2011).
- 82 Jin, Z., Yao, J., Kittrell, C. & Tour, J. M. Atomic layers of hybridized boron nitride andgraphenedomains. *ACS Nano* **5**, 4112-4117 (2011).
- 83 Mayorov, A. S. *et al.* Micrometer-scale ballistic transport in encapsulated graphene at room temperature. *Nano Lett.* **11**, 2396-2399 (2011).
- 84 Park, S. & Ruoff, R. S. Chemical methods for the production of graphenes *Nat. Nanotechnol.* **4**, 217-224 (2009).
- 85 Ci, L. *et al.* Atomic layers of hybridized boron nitride andgraphenedomains. *Nature Mater.* **9**, 430-435 (2010).
- 86 Nair, R. R. *et al.* Fluorographene: a two-dimensional counterpart of Teflon. *Small* **6**, 2877-2884 (2010).
- 87 Geim, A. K. & Novoselov, K. S. The rise of graphene. *Nature Mater.* **6**, 183-191 (2007).
- 88 Wang, Q. H., Kalantar-Zadeh, K., Kis, A., Coleman, J. N. & Strano, M. S. Electronics and optoelectronics of two-dimensional transition metal dichalcogenides. *Nat. Nanotechnol.* **7**, 699-712 (2012).
- 89 Li, H. *et al.* Fabrication of single- and multilayer MoS₂ film-based field-effect transistors for sensing NO at room temperature. *Small* **8**, 63-67 (2012).
- 90 Tongay, S. *et al.* Thermally driven crossover from indirect toward direct bandgap in 2D semiconductors: MoSe₂ versus MoS₂. *Nano Lett.* **12**, 5576-5580 (2012).
- 91 Matte, H. S. S. R. *et al.* MoS₂ and WS₂ analogues of graphene. *Angew. Chem.* **122**, 4153-4156 (2010).
- 92 Chiritescu, C. *et al.* Ultralow thermal conductivity in disordered, layered WSe₂ crystals. *Science* **315**, 351-353 (2007).
- 93 Zhao, W. *et al.* Evolution of electronic structure in atomically thin sheets of WS₂ and WSe₂. *ACS Nano* **7**, 791-797 (2013).

- 94 Fang, H. *et al.* High-performance single layered WSe₂ p-FETs with chemically doped contacts. *Nano Lett.* **12**, 3788-3792 (2012).
- 95 Xu, M., Liang, T., Shi, M. & Chen, H. Graphene-like two-dimensional materials. *Chem. Rev.* **113**, 3766-3798 (2013).
- 96 Löher, T., Tomm, Y., Pettenkofer, C., Klein, A. & Jaegermann, W. Structural dipoles at interfaces between polar II-VI semiconductors CdS and CdTe and non-polar layered transition metal dichalcogenide semiconductors MoTe₂ and WSe₂. *Semicond. Sci. Technol.* **15**, 514-522 (2000).
- 97 Siemeling, U. Tellurium-an interesting bonding partner for transition metals: new results from molecular chemistry. *Angew. Chem. Int. Ed. Engl* **32**, 67-68 (1993).
- 98 Koski, K. J. & Cui, Y. The new skinny in two-dimensional nanomaterials. *ACS Nano* **7**, 3739-3743 (2013).
- 99 Han, J. H., Lee, S. & Cheon, J. Synthesis and structural transformations of colloidal 2D layered metal chalcogenide nanocrystals. *Chem. Soc. Rev.* **42**, 2581-2591 (2013).
- 100 Li, L. *et al.* Electrical transport and high-performance photoconductivity in individual ZrS₂ nanobelts. *Adv. Mater.* **22**, 4151-4156 (2010).
- 101 Brauer, H. E., Starnberg, H. I., Holleboom, L. J. & Hughes, H. P. In situ intercalation of the layered compounds TiS₂, ZrSe₂ and VSe₂. *Surf. Sci.* **331-333**, 419-424 (1995).
- 102 Mosca, D. H. *et al.* Mechanical properties of layered InSe and GaSe single crystals. *J. Appl. Phys.* **91**, 140 (2002).
- 103 Hu, P., Wen, Z., Wang, L., Tan, P. & Xiao, K. Synthesis of few-layer GaSe nanosheets for high performance photodetectors. *ACS Nano* **6**, 5988-5994 (2012).
- 104 Mandal, K. C. *et al.* Layered GaTe crystals for radiation detectors. *IEEE T. Nucl. Sci.* **58**, 1981-1986 (2002).
- 105 Lee, D. S. *et al.* Crystal structure, properties and nanostructuring of a new layered chalcogenide semiconductor, Bi₂MnTe₄. *CrystEngComm* **15**, 5532-5538 (2013).
- 106 Kong, D. *et al.* Few-layer nanoplates of Bi₂Se₃ and Bi₂Te₃ with highly tunable chemical potential. *Nano Lett.* **10**, 2245-2250 (2010).

- 107 Zhang, J. *et al.* Raman spectroscopy of few-quintuple layer topological insulator Bi₂Se₃ nanoplatelets. *Nano Lett.* **11**, 2407-2414 (2011).
- 108 Samuely, P. *et al.* Two-dimensional behavior of the naturally layered superconductor (LaSe)_{1.14}(NbSe₂). *Phys. C* **369**, 61-67 (2002).
- 109 Novoselov, K. S. *et al.* Two-dimensional atomic crystals. *Proc. Natl. Acad. Sci. USA* **102**, 10451-10453 (2005).
- 110 Izawa, K. *et al.* A new approach for the synthesis of layered niobium sulfide and restacking route of NbS₂ nanosheet. *J. Solid State Chem.* **181**, 319-324 (2008).
- 111 Wu, X.-C., Tao, Y.-R., Gao, Q.-X., Mao, C.-J. & Zhu, J.-J. Superconducting TaS_{2-x}I_y hierarchical nanostructures. *Chem. Commun.*, 4290-4292 (2009).
- 112 Panneerselvam, A., Malik, M. A., Afzaal, M., O'Brien, P. & Helliwell, M. The chemical vapor deposition of nickel phosphide or selenide thin films from a single precursor. *J. Am. Chem. Soc.* **130**, 2420-2421 (2008).
- 113 Osada, M. & Sasaki, T. Two-dimensional dielectric nanosheets: novel nanoelectronics from nanocrystal building blocks. *Adv. Mater.* **24**, 210-228 (2012).
- 114 Addou, R., Dahal, A. & Batzill, M. Growth of a two-dimensional dielectric monolayer on quasi-freestanding graphene. *Nat. Nanotechnol.* **8**, 41-45 (2013).
- 115 Pang, H. *et al.* 2D single- or double-layered vanadium oxide nanosheet assembled 3D microflowers: controlled synthesis, growth mechanism, and applications. *Nanoscale* **5**, 7790-7794 (2013).
- 116 Zhao, Y. M. *et al.* Two-dimensional tungsten oxide nanowire networks. *Appl. Phys. Lett.* **89**, 133116 (2006).
- 117 Odelius, M., Bernasconi, M. & Parrinello, M. Two dimensional ice adsorbed on mica surface. *Phys. Rev. Lett.* **78**, 2855-2858 (1997).
- 118 Badica, P. & Togano, K. Growth of superconducting and non-superconducting whiskers in the Bi-Sr-Ca-Cu-O (BSCCO) system. *J. Mater. Res.* **20**, 3358-3367 (2005).
- 119 Fang, M. *et al.* Layer-by-layer growth and condensation reactions of niobate and titanoniobate thin films. *Chem. Mater.* **11**, 1526-1532 (1999).
- 120 Omomo, Y., Sasaki, T., Lianzhou & Watanabe, M. edoxable nanosheet crystallites of MnO₂ derived via delamination of a layered manganese oxide. *J. Am. Chem. Soc.* **125**, 3568-3575 (2003).

- 121 Saupe, G. B. *et al.* Nanoscale tubules formed by exfoliation of potassium hexaniobate. *Chem. Mater.* **12**, 1556-1562 (2000).
- 122 Fukuda, K., Nakai, I., Ebina, Y., Ma, R. & Sasaki, T. Colloidal unilamellar layers of tantalum oxide with open channels. *Inorg. Chem.* **46**, 4787-4789 (2007).
- 123 Sugimoto, W., Iwata, H., Yasunaga, Y., Murakami, Y. & Takasu, Y. Preparation of ruthenic acid nanosheets and utilization of its interlayer surface for electrochemical energy storage. *Angew. Chem. Int. Ed.* **42**, 4092-4096 (2003).
- 124 He, X., Zhou, Y. & Liang, H. Cuⁿ⁺-assisted synthesis of multi- and single-phase yttrium oxide nanosheets. *J. Mater. Chem. C* **1**, 6829-6834 (2013).
- 125 Butler, S. Z. *et al.* Progress, challenges, and opportunities in two-dimensional materials beyond graphene. *ACS Nano* **7**, 2898-2926 (2013).
- 126 Schaak, R. E. & Mallouk, T. E. Perovskites by design: A toolbox of solid-state reactions. *Chem. Mater.* **14**, 1455-1471 (2002).
- 127 Kim, o.-Y., Chung, I., Choy, J.-H. & Park, G.-S. Macromolecular nanoplatelet of aurivillius-type layered perovskite oxide, Bi₄Ti₃O₁₂. *Chem. Mater.* **13**, 2759-2761 (2001).
- 128 Ozawa, T. C., Fukuda, K., Akatsuka, K., Ebina, Y. & Sasaki, T. Preparation and characterization of the Eu³⁺ doped perovskite nanosheet phosphor: La_{0.90}Eu_{0.05}Nb₂O₇. *Chem. Mater.* **19**, 6575-6580 (2007).
- 129 Ida, h. *et al.* Preparation of a blue luminescent nanosheet derived from layered perovskite Bi₂SrTa₂O₉. *J. Am. Chem. Soc.* **129**, 8956-8957 (2007).
- 130 Chevallier, i., Nihoul, G. & Madigou, V. Exfoliated nanoplatelets of an Aurivillius phase, Bi_{3.25}La_{0.75}Ti₃O₁₂: Characterisation by X-ray diffraction and by high-resolution electron microscopy. *J. Solid State Chem.* **181**, 439-449 (2008).
- 131 Osada, i. *et al.* Robust high-κ response in molecularly thin perovskite nanosheets. *ACS Nano* **4**, 5225-5232 (2010).
- 132 Li, B.-W. *et al.* Impact of perovskite layer stacking on dielectric responses in KCa₂Na_{n-3}NbnO_{3n+1} (n = 3–6) Dion-Jacobson homologous series. *Appl. Phys. Lett.* **96**, 182903 (2010).
- 133 Li, L., Ma, R., Ebina, Y., Iyi, N. & Sasaki, T. Positively charged nanosheets derived via total delamination of layered double hydroxides. *Chem. Mater.* **17**, 4386-4391 (2005).

- 134 Zhou, W. *et al.* Hydrazine-linked convergent self-assembly of sophisticated concave polyhedrons of β -Ni(OH)₂ and NiO from nanoplate building blocks. *J. Am. Chem. Soc.* **131**, 2959-2964 (2009).
- 135 Wang, X. & Li, Y. Rare-earth-compound nanowires, nanotubes, and fullerene-like nanoparticles: Synthesis, characterization, and properties. *Chem. Eur. J.* **9**, 5627-5635 (2003).
- 136 Wang, X. & Li, Y. Fullerene-like rare-earth nanoparticles. *Angew. Chem. Int. Ed.* **42**, 3497-3500 (2003).
- 137 Yang, L.-X., Zhu, Y.-J., Tong, H., Liang, Z.-H. & Wang, W.-W. Hierarchical β -Ni(OH)₂ and NiO nanorods assembled from nanosheet building blocks. *Cryst. Growth Des.* **7**, 2716-2719 (2007).
- 138 Ma, R. & Sasaki, T. Nanosheets of oxides and hydroxides: Ultimate 2D charge-bearing functional crystallites. *Adv. Mater.* **22**, 5082-5104 (2010).
- 139 Wang, L. *et al.* Layered assembly of graphene oxide and Co-Al layered double hydroxide nanosheets as electrode materials for supercapacitors. *Chem. Commun.* **47**, 3556-3558 (2011).
- 140 Naguib, M. *et al.* Two-dimensional nanocrystals produced by exfoliation of Ti₃AlC₂. *Adv. Mater.* **23**, 4248-4253 (2011).
- 141 Naguib, M. *et al.* Two-dimensional transition metal carbides. *ACS Nano* **6**, 1322-1331 (2012).
- 142 Tang, Q., Zhou, Z. & Shen, P. Are MXenes promising anode materials for Li ion batteries? computational studies on electronic properties and Li storage capability of Ti₃C₂ and Ti₃C₂X₂ (X = F, OH) monolayer. *J. Am. Chem. Soc.* **134**, 16909-16916 (2012).
- 143 Shein, I. R. & Ivanovskii, A. L. Planar nano-block structures Ti_{n+1}Al_{0.5}C_n and Ti_{n+1}C_n (n = 1, and 2) from MAX phases: Structural, electronic properties and relative stability from first principles calculations. *Superlattice. Microst.* **52**, 147-157 (2012).
- 144 Mashtalir, O. *et al.* Intercalation and delamination of layered carbides and carbonitrides. *Nat. Commun.* **4**, 1716 (2013).
- 145 Khazaei, M. *et al.* Novel electronic and magnetic properties of two-dimensional transition metal carbides and nitrides. *Adv. Funct. Mater.* **23**, 2185-2192 (2013).

- 146 Bhambhani, A. & Kumar, C. V. Enzyme-inorganic nanoporous materials: Stabilization of proteins intercalated in α -zirconium(IV) phosphate by a denaturant. *Microporous Mesoporous Mater.* **110**, 517-527 (2008).
- 147 Alberti, G., Dionigi, C., Giontella, E., Murcia-Mascarós, S. & Vivani, R. Formation of colloidal dispersions of layered γ -Zirconium phosphate in water/acetone mixtures. *J. Colloid Interface Sci.* **188**, 27-31 (1997).
- 148 Tas, A. C. & Bhaduri, S. B. Chemical processing of $\text{CaHPO}_4 \cdot 2\text{H}_2\text{O}$: Its conversion to hydroxyapatite. *J. Am. Ceram. Soc.* **87**, 2195-2200 (2004).
- 149 Lukyanyuk, V. K. & Z. D. Kovalyuk. Sodium intercalation into indium and gallium selenides. *Phys. Status Solidi, A Appl. Res.* **102**, K1-K5 (1987).
- 150 Mirabal, N., Lavayen, V., Benavente, E., Ana, M. A. S. & Gonzalez, G. Synthesis, functionalization, and properties of intercalation compounds. *Microelectron. J.* **35**, 37-40 (2004).
- 151 Bourdon, A., Bringuier, E., Portella, M. T., Vivières, M. & Piccioli, N. Angular properties of second-harmonic polarization due to high-order nonlinearities: Application to GaSe and InSe. *Phys. Rev. Lett.* **65**, 1925-1928 (1990).
- 152 Coleman, C. C., Goldwhite, H. & Tikkanen, W. A review of intercalation in heavy metal iodides. *Chem. Mater.* **10**, 2794-2800 (1998).
- 153 Wang, L., Brazis, P., Rocci, M., Kannewurf, C. R. & Kanatzidis, M. G. A new redox host for intercalative polymerization: Insertion of polyaniline into α - RuCl_3 . *Chem. Mater.* **10**, 3298-3300 (1998).
- 154 Herrmann, W. A., Öfele, K., Elison, M., Kühn, F. E. & Roesky, P. W. Nucleophilic cyclocarbenes as ligands in metal halides and metal oxides. *J. Organomet. Chem.* **480**, c7-c9 (1994).
- 155 Lee, C., Wei, X., Kysar, J. W. & Hone, J. Measurement of the elastic properties and intrinsic strength of monolayer graphene. *Science* **321**, 385-388 (2008).
- 156 Balandin, A. A. Thermal properties of graphene and nanostructured carbon materials. *Nature Mater.* **10**, 569-581 (2011).
- 157 Nair, R. R. *et al.* Fine structure constant defines visual transparency of graphene. *Science* **320**, 1308 (2008).
- 158 Bunch, J. S. *et al.* Impermeable atomic membranes from graphene sheets. *Nano Lett.* **8**, 2458-2462 (2008).

- 159 Wilson, J. A. & Yoffe, A. D. The transition metal dichalcogenides discussion and interpretation of the observed optical, electrical and structural properties. *Adv. Phys.* **18**, 193-335 (1969).
- 160 Mas-Ballesté, R., Gómez-Navarro, C., Gómez-Herrero, J. & Zamora, F. 2D materials: to graphene and beyond. *Nanoscale* **3**, 20-30 (2011).
- 161 Herrmann, H. J., Jr., J. S. A., Araújo, A. D. & Almeida, M. P. Particles in fluids. *Eur. Phys. J. Special Topics* **143**, 181-189 (2007).
- 162 Leal, L. G. Particle motions in a viscous fluid *Ann. Rev. Fluid Mech.* **12**, 435-476 (1980).
- 163 Lovvorn, J., Liggins, G. A., Borstad, M. H., Calisal, S. M. & Mikkelsen, J. Hydrodynamic drag of diving birds: effects of body size, body shape and feathers at steady speeds. *J. Exp. Biol.* **204**, 1547-1557 (2001).
- 164 Tran-Cong, S., Gay, M. & Michaelides, E. E. Drag coefficients of irregularly shaped particles. *Powder Technol.* **139**, 21-32 (2004).
- 165 Wang, X.-Q. & Mujumdar, A. S. Heat transfer characteristics of nanofluids: a review. *Int. J. Therm. Sci.* **46**, 1-19 (2007).
- 166 Sun, L., Boo, W. J., Sue, H.-J. & Clearfield, A. Preparation of α -zirconium phosphate nanoplatelets with wide variations in aspect ratios. *New J. Chem.* **31**, 39-43 (2007).
- 167 Díaz, A. *et al.* Nanoencapsulation of insulin into zirconium phosphate for oral delivery applications. *Biomacromolecules* **11**, 2465-2470 (2010).
- 168 Martin, J. M. & Ohmae, N. *Nanolubricants*, John Wiley & Sons, Ltd. (2008).
- 169 Kasai, T. & Bhushan, B. Physics and tribology of chemical mechanical planarization. *J. Phys.: Condens. Matter* **20**, 225011 (2008).
- 170 Chemali, C. E. *et al.* Multizone uniformity control of a chemical mechanical polishing process utilizing a pre- and postmeasurement strategy. *J. Vac. Sci. Technol. A* **18**, 1287-1296 (2000).
- 171 Tso, P., Wang, Y. & Tsai, M. A study of carrier motion on a dual-face CMP machine. *J. Mater. Process. Technol.* **116**, 194-200 (2001).
- 172 Carlos, L. D., Ferreira, R. A. S., Bermudez, V. d. Z. & Ribeiro, S. J. L. Lanthanide-containing light-emitting organic-inorganic hybrids: A bet on the future. *Adv. Mater.* **21**, 509-534 (2009).

- 173 Nishiura, M. & Hou, Z. Novel polymerization catalysts and hydride clusters from rare-earth metal dialkyls. *Nature Chem.* **2**, 257-268 (2010).
- 174 Govindarajan, S. *et al.* Higher permittivity rare earth doped HfO₂ for sub-45-nm metal-insulator-semiconductor devices. *Appl. Phys. Lett.* **91**, 062906 (2007).
- 175 Sugimoto, S. Current status and recent topics of rare-earth permanent magnets. *J. Phys. D: Appl. Phys.* **44**, 064001 (2011).
- 176 Si, R., Zhang, Y.-W., You, L.-P. & Yan, C.-H. Rare-earth oxide nanopolyhedra, nanoplates, and nanodisks. *Angew. Chem. Int. Ed.* **117**, 3320-3324 (2005).
- 177 Yan, Z. & Yan, C. Controlled synthesis of rare earth nanostructures. *J. Mater. Chem.* **18**, 5046-5059 (2008).
- 178 Buissette, V., Giaume, D., Gacoin, T. & Boilot, J.-P. Aqueous routes to lanthanide-doped oxide nanophosphors. *J. Mater. Chem.* **16**, 529-539 (2006).
- 179 Wang, J., Liu, Q. & Liu, Q. Synthesis and luminescence properties of Eu or Tb doped Lu₂O₃ square nanosheets. *Opt. Mater.* **29**, 593-597 (2007).
- 180 Fang, Y. *et al.* Hydrothermal synthesis of rare earth (Tb, Y) hydroxide and oxide nanotubes. *Adv. Funct. Mater.* **13**, 955-960 (2003).
- 181 Wang, X. & Li, Y. Synthesis and characterization of lanthanide hydroxide single-crystal nanowires. *Angew. Chem. Int. Ed.* **41**, 4790-4793 (2002).
- 182 Li, G., Li, C., Xu, Z., Cheng, Z. & Lin, J. Facile synthesis, growth mechanism and luminescence properties of uniform La(OH)₃ : Ho³⁺/Yb³⁺ and La₂O₃ : Ho³⁺/Yb³⁺ nanorods. *CrystEngComm* **12**, 4208-4216 (2010).
- 183 Mao, Y., Huang, J. Y., Ostroumov, R., Wang, K. L. & Chang, J. P. Synthesis and luminescence properties of erbium-doped Y₂O₃ nanotubes. *J. Phys. Chem. C* **112**, 2278-2285 (2008).
- 184 Tang, Q. *et al.* Synthesis of yttrium hydroxide and oxide nanotubes. *J. Crystal Growth* **259**, 208-214 (2003).
- 185 Silver, J., Martinez-Rubio, M. I., Ireland, T. G., Fern, G. R. & Withnall, R. The effect of particle morphology and crystallite size on the upconversion luminescence properties of erbium and ytterbium co-doped yttrium oxide phosphors. *J. Phys. Chem. B* **105**, 948-953 (2001).
- 186 Levy, R., Snyder, R. V. & Matthaiei, G. Design of microwave filters. *IEEE Trans. Microw. Theory Tech.* **50**, 783-793 (2002).

- 187 Kong, J. *et al.* 9.2-W diode-end-pumped Yb:Y₂O₃ ceramic laser. *Appl. Phys. Lett.* **86**, 161116 (2005).
- 188 Korzenski, M. B., Lecoeur, P., Mercey, B., Chippaux, D. & Raveau, B. PLD-grown Y₂O₃ thin films from Y metal: an advantageous alternative to films deposited from yttria. *Chem. Mater.* **12**, 3139-3150 (2000).
- 189 Huignard, A. *et al.* Growth by laser ablation of Y₂O₃ and Tm : Y₂O₃ thin films for optical applications. *J. Mater. Chem.* **10**, 549-554 (2000).
- 190 Zhitomirsky, I. & Petric, A. Electrochemical deposition of yttrium oxide. *J. Mater. Chem.* **10**, 1215-1218 (2000).
- 191 Nguyen, T.-D., Dinh, C.-T. & Do, T.-O. Shape- and size-controlled synthesis of monoclinic ErOOH and cubic Er₂O₃ from micro- to nanostructures and their upconversion luminescence. *ACS Nano* **4**, 2263-2273 (2010).
- 192 Park, D. H. *et al.* Low-temperature synthesis of Li_xMn_{0.67}Ni_{0.33}O₂ (0.2<x<0.33) nanowires with a hexagonal layered structure. *Adv. Mater.* **17**, 2834-2837 (2005).
- 193 Yada, M., Mihara, M., Mouri, S., Kuroki, M. & Kijima, T. Rare earth (Er, Tm, Yb, Lu) oxide nanotubes templated by dodecylsulfate assemblies. *Adv. Mater.* **14**, 309-313 (2002).
- 194 Huang, C.-C., Yeh, C.-S. & Ho, C.-J. Laser ablation synthesis of spindle-like gallium oxide hydroxide nanoparticles with the presence of cationic cetyltrimethylammonium bromide. *J. Phys. Chem. B* **108**, 4940-4945 (2004).
- 195 Titirici, M.-M., Antonietti, M. & Thomas, A. A Generalized synthesis of metal oxide hollow spheres Using a hydrothermal approach. *Chem. Mater.* **18**, 3808-3812 (2006).
- 196 Wu, M. *et al.* Sol-hydrothermal synthesis and hydrothermally structural evolution of nanocrystal titanium dioxide. *Chem. Mater.* **14**, 1974-1980 (2002).
- 197 Li, N., Yanagisawa, K. & Kumada, N. Facile hydrothermal synthesis of yttrium hydroxide nanowires. *Cryst. Growth Des.* **9**, 978-981 (2009).
- 198 Banfield, J. F., Welch, S. A., Zhang, H., Ebert, T. T. & Penn, R. L. Aggregation-based crystal growth and microstructure development in natural iron oxyhydroxide biomineralization products. *Science* **289**, 751-754 (2000).
- 199 Penn, R. L. *et al.* Epitaxial assembly in aged colloids. *J. Phys. Chem. B* **105**, 2177-2182 (2001).

- 200 Zhang, H., Miller, E. J. & Yu, E. T. Analysis of leakage current mechanisms in Schottky contacts to GaN and Al_{0.25}Ga_{0.75}N/GaN grown by molecular-beam epitaxy. *J. Appl. Phys.* **99**, 023703 (2006).
- 201 Tung, R. T. Electron transport at metal-semiconductor interfaces: General theory. *Phys. Rev. B* **45**, 13509-13523 (1992).
- 202 Cassagneau, T., Mallouk, T. E. & Fendler, J. H. Layer-by-layer assembly of thin film Zener diodes from conducting polymers and CdSe nanoparticles. *J. Am. Chem. Soc.* **120**, 7848-7859 (1998).
- 203 Rosam, B. *et al.* Field-Induced delocalization and Zener breakdown in semiconductor superlattices. *Phys. Rev. Lett.* **86**, 1307-1310 (2001).
- 204 Yang, J. J. *et al.* Memristive switching mechanism for metal/oxide/metal nanodevices. *Nat. Nanotechnol.* **3**, 429-433 (2008).
- 205 Sawa, A. Resistive switching in transition metal oxides. *Mater. Today* **11**, 28-36 (2008).
- 206 Waser, R. & Aono, M. Nanoionics-based resistive switching memories. *Nature Mater.* **6**, 833-840 (2007).
- 207 Janowitz, C. *et al.* Experimental electronic structure of In₂O₃ and Ga₂O₃. *New J. Phys.* **13**, 085014 (2011).
- 208 Krylova, K. *et al.* Ring size, substituent, and anion effects on the kinetic and equilibrium properties of copper(II) complexes with water-soluble macrocyclic tetrathia ethers. *Inorg. Chem.* **36**, 6216-6223 (1997).
- 209 Ambundo, E. A. *et al.* Influence of coordination geometry upon copper(II/I) redox potentials. Physical parameters for twelve copper tripod ligand complexes. *Inorg. Chem.* **38**, 4233-4242 (1999).
- 210 Nian, Y. B., Strozier, J., Wu, N. J., Chen, X. & Ignatiev, A. Evidence for an oxygen diffusion model for the electric pulse induced resistance change effect in transition-metal oxides. *Phys. Rev. Lett.* **98**, 146403 (2007).
- 211 Goux, L. *et al.* Evidences of oxygen-mediated resistive-switching mechanism in TiN/HfO₂/Pt cells. *Appl. Phys. Lett.* **97**, 243509 (2010).
- 212 Atienzar, P. *et al.* Layered γ -zirconium phosphate as novel semiconductor for dye sensitized solar cells: Improvement of photovoltaic efficiency by intercalation of a ruthenium complex-viologen dyad. *Energy Environ. Sci.* **4**, 4718-4726 (2011).

- 213 Clearfield, A. & Wang, Z. Organically pillared microporous zirconium phosphonates. *J. Chem. Soc., Dalton Trans.*, 2937-2947 (2002).
- 214 Clearfield, A. & Smith, G. D. Crystallography and structure of .alpha-zirconium bis(monohydrogen orthophosphate) monohydrate. *Inorg. Chem.* **8**, 431-436 (1969).
- 215 Amberger, E. & Stumpf, W. *Gmelin handbook of inorganic chemistry, boron*. Berlin, Germany, Springer, (1981).
- 216 Imai, Y., Mukaida, M., Ueda, M. & Watanabe, A. Screening of the possible boron-based *n*-type thermoelectric conversion materials on the basis of the calculated densities of states of metal borides and doped β -boron. *Intermetallics* **9**, 721-734 (2001).
- 217 Riedel, R. Novel ultrahard materials. *Adv. Mater.* **6**, 549-560 (1994).
- 218 Pyzik, A. J. & Beaman, D. R. Al-B-C phase development and effects on mechanical properties of B₄C/Al-derived composites. *J. Am. Ceram. Soc.* **78**, 305-312 (1995).
- 219 Hayun, S., Weizmann, A., Dilman, H., Dariel, M. P. & Frage, N. Rim region growth and its composition in reaction bonded boron carbide composites with core-rim structure. *J. Phys. Conf. Ser.* **176**, 012009 (2009).
- 220 Ogitsu, T. *et al.* Imperfect crystal and unusual semiconductor: boron, a frustrated element. *J. Am. Chem. Soc.* **131**, 1903-1909 (2009).
- 221 Otten, C. J. *et al.* Crystalline boron nanowires. *J. Am. Chem. Soc.* **124**, 4564-4565 (2002).
- 222 Tromp, H. J., Gelderen, P. v., Kelly, P. J., Brocks, G. & Bobbert, P. A. CaB₆: a new semiconducting material for spin electronics. *Phys. Rev. Lett.* **87**, 016401 (2001).
- 223 Zhang, H. *et al.* Nanostructured LaB₆ field emitter with lowest apical work function. *Nano Lett.* **10**, 3539-3544 (2010).
- 224 Wang, X. J. *et al.* Single crystalline boron nanocones: electric transport and field emission properties. *Adv. Mater.* **19**, 4480-4485 (2007).
- 225 Kirihara, K. *et al.* Dependence of photocurrent in single-crystalline boron nanobelts on atmosphere. *Appl. Phys. Lett.* **89**, 243121 (2006).

- 226 Kubota, Y., Watanabe, K., Tsuda, O. & Taniguchi, T. Deep ultraviolet light-emitting hexagonal boron nitride synthesized at atmospheric pressure. *Science* **317**, 932-934 (2007).
- 227 Watanabe, K., Taniguchi, T. & Kanda, H. Direct-bandgap properties and evidence for ultraviolet lasing of hexagonal boron nitride single crystal. *Nat. Mater.* **3**, 404-409 (2004).
- 228 Eremets, M. I., Struzhkin, V. V., Mao, H. & Hemley, R. J. Superconductivity in boron. *Science* **293**, 272-274 (2001).
- 229 Nagamatsu, J., Nakagawa, N., Muranaka, T., Zenitani, Y. & Akimitsu, J. Superconductivity at 39 K in magnesium diboride. *Nature* **410**, 63-64 (2001).
- 230 Schlapbach, L. & Züttel, A. Hydrogen-storage materials for mobile applications. *Nature* **414**, 353-358 (2001).
- 231 Yoon, C. W., Carroll, P. J. & Sneddon, L. G. Ammonia triborane: a new synthesis, structural determinations, and hydrolytic hydrogen-release properties. *J. Am. Chem. Soc.* **131**, 855-864 (2009).
- 232 Emin, D. Unusual properties of icosahedral boron-rich solids. *J. Solid State Chem.* **179**, 2791-2798 (2006).
- 233 Emin, D. & Aselage, T. L. A proposed boron-carbide-based solid-state neutron detector. *J. Appl. Phys.* **97**, 013529 (2005).
- 234 Liang, H. & Jahanmir, S. Boric acid as an additive for core-drilling of alumina *J. Tribol.* **117**, 65-71 (1995).
- 235 Albert, B. & Hillebrecht, H. Boron: elementary challenge for experimenters and theoreticians. *Angew. Chem. Int. Ed.* **48**, 8640-8668 (2009).
- 236 Werheit, H. *et al.* Raman effect in icosahedral boron-rich solids. *Sci. Technol. Adv. Mater.* **11**, 023001 (2010).
- 237 Oganov, A. R. *et al.* Ionic high-pressure form of elemental boron. *Nature* **457**, 863-867 (2009).
- 238 Setten, M. J. v., Uijttewaal, M. A., Wijs, G. A. d. & R. A. de Groot. Thermodynamic stability of boron: the role of defects and zero point motion. *J. Am. Chem. Soc.* **129**, 2458-2465 (2007).
- 239 Hoard, J. L., Hughes, R. E. & Sands, D. E. The structure of tetragonal boron. *J. Am. Chem. Soc.* **80**, 4507-4515 (1958).

- 240 Vlasse, M., Naslain, R., Kasper, J. S. & Ploog, K. Crystal structure of tetragonal boron related to α -AlB₁₂. *J. Solid State Chem.* **3**, 289-301 (1979).
- 241 Zarechnaya, E. Y. *et al.* Superhard semiconducting optically transparent high pressure phase of boron. *Phys. Rev. Lett.* **102**, 185501 (2009).
- 242 Bellott, B. J., Noh, W., Nuzzo, R. G. & Girolami, G. S. Nanoenergetic materials: boron nanoparticles from the pyrolysis of decaborane and their functionalisation. *Chem. Commun.* **2009**, 3214-3215 (2009).
- 243 Devener, B. V., Paulo, J., Perez, L. & Anderson, S. L. Air-stable, unoxidized, hydrocarbon-dispersible boron nanoparticles. *J. Mater. Res.* **24**, 3462-3464 (2009).
- 244 Pickering, A. L., Mitterbauer, C., Browning, N. D., Kauzlarich, S. M. & Power, P. P. Room temperature synthesis of surface-functionalised boron nanoparticles. *Chem. Commun.* **2007**, 580-582 (2007).
- 245 Ciuparu, D., Klie, R. F., Zhu, Y. & Pfefferle, L. Synthesis of pure boron single-wall nanotubes. *J. Phys. Chem. B* **108**, 3967-3969 (2004).
- 246 Cao, L. *et al.* Well-aligned boron nanowire arrays. *Adv. Mater.* **13**, 1701-1704 (2001).
- 247 Tian, J. *et al.* Boron nanowires for flexible electronics. *Appl. Phys. Lett.* **93**, 122105 (2008).
- 248 Xu, T. T. *et al.* Crystalline boron nanoribbons: synthesis and characterization. *Nano Lett.* **4**, 963-968 (2004).
- 249 Adams, D. P. & Yalisove, S. M. Low-temperature homoepitaxial growth on nonplanar Si substrates. *J. Appl. Phys.* **76**, 5185-5189 (1994).
- 250 Meyerson, B. S. Low-temperature silicon epitaxy by ultrahigh vacuum/chemical vapor deposition. *Appl. Phys. Lett.* **48**, 797-799 (1986).
- 251 Platen, J. *et al.* Low-temperature epitaxial growth of Si by electron cyclotron resonance chemical vapor deposition. *Thin Solid Films* **381**, 22-30 (2001).
- 252 Du, X. & He, J. Spherical silica micro/nanomaterials with hierarchical structures: synthesis and applications. *Nanoscale* **3**, 3984-4002 (2011).
- 253 Song, C., Zhao, G., Zhang, P. & Rosi, N. L. Expeditious synthesis and assembly of sub-100 nm hollow spherical gold nanoparticle superstructures. *J. Am. Chem. Soc.* **132**, 14033-14035 (2010).

- 254 Aradi, B., Deák, P., Son, N. T., Janzén, E. & Choyke, W. J. Impurity-controlled dopant activation: hydrogen-determined site selection of boron in silicon carbide. *Appl. Phys. Lett.* **79**, 2746-2748 (2001).
- 255 Kobayashi, H., Nomachi, I., Kusanagi, S. & Nishiyam, F. Activation and dopant sites of ultra-shallow implanted boron and arsenic in silicon. *Nucl. Instr. and Meth. in Phys. Res. B* **190**, 547-551 (2002).
- 256 Sameshima, T. & Andoh, N. Activation behavior of boron and phosphorus atoms implanted in polycrystalline silicon films by heat treatment at 250 °C. *Jpn. J. Appl. Phys.* **44**, 1186-1191 (2005).
- 257 Erdemir, A., Fenske, G. R. & Erck, R. A. A study of the formation and self-lubrication mechanisms of boric acid films on boric oxide coatings. *Surf. Coat. Technol.* **43-44**, 588-596 (1990).
- 258 Ma, X., Unertl, W. N. & Erdemir, A. The boron oxide-boric acid system: nanoscale mechanical and wear properties. *J. Mater. Res.* **14**, 3455-3466 (1999).
- 259 Martin, J. M. & Ohmae, N. *Nanolubricants*. Chichester, West Sussex, UK, John Wiley & Sons, Ltd, (2008).
- 260 Bhushan, B. *Introduction to tribology (Tribology in practice series)*. Somerset, NJ, Wiley, (2013).
- 261 Stachowiak, G. & Batchelor, A. W. *Engineering tribology*. Waltham, MA, Butterworth-Heinemann, (2014).
- 262 He, X., Demchenko, I. N., Stolte, W. C., Buuren, A. v. & Liang, H. Synthesis and transformation of Zn-doped PbS quantum dots. *J. Phys. Chem. C* **116**, 22001-22008 (2012).
- 263 Horsley, S. E., Nowell, D. V. & Stewart, D. T. The infrared and Raman spectra of α -zirconium phosphate. *Spectrochim. Acta Mol. Spectros.* **30**, 535-541 (1974).
- 264 Helen, M., Viswanathan, B. & Murthy, S. S. Synthesis and characterization of composite membranes based on α -zirconium phosphate and silicotungstic acid. *J. Membr. Sci.* **292**, 98-105 (2007).
- 265 Díaz, A. *et al.* Zirconium phosphate nano-platelets : a novel platform for drug delivery in cancer therapy. *Chem. Commun.* **48**, 1754-1756 (2012).
- 266 Bestaoui, N., Spurr, N. A. & Clearfield, A. Intercalation of polyether amines into α -zirconium phosphate. *J. Mater. Chem.* **16**, 759-764 (2006).

- 267 Liang, H. & Craven, D. *Tribology in chemical-mechanical planarization*. Boca Raton, FL, CRC Press, (2005).
- 268 Li, Y. *Microelectronic applications of chemical mechanical planarization*. Hoboken, NJ, Wiley-Interscience, (2007).
- 269 Gao, F. & Liang, H. In situ observation of friction-induced electrochemical reactions and impedance in tantalum ECMP. *J. Electrochem. Soc.* **156**, H80-H86 (2009).
- 270 Feng, X. *et al.* Converting ceria polyhedral nanoparticles into single-crystal nanospheres. *Science* **312**, 1504-1508 (2006).
- 271 Li, Y., Hariharaputhiran, M. & Babu, S. V. Chemical-mechanical polishing of copper and tantalum with silica abrasives. *J. Mater. Res.* **16**, 1066-1073 (2001).
- 272 Zhu, H., Niesz, D. E., Greenhut, V. A. & Sabia, R. The effect of abrasive hardness on the chemical-assisted polishing of (0001) plane sapphire. *J. Mater. Res.* **20**, 504-520 (2005).
- 273 Joo, S. & Liang, H. Tribo-electrochemical characterization of copper with patterned geometry. *Microelectron. Eng.* **98**, 12-18 (2012).
- 274 Su, J., Chen, X., Du, J., Guo, D. & Kang, R. Analyzing on nonuniformity of material removal in silicon wafer cmp based on abrasive movement trajectories. *Adv. Mater. Res.* **53-54**, 119-124 (2008).
- 275 Hocheng, H., Tsai, H. Y. & Tsai, M. S. Effects of kinematic variables on nonuniformity in chemical mechanical planarization. *Int. J. Mach. Tool Manu.* **40**, 1651-1669 (2000).
- 276 Feng, T. Nonuniformity of wafer and pad in cmp: kinematic aspects of view. *IEEE Trans. Semicond. Manuf.* **20**, 451-463 (2007).
- 277 Kim, H. & Jeong, H. Effect of process conditions on uniformity of velocity and wear distance of pad and wafer during chemical mechanical planarization. *J. Electron. Mater.* **33**, 53-60 (2004).
- 278 Lee, H., Park, B. & Jeong, H. Influence of slurry components on uniformity in copper chemical mechanical planarization. *Microelectron. Eng.* **85**, 689-696 (2008).
- 279 Sikder, A. K., Giglio, F., Wood, J., Kumar, A. & Anthony, M. Optimization of tribological properties of silicon dioxide during the chemical mechanical planarization process. *J. Electron. Mater.* **30**, 1520-1526 (2001).

- 280 Fu, G. & Chandra, A. An analytical dishing and step height reduction model for chemical mechanical planarization (CMP). *IEEE Trans. Semicond. Manuf.* **16**, 477-485 (2003).
- 281 Nguyen, V. H., Daamen, R., Kranenburg, H. v., Velden, p. v. d. & Woerlee, P. H. A physical model for dishing during metal CMP. *J. Electrochem. Soc.* **150**, G689-G693 (2003).
- 282 Ward-Smith, J. *Mechanics of Fluids*. New York, NY, CRC Press, (2011).
- 283 Taylor, G. The dispersion of matter in turbulent flow through a pipe. *Proc. R. Soc. Lond. A* **223**, 446-468 (1954).
- 284 Spalding, D. B. Mass transfer in laminar flow. *Proc. R. Soc. Lond. A* **221**, 78-99 (1954).
- 285 Luo, J. & Dornfeld, D. A. Material removal mechanism in chemical mechanical polishing: theory and modeling. *IEEE Trans. Semicond. Manuf.* **14**, 112-133 (2001).
- 286 Bozkaya, D. & Müftü, S. A material removal model for cmp based on the contact mechanics of pad, abrasives, and wafer. *J. Electrochem. Soc.* **156** (2009).
- 287 Runnels, S. R. & Eyman, L. M. Tribology analysis of chemical-mechanical polishing. *J. Electrochem. Soc.* **141**, 1698-1701 (1994).
- 288 Chen, J. M. & Fang, Y.-C. Hydrodynamic characteristics of the thin fluid film in chemical-mechanical polishing. *IEEE Trans. Semicond. Manuf.* **15**, 39-44 (2002).
- 289 Liang, H. Chemical boundary lubrication in chemical-mechanical planarization. *Tribol. Int.* **38**, 235-242 (2005).
- 290 Grover, G. S., Liang, H., Ganeshkumar, S. & Fortino, W. Effect of slurry viscosity modification on oxide and tungsten CMP. *Wear* **214**, 10-13 (1998).
- 291 Nolan, L. & Cadien, K. Copper CMP: The relationship between polish rate uniformity and lubrication. *ECS J. Solid State Sci. Technol.* **1**, P157-P163 (2012).
- 292 Lin, S. & Wu, M. A study of the effects of polishing parameters on material removal rate and non-uniformity. *Int. J. Mach. Tool Manu.* **42**, 99-103 (2002).
- 293 Vlassak, J. J. A contact-mechanics based model for dishing and erosion in chemical-mechanical polishing. *Mater. Res. Soc. Symp.* **671**, M4.6.1-M4.6.6 (2001).

- 294 Saka, N., Lai, J. Y., Chun, J. H. & Shu, N. P. Mechanisms of the chemical mechanical polishing (CMP) process in integrated circuit fabrication. *CIRP Ann. Manuf. Technol.* **50**, 233-238 (2001).
- 295 Kondo, S. *et al.* Abrasive-free polishing for copper damascene interconnection. *J. Electrochem. Soc.* **147**, 3907-3913 (2000).
- 296 Chiu, J., Yu, C. & Shen, S. Application of soft landing to the process control of chemical mechanical polishing. *microelectron. Eng.* **65**, 345-356 (2003).
- 297 Denardis, D., Sorooshian, J., Habiro, M., Rogers, C. & Philipossian, A. Tribology and removal rate characteristics of abrasive-free slurries for copper CMP applications. *Jpn. J. Appl. Phys.* **42**, 6809-6814 (2003).
- 298 Telle, R. Boride-eine neue Hartstoffgeneration? *Chem. Unserer Zeit* **22**, 93-99 (1988).
- 299 Wood, C. Materials for thermoelectric energy conversion. *Rep. Prog. Phys.* **51**, 459-539 (1988).
- 300 S. Pandija, D. Roy & Babu, S. V. Achievement of high planarization efficiency in CMP of copper at a reduced down pressure. *Microelectron. Eng.* **86**, 367-373 (2009).
- 301 Xu, G., Liang, H., Zhao, J. & Li, Y. Investigation of copper removal mechanisms during CMP. *J. Electrochem. Soc.* **151**, G688-G692 (2004).
- 302 Carnes, C. L. & Klabunde, K. J. Synthesis, isolation, and chemical reactivity studies of nanocrystalline zinc oxide. *Langmuir* **16**, 3764-3772 (2000).
- 303 Kalinin, S. V. *et al.* Atomic polarization and local reactivity on ferroelectric surfaces: a new route toward complex nanostructures. *Nano Lett.* **2**, 589-593 (2002).
- 304 Liang, H., Mogne, T. L. & Martin, J.-M. Interfacial transfer between copper and polyurethane in chemical-mechanical polishing. *J. Electron. Mater.* **31**, 872-878 (2002).
- 305 Liang, H., Martin, J.-M. & Lee, R. Influence of oxides on friction during Cu CMP. *J. Electron. Mater.* **30**, 391-395 (2001).
- 306 Dandu, P. R. V., Devarapalli, V. K. & Babu, S. V. Reverse selectivity - High silicon nitride and low silicon dioxide removal rates using ceria abrasive-based dispersions. *J. Colloid. Interf. Sci.* **347**, 267-276 (2010).

- 307 Veera, P. R. D., Natarajan, A., Hegde, S. & Babu, S. V. Selective polishing of polysilicon during fabrication of microelectromechanical systems devices. *J. Electrochem. Soc.* **156**, H487-H494 (2009).
- 308 Li, Y. Microelectronic applications of chemical mechanical planarization, Hoboken, NJ, Wiley-Interscience, (2007).
- 309 Zantye, P. B., Kumar, A. & A. K. Sikder. Chemicalmechanicalplanarization for microelectronicsapplications. *Mater. Sci. Eng. R Rep.* **45**, 89-220 (2004).
- 310 Liu, X., Wazne, M., Christodoulatos, C. & Jasinkiewicz, K. L. Aggregation and deposition behavior of boron nanoparticles in porous media. *J. Colloid. Interf. Sci.* **330**, 90-96 (2009).
- 311 Fischer, T. E. Tribochemistry. *Ann. Rev. Mater. Sci.* **18**, 303-323 (1988).
- 312 Fischer, T. E., Liang, H. & Mullins, W. M. Tribochemical lubricious oxides on silicon nitride. *Mater. Res. Soc. Symp. Proc.* **140**, 339-344 (1989).
- 313 Said, J. & Zhang, G. US Patent No: 5,507,962 patent (1996).
- 314 Erdemir, A., Fenske, G. R., Erck, R. A., Nichols, F. A. & Busch, D. Tribological properties of boric acid and boric-acid-forming surfaces: Part 2, Formation and self-lubrication mechanisms of boric acid films on boron- and boric-oxide-containing surfaces. *Lubr. Eng.* **47**, 179-184 (1991).
- 315 Stribeck, R. Kugellager für beliebige Belastungen, Zeitschrift des Vereins Deutscher Ingenieure (VDI) 3 (Band 45) 73-79 (1901).
- 316 Woydt, M. & Wäsche, R. The history of the Stribeck curve and ball bearing steels: The role of Adolf Martens. *Wear* **268**, 1542-1546 (2010).
- 317 Zhang, W. *et al.* Tribological properties of oleic acid-modified graphene as lubricant oil additives. *J. Phys. D: Appl. Phys.* **44**, 205303 (2011).
- 318 Andras Z. Szeri. *Fluid film lubrication*. New York, NY, Cambridge University Press, (2010).
- 319 Braun, O. M. & Naumovets, A. G. Nanotribology: Microscopic mechanisms of friction. *Surf. Sci. Rep.* **60**, 79-158 (2006).
- 320 Barnes, H. A. Thixotropy-a review. *J. Non-Newtonian Fluid Mech.* **70**, 1-33 (1997).
- 321 Einstein, A. Investigations on the theory of Brownian movement. *Ann. Phys.* **324**, 371-381 (1906).

- 322 Werff, J. C. v. d. & Kruif, C. G. d. Hard-sphere colloidal dispersions: the scaling of rheological properties with particle size, volume fraction, and shear rate. *J. Rheol.* **33**, 421-454 (1989).
- 323 Russel, W. B., Saville, D. A. & Schowalter, W. R. *Colloidal dispersions (Cambridge Monographs on Mechanics)*. New York, NY, Cambridge University Press, (1992).
- 324 Xie, X.-L. *et al.* Rheological and mechanical properties of PVC/CaCO₃ nanocomposites prepared by in situ polymerization. *Polymer* **45**, 6665-6673 (2004).
- 325 Tuteja, A., Duxbury, P. M. & Mackay, M. E. Multifunctional nanocomposites with reduced viscosity. *Macromolecules* **40**, 9427-9434 (2007).
- 326 Jain, S., Goossens, J. G. P., Peters, G. W. M., Duin, M. v. & Lemstra, P. J. Strong decrease in viscosity of nanoparticle-filled polymer melts through selective adsorption. *Soft Matter* **4**, 1848-1854 (2008).
- 327 Hamrock, B. J., Schmid, S. R. & Jacobson, B. O. *Fundamental of fluid film lubrication*. New York, NY, CRC Press, (2004).
- 328 Szeri, A. Z. *Fluid film lubrication*. New York, NY, Cambridge University Press, (2010).
- 329 Martys, N. S., George, W. L., Chun, B.-W. & Lootens, D. A smoothed particle hydrodynamics-based fluid model with a spatially dependent viscosity: Application to flow of a suspension with a non-newtonian fluid matrix. *Rheol. Acta* **49**, 1059-1069 (2010).
- 330 Monaghan, J. J. Smoothed particle hydrodynamics. *Rep. Prog. Phys.* **68**, 1703-1759 (2005).
- 331 Kyle, J. P. & Terrell, E. J. Application of smoothed particle hydrodynamics to full-film lubrication. *J. Tribol.* **135**, 041705 (2013).
- 332 Jonathan W. Bender, N. J. W. Optical measurement of the contributions of colloidal forces to the rheology of concentrated suspensions. *J. Colloid Interface Sci.* **172**, 171-184 (1995).
- 333 Brady, J. F. The rheological behavior of concentrated colloidal dispersions. *J. Chem. Phys.* **99**, 567-581 (1993).

- 334 Cheng, X., McCoy, J. H., Israelachvili, J. N. & Cohen, I. Imaging the microscopic structure of shear thinning and thickening colloidal suspensions. *Science* **333**, 1276-1279 (2011).
- 335 Xu, X., Rice, S. A. & Dinner, A. R. Relation between ordering and shear thinning in colloidal suspensions. *Proc. Natl. Acad. Sci. U.S.A.* **110**, 3771-3776 (2013).
- 336 Bäbler, M. U., Morbidelli, M. & Bałdyga, J. Modelling the breakup of solid aggregates in turbulent flows. *J. Fluid Mech.* **612**, 261-289 (2008).
- 337 Zaccone, A. *et al.* Breakup of dense colloidal aggregates under hydrodynamic stresses. *Phys. Rev. E* **79**, 061401 (2009).
- 338 Foss, D. R. & Brady, J. F. Structure, diffusion and rheology of Brownian suspensions by Stokesian Dynamics simulation. *J. Fluid Mech.* **407**, 167-200 (2000).
- 339 Alam, M. & Sandham, N. D. Direct numerical simulation of "short" laminar separation bubbles with turbulent reattachment. *J. Fluid Mech.* **410**, 1-28 (2000).
- 340 Hasan, M. A. Z. The flow over a backward-facing step under controlled perturbation: laminar separation. *J. Fluid Mech.* **238**, 73-96 (1992).
- 341 Pauley, L. L., Moinz, P. & Reynold, W. C. The structure of two-dimensional separation. *J. Fluid Mech.* **220**, 397-411 (1990).
- 342 Giddings, J. C. Field-flow fractionation: analysis of macromolecular, colloidal, and particulate materials. *Science* **260**, 1456-1465 (1993).
- 343 Williams, S., Koch, T. & Calvin, J. Characterization of near-wall hydrodynamic lift forces using sedimentation field-flow fractionation. *Chem. Eng. Commun.* **111**, 121-147 (1992).
- 344 Costa, H. L. & Hutchings, I. M. Hydrodynamic lubrication of textured steel surfaces under reciprocating sliding conditions. *Tribol. Int.* **40**, 1227-1238 (2007).